# Full-wave Algorithms for Model Order Reduction and Electromagnetic Analysis of Impedance and Scattering

by

Thomas Jonas Klemas

B.S., Massachusetts Institute of Technology (1993,2001)
M.Eng., Massachusetts Institute of Technology (1994)

Submitted to the Department of Electrical Engineering and Computer Science
in partial fulfillment of the requirements for the degree of

Doctor of Philosophy in Electrical Engineering

at the

MASSACHUSETTS INSTITUTE OF TECHNOLOGY

May 2005

Author . . . . . . . . . . . . . . . . . . . . . . . . . . . . . . . . . . . . . . . . . . . . . . . . . . . . . . .
Department of Electrical Engineering and Computer Science
May 18, 2005

Certified by. . . . . . . . . . . . . . . . . . . . . . . . . . . . . . . . . . . . . . . . . . . . . . . . . . .
Jacob K. White
Associate Director, Research Laboratory for Electronics
Thesis Supervisor

Accepted by . . . . . . . . . . . . . . . . . . . . . . . . . . . . . . . . . . . . . . . . . . . . . . . . . . .
Arthur C. Smith
Chairman, Department Committee on Graduate Students

# Full-wave Algorithms for Model Order Reduction and Electromagnetic Analysis of Impedance and Scattering

by

## Thomas Jonas Klemas

## Abstract

As technology advances and sophisticated electronic systems achieve ubiquity, the demand for thorough, efficient Electromagnetic (EM) analysis continues to rise. The prohibitive costs of constructing and maintaining measurement facilities and designing and building system prototypes has fueled even greater demand for Computational Electromagnetics (CEM). Today's CEM solvers can generate models that accurately characterize the EM behavior of an arbitrary structure presented for analysis. Two important applications for CEM are Scattering analysis of targets excited by EM waves and impedance modelling for the interconnect between the electronic components in Systems on Package (SoP) and Systems on Board (SoB).

Often, the goal of analysis is to characterize behavior relative to parameters of interest, and EM solvers can generate parameter-dependent models of the system. The complexity of structures has increased so much that solving the solver-generated models at numerous desired parameter-points is a daunting computational task. For example, using these models in a simulator would be infeasible. Instead, existing Model Order Reduction (MOR) algorithms can construct reduced order models (ROMs) that characterize the parameter-dependent behavior of the original system. These existing methods are effective when the system of equations is linearly or weakly nonlinearly dependent on the parameters.

When analyzing structures that are large compared to wavelengths of interest, retardation generates an exponentially nonlinear dependence on frequency, and such a strong nonlinearity makes it impossible to use existing MOR methods. This dissertation describes a new algorithm, Segregation by Primary Phase factors, that extends existing projection-based MOR techniques to the case of "Electromagnetically Large" structures. Extensions of the SPPF method to problems with parameter-dependent excitation are considered, as well as how to combine SPPF with fast integral equation solvers.

# Acknowledgments

There are so many people who deserve thanks. Almost everyone at MIT and the Air Force Research Laboratory that I have interacted with during my daily routine has offered encouragement and valuable insights. Even acquaintances at the MIT gym were occasionally excellent resources for technical and procedural advice.

However, some people have had a dominant impact on my progress: My advisor, Professor Jacob White, in supervising my research, has shown great understanding, been most supportive, and yet allowed a great deal of independence. Jacob has helped me learn to stay on target, to maximize advantage of the set of skills I do have rather than lamenting those I do not, and to optimize effort to take advantage of the peculiarities of the learning curve which I have, rather than trying to fit my learning onto a "standard" curve. Through his guidance, I have learned that thinking about things from an unorthodox perspective and processing information differently can be an advantage if harnessed properly.

I am also deeply grateful to Professor Luca Daniel. Luca has always been available for help and technical discussions, providing valuable advice on almost any subject. At the time of this writing, two publications related to this dissertation have been accepted, but none would have been submitted in time without Luca's patience and "above-and-beyond" commitment to assist students whenever we ask.

From the Air Force Research Laboratory (AFRL), I am grateful especially to Dr. Schindler, my supervisor Bert Weijers, Dr. Rangaswamy, and Dr. Kim. Dr. Schindler agreed to participate on my thesis committee after very little introduction and his EM expertise has proved to be a tremendous resource for me in examining results and guiding the latter stages of this research. Both Bert and Dr. Kim have provided excellent support, particularly in helping me define a suitable application for the research. Both Dr. Rangaswamy and Dr. Kim have shared a number of very fruitful discussions with me about technical subjects, the Air Force, and other pertinent topics.

Every student in the computational prototyping group and many others that I

have interacted with at MIT have helped me both technically and by being a role model in some way. For this, I must thank Jung Hoon Lee, Luke Theogarajan, Niell Elvin, David Willis, Jaydeep Bardhan, Carlos Coelho, Xin Hu, Shihhsien Kuo, Zhenhai Zhu, Anne Vithayathil, Dimitry Vasilyev, Xin Wang, Joe Kanapka, Deepak Ramaswamy, Jing Li, Michal Rewienski, Dimitry Vasilyev, and Bradley Bond. Former RLE-VLSI group research scientists David Kring and Tom Korsemeyer played an important role in getting me started. There have been many MIT Professors, Lecturers, and staff who were inspiration instructors or generously shared with me during meetings or chance encounters. I have learned valuable things from many people whether they were aware or not, and I am grateful.

Finally, my parents, family, and friends have given me invaluable emotional support and advice throughout my graduate career. One can sometimes feel pretty lonely when working late in the middle of the night and suffering sleep deprivation. Without the support of so many special people, I would not have made it to MIT in the first place, let alone finding a path that would lead to completion of this important stage of my journey towards self-enlightenment.

## Biography

Thomas Jonas Klemas first attended MIT in the fall of 1988. He received a Bachelor of Science (B.S.) degree in Electrical Engineering from MIT in 1993 and a Master of Engineering (M.Eng) degree in Electrical Engineering from MIT in 1994. His undergraduate thesis, titled "A Monte Carlo Simulation of Radiation Transport for Benchmarking Intel's iPSC/2, iPSC/860, and Touchstone Delta Machine", was awarded the Charles and Jennifer Johnson Outstanding Thesis Award in Computer Science and a $1500 prize.

In 1993, he was commissioned as Second Lieutenant in the United States Air Force and he entered active duty in February of 1994. He was assigned to the Rome Laboratory at Hanscom Air Force Base, where he led a project to assemble and program a parallel processing system in order to perform Neural Network Beamforming for

Phased Array Antennas. He contributed several key ideas and was the coauthor of a paper that won Department of Air Force Scientific Achievement Award entitled Network Antenna Processing for Detection and Direction Finding" in 1995. Also, in 1995, First Lieutenant Klemas was selected to train for the All-military volleyball team, and he represented United States of America at 1st Military World Games in Rome, Italy as the team alternate.

In 1998, he separated from the Air Force and applied and was accepted into MIT's graduate school for Electrical Engineering and began doctoral studies in the Computational Prototyping Group at the Research Laboratory for Electronics under the guidance of Professor Jacob White. During these studies, he earned a second B.S degree in Mathematics from MIT in 2001. Also, in 2001 Captain Thomas Klemas joined the US Air Force Reserves and was assigned to the Electromagnetic Scattering Branch of the Sensors Directorate of the Air Force Research Laboratory and was promoted to Major in 2004. In May 2005, several of his research contributions were selected for publication and presentation at Conferences. The 2005 Digital Automation Conference accepted his paper titled, "Segregation by Primary Phase Factors: A Full-wave Algorithm for Model Order Reduction", and the 2005 IEEE AP-S International Symposium on Antennas and Propagation and USNC/URSI National Radio Science Meeting accepted his paper titled, "A Fast Full-Wave Algorithm to Generate Low Order Electromagnetic Scattering Models". Also in May 2005, Major Thomas Klemas' AFRL Radio Frequency Thrust research grant proposal was awarded funding. The research grant will fund a computational research project that Major Klemas hopes will lead to future collaborative efforts of larger scope.

# Contents

**11 Conclusion**        **163**

**A Survey of Military Ground Vehicles**        **167**

**B Rotation of Axes**        **169**

# Chapter 1

# Introduction

The 21st century will be no different than the 20th century in at least one respect: The pace of technological advancement will continue to increase. Rather than satisfying society's needs, all of the past innovation has only accelerated demand for the next generation of technologies. One of the primary reasons that technological capability has progressed so dramatically is that the complexity of systems has increased just as quickly. The adoption of modular designs has heralded systems that comprise of ever-more elaborate combinations of complicated elements. Correspondingly, the list of factors that engineers and manufacturers must consider during the design of new systems has expanded rapidly. As a result, the design of new technology requires ever-greater effort and skill to manage and guide the surging complexity of systems. Therefore, the need for efficient and accurate systems analysis tools to aid engineers during the design process is greater than ever.

Electronics have been at the forefront of technological innovations during the 20th century. Thus, much effort has been invested in developing tools for electromagnetic (EM) analysis. Designing special EM measurement facilities and building prototype structures to test is usually very expensive. Therefore, Computational Electromagnetics (CEM) is a field of growing importance. Computational EM analysis tools that are based on formulations of Maxwell's Laws can generate models that accurately characterize the EM behavior of arbitrary structures. Two CEM applications of particular interest are EM scattering analysis and Impedance extraction for interconnect

structures.

In the semiconductor industry, added complexity of electronic systems and increasing signal frequencies can lead to problems with interference. As wavelengths decrease relative to the size of interconnect structures on system on packages (SoP) and System on Boards (SoB), interconnect structures will transmit conductive interference to nearby sections of the system, and radiative interference to distant portions of the system. Conductive interference induces currents and voltages on adjacent portions of the system, while radiative interference induces retarded currents and voltages on nearby and distant portions of the system. Interference of either type can impair operation of the electronic system, and, as a result, must be considered during the design process. Therefore, Electromagnetic (EM) analysis of interference in proposed systems is imperative.

For the civilian transportation industry and for the military, the design of surveillance systems and counter-surveillance measures requires detailed EM analysis. For example, civilian transportation industries and the military have an ever-increasing need for advanced radar systems with improved target detection, automatic target recognition, and other sophisticated remote sensing capabilities. Air Traffic Control systems, employed at airports throughout the world to facilitate safe take-offs and landings for aircraft, require meticulous design and EM analysis. The design of communications antennas and sensors on aircraft requires careful EM analysis to understand interactions of EM fields and waves with the body of the aircraft and each other to ensure both safety and functionality. In military contexts, designers must also consider that the enemy may attempt to jam the communications, sensors, and other systems of an aircraft, ship, ground vehicle, or facility. Additionally, there is a strong interest in improving capabilities to design stealth systems that are invisible to radar. Designing aircraft, ground vehicles, and other weapons systems with lower radar cross-sections increases the survivability of these systems! These are just a few applications which have a clearcut need for EM scattering analysis.

Many CEM tools have been developed for EM analysis for these application. Impedance extraction tools generate models that characterize the impedance behavior

of interconnect structures on electronics systems, such as System on Packages (SoP) and System on Boards (SoB) and relate system charges and currents to the source voltage. The impedance models allow engineers to simulate the behavior of the system to understand the interference that occurs. EM scattering solvers can generate models that characterize the current density induced when an source EM wave contacts the surface of the scattering target. From the induced surface current, other scattering quantities of interest, such as radar cross section or field quantities, can be computed at desired observation points. Thus, engineers can use these models design better stealth systems, target detection systems, target recognition systems, radar, and much more.

Matching the growing complexity of systems, the models generated by CEM tools have become very complicated and extremely large systems of equations are required to describe the system, such that using the original model to solve for desired quantities is frequently prohibitively time-consuming. Thus, acceleration methods, such as sparsification algorithms [36] [8] [2] [43] [4], have been developed to permit efficient solution by constructing an approximation to the original model that can be solved very rapidly.

Often, one wishes to characterize or understand some parameter-dependencies of a system, perhaps through simulation, but the complexity of the models prohibit direct use in simulation or to solve the system to compute results at every required point over a desired parameter range. However, by using information obtained from solving the system of equations at just a few parameter points, one can use standard Model Order Reduction (MOR) techniques [?] [5] [30] [34] [12] [42] [37] [9] to construct reduced order models (ROMs) that can be rapidly solved to characterize the parameter-dependent behavior of a large system over the rest of the desired parameter range.

Standard Model Order Reduction techniques are effective for generating low order models to approximate systems in Quasistatic analysis regimes with polynomial frequency dependencies. Figure 1-1 illustrates these regimes, where the signal wavelength is much greater than the maximum diameter of the structure. The traditional

15
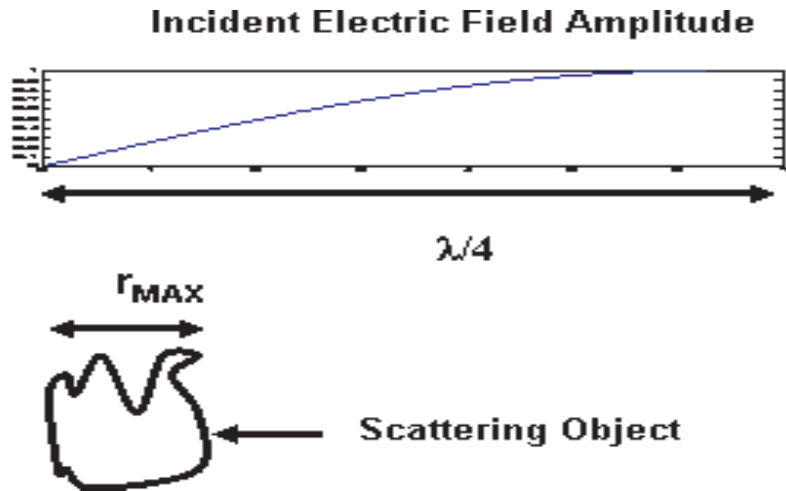
Figure 1-1: Quasi-static EM Analysis: The amplitude of the incident source field and interactions between distant panel pairs on the geometry vary very slowly ($\lambda > 8r_{MAX}$) over the diameter of the structure and will not induce significant voltage differences.

MOR methods have been extended [34] to approximate systems with weakly oscillatory frequency dependencies.

However, there are still many limitations to what CEM can accomplish. Existing MOR methods are *not effective* for *full-wave* analysis regimes and *unable* to efficiently generate accurate models for *"electromagnetically large"* structures. Figure 1-2 illustrates the full-wave analysis regime, in which the wavelength of the signal is comparable or smaller than the maximum diameter of the structure. Complicating matters, the frequencies of signals present in today's technology are increasingly in the full-wave regime. The primary contribution of this thesis is an algorithm, **Segregation by Primary Phase Factors (SPPF)**, that facilitates *multi-point, multi-parameter, sparsified, full-wave Model Order Reduction (FMOR)*: The resulting low order SPPF-FMOR models can accurately characterize the parameter-dependent behavior of "electromagnetically large" systems and enable rapid analysis of arbitrary EM structures.

The remainder of this introductory chapter will introduce the two applications and attempt to motivate the contributions of the research described in this dissertation. Chapter 2 will present the background material in sections that outline the develop-
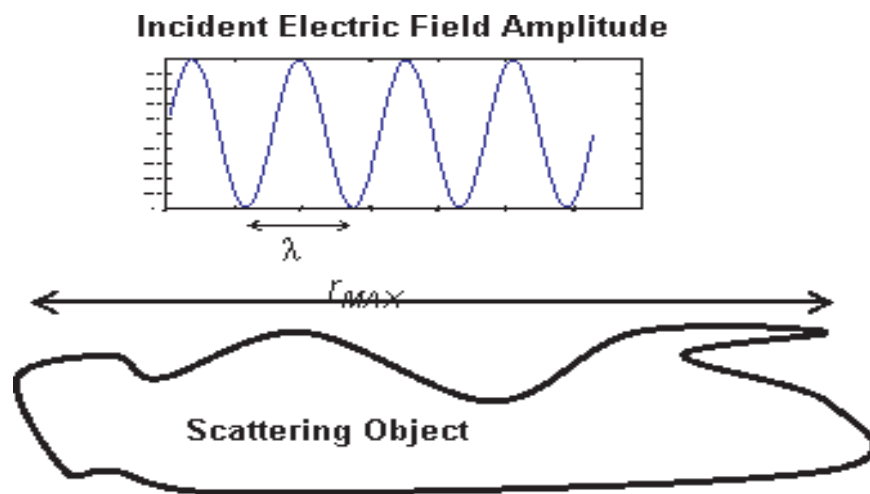
Figure 1-2: Full-wave Scattering Analysis: The amplitude of the incident source field and interactions between distant panel pairs on the geometry vary significantly ($r_{MAX} > 8\lambda$) over the diameter of the scattering object necessitating careful consideration of full-wave effects.

ment of impedance and scattering models from Integral Equations, describe standard Model Order Reduction techniques, and summarize sparsification methods, focusing on the Precorrected Fast Fourier Transform algorithm. Chapter 3 discusses the limitations of pre-existing Model Order Reduction techniques when used for full-wave electromagnetic analysis. Then, chapters 4 through 10, which comprise the main technical contributions of this research, present the Segregation by Primary Phase Factors (SPPF) algorithm, extensions to SPPF for sources that have complicated frequency dependencies, multi-point full-wave MOR methods for SPPF, extensions to SPPF for output selection vectors that have complicated frequency dependencies, a Precorrected Fast Fourier Tranform algorithm incorporating SPPF for full-wave MOR (FMOR), methods and ideas for multi-parameter FMOR, a new formulation and technique to improve conditioning, and related ideas, as well as results from applying these techniques to a variety representative sample problems.

## 1.1 Introduction to Full-wave Impedance Extraction

As predicted by Moore's Law, feature sizes have continued to decrease allowing more and more components in a System-on-Board (SoB) or System-on-Package (SoP). At the same time, frequencies generated within many of the systems have risen into the Gigahertz (GHz) ranges. With the increasing complexity of SoB and SoC components, the boards and packages will require the same or more amount of interconnect. While these interconnect geometries are not decreasing in size, the steady decrease in system operating wavelengths has driven many impedance extraction problems from the quasi-static regime into the full-wave regime by increasing the ratio of the maximum diameter of the interconnect geometry relative to the source signal wavelength, such that the ratio approaches, or even grows larger than, one.

The geometries in these full-wave impedance extraction problems are termed "electromagnetically large" when analyzed at full-wave wavelengths. In both quasi-static and full-wave modes of operation the magnitude of potentials induced by currents and charges on segments of interconnect are proportional to $1/r$, where $r$ is the distance from the source currents and charges. For quasi-static modes of operation, voltage differences induced along distant structures are exceedingly small since $1/r$ is smooth for large $r$, and the change in $1/r$ along the distant structure is negligible.

For full-wave modes of operation, impedance extraction for "electromagnetically large" interconnect geometries must take retardation effects into account when computing impedance models because retardation can cause interference in distant portions of the system that would be unaffected in quasi-static modes of operation. Due to the retardation effects, full-wave interconnect signals can induce significant voltage differences, up to $1/r$ in magnitude, along distant structures that are "electromagnetically large". Thus, during quasi-static modes of operation component charge and current densities will transmit electric and magnetic fields to adjacent portions of the system that can affect operation of the system, but in full-wave modes of operation, components will transmit electromagnetic waves that induce retarded potentials that

18

result in voltage differences even in distant portions of the system.

Depending on the geometry and properties of each component and its neighbors in the system, the effects of interference on that component's various operations will differ, but signals traveling through these systems at these Gigahertz frequencies will transmit significant levels of interference from components such as pins and wires to every other component of the chip. The increase in frequency and complexity of SoB's and SoP's has mandated ever more detailed, in-depth Electromagnetic Interference (EMI) analysis [10] for these sorts of electronic systems. In order to ascertain how EMI will affect operation of an electronic system without actually building the system, it is crucial to simulate the system in all of its potential modes of operation. Accurate simulation of the system requires detailed models for every component of the system, and these models must incorporate the effects of EMI.

Tools such IES3 [26], FastImp [46], FastCap [29], and FastPep [24] can extract detailed quasistatic impedance models by discretizing an Integral Equation (IE) formulation [19, 20], using Laplace Green's functions in the kernel, derived from the applicable set of Maxwell's Laws. Discretization of the IE governing the quasistatic frequency domain operation of the system generates a system of linear equations whose elements are polynomial or rational functions of frequency. Figure 1-3, shows an example of interconnect, discretized into small panels. For full-wave impedance analysis, IE formulations of Maxwell's Laws utilize Helmholtz oscillatory Green's functions for the kernel to capture the full-wave effects. Extraction tools, such as such as IES3[1] [26] and FastImp [46], also can discretize IE formulations of this type to generate impedance models, comprising of linear systems whose elements are polynomial functions of the product of frequency and complex exponentials of scaled frequency. It is the complex exponential term which accounts for oscillatory retardation effects.

Extracted linear systems will approximate the frequency domain behavior of the original system but the matrices are usually so large that the impedance model's computational complexity precludes simulation. Boundary Element Methods (BEM)

---

[1]IES3 is not suited for highly oscillatory kernels due to the fact that it depends on asymptotically smooth variation of the kernel for its compression techniques. Therefore, it may be not useful for electromagnetically large structures that are many wavelengths in diameter.
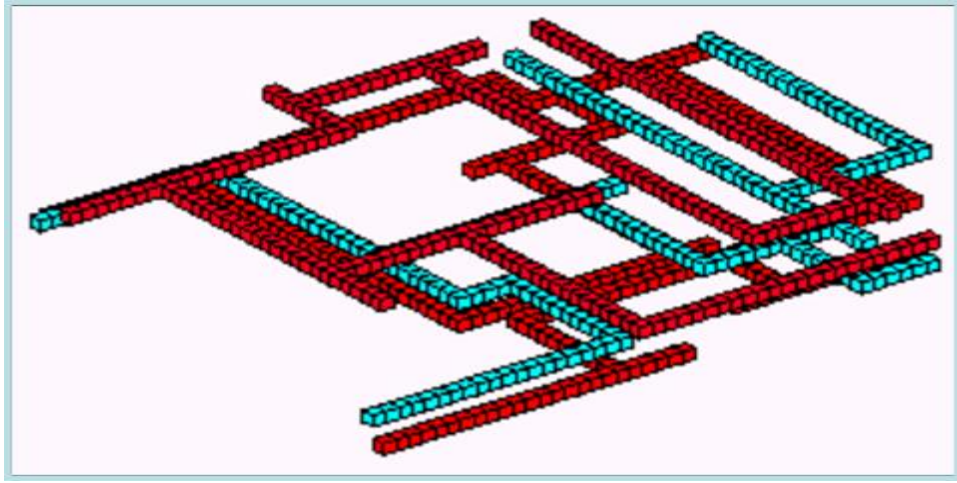
Figure 1-3: Interconnect: This figure is borrowed with permission from Michael Chou

applied to discretize Integral Equations (IE) formulations can reduce computations using Green's formulas and boundary conditions to construct Surface Integral Equation (SIE) based formulations. However, while the resulting matrices are smaller relative to differential equation based formulations, the matrices resulting from discretizing SIEs are very dense. Therefore, the computation required to accurately solve complicated systems and calculate desired unknowns at specific single frequency points is frequently too time-consuming to feasibly aid the design process. To permit simulation, IE-based tools dramatically accelerate computations by utilizing iterative methods [40] to solve the system in unison with "sparsification" algorithms [17, 16, 4] that approximate the discretized model of the original system, when computing matrix-vector products. For example, FastImp employs the Precorrected Fast Fourier Transform (PFFT) [36] sparsification algorithm. The BEM IE-based EM scattering solver implemented for this research incorporates the PFFT algorithm with iterative techniques. The impedance extraction solver used with this research relies on iterative solution techniques alone.

However, system complexity has increased at such rates that the extracted impedance models are often too large for simulation purposes, even when tools utilize sparsification algorithms to solve the system. Therefore, the extraction tools also incorporate

Model Order Reduction techniques to generate low order impedance models that capture the frequency behavior of the original system but can be rapidly solved at any desired point in the system's operating frequency range [18, 14, 42]. Standard MOR algorithms have been extended [34] to account for the oscillatory retardation kernel required for analysis in the full-wave regime, and can generate low order models to characterize the full-wave impedance behavior of a system. We briefly review these full-wave MOR algorithms in section 2.7. However, the accuracy of these methods hinge on the worst case interaction distances, severely limiting their performance. Furthermore, at high frequencies, computation required to utilize these full-wave MOR techniques, becomes very costly, perhaps infeasible, for many geometries and operating conditions.

Chapter 4 presents the Segmentation by Primary Phase Factors (SPPF) algorithm, which can be used to approximate the original system and transform the equations into a form that is suitable for full-wave Model Order Reduction (SPPF-FMOR). In SPPF-FMOR, the accuracy of the underlying truncated Taylor series approximation to the system is bounded by the value chosen for the SPPF parameter $\check{R}$. Because the truncation error is decoupled from the worst-case interaction distances, SPPF-FMOR enables greater accuracy in reduced order models than [34] for a given truncation order, and the SPPF-FMOR ROMs have a much wider frequency band of accuracy. Furthermore, SPPF-FMOR requires less computation[2] to achieve a given level of accuracy. Thus, SPPF-FMOR makes it feasible to characterize the frequency behavior of many more systems with these extraction tool than was possible before using the methods in [34].

Chapter 6 presents options for SPPF-based multi-point MOR, which is necessary to extend the frequency range of accuracy for a ROM by adding terms to the projection matrix corresponding to additional Taylor expansion points of the system. Chapter 8 describes an algorithm to implement the key concepts from SPPF-FMOR in conjunction with the PFFT sparsification algorithm to accelerate matrix-vector

---

[2]For many full-wave problems, the number of operations required for MOR (both for SPPF-FMOR and [34]) is approximately proportional to the truncation order, $n_T$.

products to generate a low-order model of the original system that may be solved at any points in the specified frequency range to obtain an accurate approximate solution and dramatically improve full-wave impedance analysis of electronic systems. Finally, Chapter 10, presents a new formulation suited for full-wave MOR and some techniques to achieve better conditioning.

## 1.2    Introduction to Full-wave Electromagnetic Scattering

Accurate computer analysis of electromagnetic scattering of complex objects can be achieved with SIE formulations, derived from Maxwell's Laws, that generate complicated models. The second application for this thesis research is to develop algorithms to efficiently generate reduced order models (ROMs) that accurately characterize the resulting scattered Electromagnetic (EM) fields produced when full-wave incident source fields interact with the surface of a complex target object, as illustrated in figure 1-4, over a desired full-wave frequency range. Full-wave source signals incident on a scattering geometry can induce significant interactions even between distant points in the scattering geometry. Figure 1-2 highlights the scale of the oscillations for EM-Large structures. The key difference in the full-wave interactions is that, although the amplitude of induced potential is very small at distant portions of the scattering structure, the retardation causes voltage differences that cause significant currents. This phenomenon is not present in quasistatic frequency ranges.

A difficult problem for full-wave electromagnetic scattering analysis is to compute accurate results over entire ranges of selected parameters, such as frequency and look angle, when the scattering object is "electromagnetically large" (EM-Large)and has geometrical dimensions much greater than wavelengths of interest. In particular, using BEM SIE solvers, a large number of basis functions are needed to accurately approximate the unknown surface quantity of interest, and existing full-wave MOR methods are not able to efficiently generate a single low order model that accurately

characterizes an EM-Large system for a sufficiently wide frequency range. Existing MOR methods can be used to generate multiple models, each accurate over a (narrow) frequency band. Thus, a composite ROM could be constructed from the piece-wise accurate narrow-band ROMs for inverse scattering.

However, the approach of characterizing the desired frequency range by stringing multiple narrow-band models together has a negative impact on computational efficiency due to the cost of constructing multiple ROMs. Furthermore, the composite ROM approach becomes unwieldy and infeasible when trying to characterize a system for multiple parameters of interest, such as frequency, look angle, and geometrical parameters. Thus, it is desirable to have a single ROM that accurately characterizes the system over the desired frequency range, and an improved full-wave MOR (FMOR) algorithm might have great potential to facilitate a number of challenging inverse-scattering type applications, such as metrology for semiconductor packages, design of stealth military weapons systems, iterative designs of antennas, automatic target recognition, and matching waveforms for both transmitters and targets.

The portions of this dissertation that are pertinent EM scattering are organized as follows: Chapter refbckgrnd presents background material necessary to better comprehend the nature of the CEM challenges and describes the formulations used in this dissertation for computational scattering. Two popular formulations, which can be used to produce accurate results for selected problems, are the Electric Field Integral Equations (EFIE) and the Combined Field Integral Equations (CFIE). Background sections 2.1- 2.3 review these formulations and trace their development from the appropriate set of Maxwell's Laws, and section 2.5 presents techniques to discretize systems of field integral equation into linear (with respect to unknown sources) equations that can be solved on a computer.

For this thesis research, we have chose to design a system that implements and solves the EFIE discretized with RWG [38] linear basis functions, in the frequency domain. The resulting linear system approximates the frequency domain behavior of the original system but the matrices are usually so large and dense that the scattering model's computational complexity precludes rapid solution. To characterize
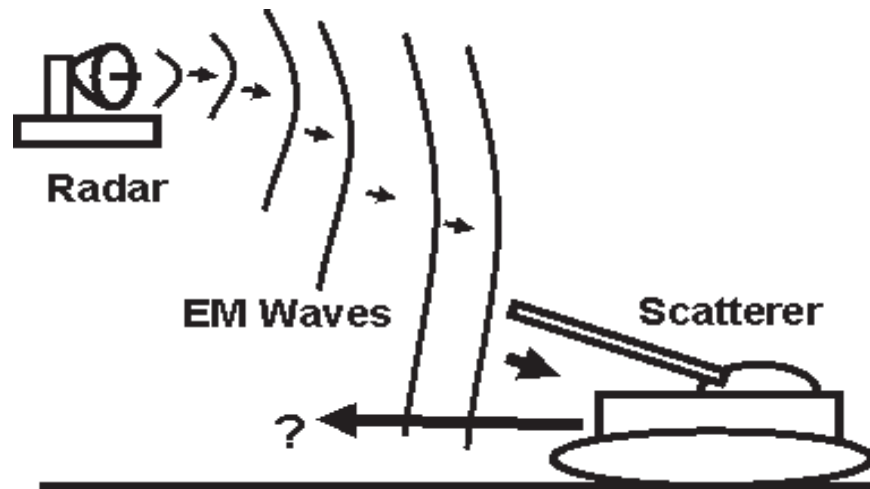
Figure 1-4: EM scattering analysis involves determining scattering quantities of interest, such as induced currents on the target, radar cross section (RCS) of the target, or scattered fields, due to an incident EM wave impinging on a scattering target. In the picture, the distant radar (perhaps on an airplane) is the source of the EM wave that impinges on the tank. The tank is the scattering target and the goal is to determine the scattering quantities of interest due to EM waves scattering from the tank. A common goal is solve for scattered fields at observation points of interest (frequently, observation points are located at the source antenna). An BEM SIE EM analysis tool would discretize the surface of the tank, in similar fashion to the interconnect pictured in figure 1-3.

scattering from a target structure over an entire parameter range, these tools dramatically accelerate solution of the system and further approximate the already-discretized model by employing "sparsification" algorithms in unison with iterative methods [40], which are reviewed in section 2.6.4.

Since the system equations and source field vector have complicated parameter dependencies, solving the large EFIE systems of equations across entire multidimensional parameter ranges is a costly computational task, but the combination of sparsification and MOR can meet this challenge. Traditional MOR methods are reviewed in section 2.7. However, EM-Large scattering geometries (full-wave problems) pose a particularly difficult computational challenge for scientists interested in simulating full-wave scattering applications since these problems are not very amenable to the existing MOR techniques. These challenges for full-wave MOR are discussed in chapter 3 and provide the motivation for the new algorithms and other contributions offered in this dissertation.

Chapters 4 through 10 presents all of the major contributions of our research. The main contribution is to propose several new algorithms and techniques to facilitate full-wave MOR (FMOR). The core algorithm which serve as the foundation of these new FMOR algorithms and techniques is called Segregation by Primary Phase Factors (SPPF) and is presented in Chapter 4. Chapters 5 and 7 discusses how to extend the SPPF-FMOR algorithms developed for Impedance Extraction (which usually has a frequency-independent source vector) to efficiently generate accurate low order models for Electromagnetic scattering that account for the complicated frequency-dependencies of the incident source field vectors and output selection vectors. Chapter 6 presents new multi-point SPPF-FMOR algorithms that generate ROMs which have great accuracy around multiple expansion points, and thus can expand the frequency range of a ROM's accuracy. Chapter 8 shows how SPPF-FMOR for Electromagnetic Scattering may be extended to incorporate sparsification techniques which are critical for simulating complex geometries. Finally, chapter 9 discusses ideas for generating multi-parameter reduced order models and presents algorithms for multi-parameter FMOR that generate ROMs with frequency and look

angle parameters.

# Chapter 2

# Background

This chapter provides the context necessary for the reader to understand the new algorithms, presented in Chapters 4 to 10, that are the main contributions of this dissertation research. Specifically this chapter will discuss how EM analysis tools construct the original, parameter-dependent[1] models for a system, how sparsification algorithms can accelerate the solution of those models at a single parameter point, and how traditional MOR techniques can generate reduced order models (ROMs) that allow rapid characterization of the parameter-dependent behavior of the system. Much of the background material will be presented in the context of the scattering application because scattering problems usually have sources and output functions that have complicated frequency dependencies, leading to a more general model order reduction problem than the impedance extraction application.

This chapter is organized as follows: An Integral Equation formulation is developed in sections 2.1- 2.4. Then, section 2.5 illustrates how to discretize the equations to produce a linear system. Section 2.6 demonstrates how sparsification can be used to rapidly solve the system at a particular parameter point. Finally, Model Order Reduction (MOR) methods are presented in section 2.7. MOR is used to generate a low order model that characterizes the behavior of the original system over a desired parameter range for certain parameters of interest and that can be rapidly solved. If

---

[1] Model parameters typically include frequency. Zenith look angle, azimuth look angle, and geometrical parameters (width, height, length) are other possible parameters of interest

the reader is interested in exploring any of the background topics in more detail, there is a wealth of literature on these topics. The reader can learn more about EM solvers in [26, 46, 25, 29, 23], discretization in [19, 38], Sparsification in [36, 8, 2, 43, 4], and MOR in [18, 5, 30, 34, 12, 42, 13, 37, 9].

## 2.1 Establishing Governing Equations

To accurately analyze the EM behavior of an arbitrary structure, CEM solvers typically generate a model of the original system based on Maxwell's Laws, which relate macroscopic EM fields and sources:

$$\nabla \cdot \overline{B} = 0 \tag{2.1}$$

$$\nabla \cdot \overline{D} = \rho_E \tag{2.2}$$

$$\nabla \times \overline{H} = \frac{\partial \overline{D}}{\partial t} + \overline{J_E} \tag{2.3}$$

$$\nabla \times \overline{E} = -\frac{\partial \overline{B}}{\partial t}. \tag{2.4}$$

In the preceding Maxwell's equations, $\overline{E}$ is electric field , $\overline{H}$ is magnetic field, $\overline{J_E}$ electric current density, $\rho_E$ is electric charge density. $\overline{D}$ is electric displacement , and $\overline{B}$ is magnetic induction. Maxwell's laws are partial differential equations (PDEs) that include derivatives with respect to position and time. Constitutive relations, relating magnetic induction to the magnetic field and electric displacement to the electric field in materials composing the structure, and boundary conditions, at interfaces of the structure to be analyzed, provide additional relations that can be used to to solve for unknowns of interest given sufficient known source terms.

## 2.2 Formulation for Electromagnetic Scattering

There are many ways that a CEM solver can use Maxwell's Laws to construct a model for a structure of interest. A particular set of choices that specify how to construct a model constitute a "formulation" for analysis of the Electromagnetic properties of the structure. This section will first present several of the possible basic choices for formulating the problem, and then present the formulation adopted for this research.

One can classify CEM solvers by whether the solver models the behavior of the system in the time domain or the frequency domain. Time-domain (TD) solvers often employ time stepping methods (Runga-Kutta, Euler, Richardson Extrapolation, Predictor-Corrector, etc) to analyze the time evolution of the system. Frequency domain solvers transform Maxwell's PDEs from the time domain into the frequency domain, using Fourier Transformation, which is useful when a goal of the analysis is to characterize the frequency behavior of a system. A frequency domain solver was developed for this research since one of the main goals of both Computational EM scattering and Impedance extraction applications is to characterize the frequency behavior of systems. Therefore, using Fourier Transformation, the PDEs with derivatives with respect to time and position coordinates, Equations 2.3 and 2.4, can be converted to PDEs with derivatives with respect to position variables only:

$$\nabla \times \overline{H}(\overline{r}) = i\omega\epsilon_R\epsilon_0\overline{E} + \overline{J}_E \tag{2.5}$$

$$\nabla \times \overline{E}(\overline{r}) = -i\omega\mu_R\mu_0\overline{H}. \tag{2.6}$$

Note that these equations were formulated under the assumption that the fields and sources are functions of position and time, and that permittivity and permeability are constant with respect to time. Also, they introduce relative permittivity[2] and relative permeability[3].

Clearly, the goal of any EM analysis is to seek a solution that satisfies Maxwell's

---

[2] $\epsilon_R = \epsilon/\epsilon_0$
[3] $\mu_R = \mu/\mu_0$

Laws for the geometry in question, and there are many ways to accomplish this. Invariably, due to finite and discrete nature of computer computations, a CEM solver will approximate the geometry of the original system and approximate the solution space and/or the operators of Maxwell's Laws. Further classification of EM solvers involves differences in the way the known and unknown quantities are "discretized" or converted from continuous functions to the discrete representations that the computer can work with.

Finite Difference methods [1] discretize the geometry of the structure with spaced grid points that representing the field and source values at those positions. Grid points must be positioned with regular spacing throughout the volume and surrounding space. Finite Difference solvers approximate the differential operators of Maxwell's Laws by computing finite differences using the grid point field quantities and the corresponding grid point distances. The unknowns in a Finite Difference model are grid point quantities (field or source, depending on the problem). The matrices in the systems of equations generated by Finite Differences are very sparse, due to the finite difference approximation of the derivatives, but the grid points must be very finely spaced to achieve accuracy. The matrices are very large since unknown and known quantities must be defined throughout the structure and surrounding volume. Furthermore, since, the grid points do not necessarily coincide with boundaries, the specification of boundary conditions can be complicated for Boundary Value Problems (BVPs).

Finite Element Method (FEM) methods [32] place "elements" described by vertices (points) throughout the volume of the geometry of the structure and surrounding space, but the points can be arbitrarily spaced. Instead of representing field and source quantities at the points, the structure is discretized by the elements, composed of a collections of points that form a volume. Thus, elements can be defined so that surface of the structure is fully represented the surfaces of elements that form the exterior of the structure's volume, so FEM does not share the difficulty modeling BVPs with Finite Differences. For each element a 3-dimensional basis function is defined that locally approximate field quantities inside the volume enclosed by the element's

points. Thus, the basis function defined by an element is nonzero only within the corresponding sub volume, and the weighted sum of all the elements approximates the field and source quantities over the entire volume of the problem space. Note, that FEM methods approximate the known and unknown quantities, and FEM model unknowns are the weighting coefficients that correspond to the basis functions that represent the unknown locally within each element. While FEM does not approximate the differential operators, it satisfies them only in a "variational" sense, rather than a pointwise sense [32]. Since the FEM system equations result from enforcing (variationally) a differential form of Maxwell's Laws over the volume enclosed by each of the element basis functions, the matrices in the systems of equations are very sparse, but also very large since unknown and known quantities must be defined throughout the structure and surrounding volume.

Boundary Element Methods (BEM) [3] require formulating Maxwell's Laws in integral form, and the resulting integral equations (IEs) are transformed into surface integral equations (SIEs), either by application of Green's theorem or applying a surface equivalence principle. The SIEs are discretized in similar fashion to FEM except that element vertex points are only defined on the surface of the structure, and, therefore, elements are two-dimensional, defined on patches on the surface of the structure. Higher order panels are possible, but triangular patches or panels are commonly used for EM analysis, in which the vertices are defined by three of the surface grid points. Basis functions, each defined to be nonzero only on its corresponding surface panel, are used to approximate the fields and sources locally on the surface panels. Obviously, the weighted sum of all the basis functions will approximate quantities over the surface of the entire structure. Clearly, SIEs are very natural to model BVP's. The matrices formed by BEMs for SIEs are very dense, but since knowns and unknowns are only defined on the surface of the structure, SIE formulations can reduce the number of unknowns dramatically.

For many electromagnetic scattering problems, source electric currents produce incident waves that travel, impinge, and scatter from the scattering object, but the sources themselves are very far away. For this research, we have selected a SIE

31

formulation of Maxwell's Laws known as the Electric Field Integral Equation (EFIE) [38, 39], and by using the BEM to discretize the EFIE will eliminate the need to discretize the entire volume space of the problem. Since radars are often very far from the scattering targets, this BEM approach will reduce the resulting model size tremendously, as only the surface of the scattering target will need to be discretized, and not all of the three-dimensional space between the radar and target.

## 2.3    Tailoring Equations for problems of interest

This section presents some of the basic theory and methodology for implementing the EFIE. An excellent resource for a more in depth development of the EFIE and other formulations is [28]. The rationale for choosing to implement the EFIE was mainly for simplicity and to save programming effort. Furthermore, SoB and SoP interconnect and many EM scattering problems of interest involve analysis of "perfect electric conductor" (p.e.c.) type structures, for which the EFIE is suitable.

As described in the literature [33], for certain problems, solutions to the EFIE and Magnetic Field Integral Equation (MFIE) will not have unique solutions and the resulting EM solver model matrices will approach singular at resonant frequencies. The Combined Field Integral Equation (CFIE) formulation, combines the MFIE and EFIE, preventing this problem, but our algorithms and results are tested on the implemented EFIE solver. The reader can consult [33] and [28] to see that extending the new algorithms developed in this research to MFIE and CFIE implementations would require only minimal modifications.

To study scattering due to incident wave excitation, it is helpful to separate the fields outside the conductor into two components: the incident fields $\overline{E^{INC}}$ and the scattered field, $\overline{E^{SC}}$:

$$\overline{E}(\overline{r}) = \overline{E^{INC}} + \overline{E^{SC}}, \tag{2.7}$$

The gradients of electric scalar potential $\Phi_E$ and magnetic scalar potential $\Phi_M$ are

defined as follows:

$$-\overline{\nabla \Phi_E}(\overline{r}) = \overline{E^{SC}}(\overline{r}) + i\omega\mu_0 \overline{A}(\overline{r}) - \nabla \times \overline{F}(\overline{r}) \tag{2.8}$$

$$-\overline{\nabla \Phi_M}(\overline{r}) = \overline{H^{SC}}(\overline{r}) + i\omega\epsilon_0 \overline{F}(\overline{r}) - \nabla \times \overline{A}(\overline{r}), \tag{2.9}$$

where $\overline{A}(\overline{r})$ is the vector electric potential and $\overline{F}(\overline{r})$ is the vector magnetic potential[4]. For our solver and the p.e.c. problems under consideration, the $\overline{F}(\overline{r})$ terms are assumed to be zero[5].

By taking the curl of equation 2.9, the unknown electric vector potential is related to the unknown current densities near the surface of the conductor by the inhomogeneous vector Helmholtz equation:

$$\overline{\nabla^2 A}(\overline{r}) + k^2 \overline{A}(\overline{r}) = -\overline{J}_S(\overline{r}) \tag{2.10}$$

By taking the divergence of equation 2.8, and applying the Lorentz gauge conditions [22], the unknown electric scalar potential is related to the unknown current densities near the surface of the conductor by the inhomogeneous scalar Helmholtz equation:

$$\nabla^2 \Phi_E(\overline{r}) + k^2 \Phi_E(\overline{r}) = -\frac{\rho_S(\overline{r})}{\epsilon}. \tag{2.11}$$

Note that the sources, surface charge $\rho_S(\overline{r})$ and surface current density $\overline{J}_S(\overline{r})$, are surface quantities because we will use the EFIE to analyze p.e.c. structures for which skin-depth is negligible. However, the Surface Equivalence Principle and Volume Equivalence Principle, discussed in [28], can be used to derive identical equations for more general problems involving non-p.e.c structures, which may have significant skin-depths, but, in such cases, the surface quantities are fictitious "equivalent" sources used to simplify analysis by "homogenizing" the problem domain.

---

[4]$\overline{F}(\overline{r})$ arises from employing Volume Equivalence principles (see [28]) to simplify problems with inhomogeneities by accounting for material properties with fictitious volume sources

[5]This assumptions is convenient to simplify implementation of a EM solver, but using a MFIE or CFIE solver to examine more general classes of EM analysis problems should not significantly alter the new algorithms contributed by this dissertation

## 2.4 Converting PDE's to Integral Equations

Currents only flow along the surface of perfect conductors. Green's functions derived for the Helmholtz (homogeneous ODE) operators can be used to solve the vector potential in terms of a Fredholm integral equation representing the convolution of the Green's function and the unknown surface current, as shown:

$$\overline{A}(\overline{r}) = \oint_S \overline{J}(\overline{r}')G(\overline{r},\overline{r}')dS(\overline{r}'). \tag{2.12}$$

Green's functions derived for the Helmholtz (homogeneous ODE) operators can also be used to solve the scalar potential in terms of a Fredholm integral equation representing the convolution of the Green's function and the divergence unknown surface current, as shown:

$$\Phi(\overline{r}) = \oint_S \rho_S(\overline{r}')G(\overline{r},\overline{r}')dS(\overline{r}') = \oint_S \frac{\nabla \cdot \overline{J}_S(\overline{r}')}{i\omega\epsilon}G(\overline{r},\overline{r}')dS(\overline{r}'), \tag{2.13}$$

in which current continuity is enforced to yield the 2nd equivalence containing the divergence of the surface current density as the unknown.

The Green's function for the Helmholtz equation 2.10 is

$$G_H(\overline{r},\overline{r}') = \frac{e^{-ik\|\overline{r}-\overline{r}'\|}}{\|\overline{r}-\overline{r}'\|}. \tag{2.14}$$

In the next section, boundary conditions will be applied to derive equations that can be used to solve for the unknown surface current densities induced by known incident source fields.

### 2.4.1 Applying boundary conditions for perfect conductors

All magnetic and electric fields are zero within the volume of perfect conductors, as a field in the interior would imply infinite current densities there. However, currents can exist at the surface of conductors, described by the following boundary conditions:

$$\overline{n} \times (\overline{E^{INC}}(\overline{r}) + \overline{E^{SC}}(\overline{r}))_{\overline{r}\in S^+} = 0 \tag{2.15}$$

where $S^+$ refers to points just exterior to the surface of the conductor. Substituting integral equations 2.12 and 2.13 to eliminate the scalar and vector potential terms in equation 2.8 and using the result to replace the scattered Electric Field $\overline{E}_{SC}$ in equation 2.15 yields the electric field integral equation (EFIE):

$$\overline{n} \times \overline{E^{INC}}(\overline{r}) = -\frac{\overline{n}}{i\omega\epsilon_0} \times (\nabla\nabla' \cdot \oint_S \overline{J}(\overline{r'})G(\overline{r},\overline{r'})dS(\overline{r'}) + k^2 \oint_S \overline{J}(\overline{r'})G(\overline{r},\overline{r'})dS(\overline{r'})),$$
(2.16)

which relates the unknown surface current density, $\overline{J_S}$, to the known incident excitation, $\overline{E^{INC}}$ (usually plane waves), evaluated at the surface. The EFIE is a Fredholm IE of 1st kind. The EFIE 2.16 has a translationally invariant kernel (equation 2.14) and can be considered a convolution. Although the EFIE is formulated specially for the p.e.c. case, similar surface IE's can be developed for other scatterers through application of the surface equivalence principle [28].

## 2.5 Discretization Techniques for Integral Equations

A computer cannot solve the Electric Field Integral Equation for the unknown surface current density exactly because the surface current density is a continuous function of position and its value at each position coordinate is unknown. Furthermore, the known incident source wave is also continuous, since the EFIE can be evaluated at any observation point. Therefore, the EFIE has an infinite number of unknowns and represents an infinite number of equations. By employing a BEM-based discretization procedure, the integral equations can be converted into a finite linear system of equations which approximate (except at selected quadrature points where the approximation is exact) the original system.

With the Method of Moments (MoM) [19, 28, 27] discretization technique, a set of basis functions and a set of testing functions are selected to create an approximation to the original EFIE. First a set of $n_B$ basis functions are chosen to approximate the

desired unknown quantity:

$$\overline{J_S}(\overline{r}) \approx \sum_{n=1}^{n_B} J_n \overline{f_n^B}(\overline{r}) \tag{2.17}$$

Due to the integrals, the $n_B$ current density coefficients become new unknowns that approximate the unknown current density function by scaling the selected basis functions. This approximation is substituted in the original equations to replace the unknown current density. Second, $n_T = n_B$ testing functions are selected and used to "test" the equations by taking the inner product of the $mth$ testing function $f_m^T$ with the approximate EFIE equations (integrating the approximate EFIE equations multiplied by the testing function corresponding to the resulting $mth$ row of the discretized, linear equations).

The resulting $(m, n)$ entry of the discretized linear system from the two step discretization process of basis function approximation and testing is

$$\oint_S \overline{f_m^T}(\overline{r}) \cdot \overline{n} \times \overline{E^{INC}}(\overline{r}) dS = \tag{2.18}$$

$$\sum_{n=1}^{n_B} J_n \oint_S \oint_{S'} \nabla' \cdot \overline{f_n^B}(\overline{r'}) \overline{f_m^T}(\overline{r}) \cdot \overline{\nabla G(\overline{r}, \overline{r'})} + (s)^2 \overline{f_m^T}(\overline{r}) \cdot \overline{f_n^B}(\overline{r'}) G(\overline{r}, \overline{r'}) dS' dS,$$

or in matrix notation: $\boldsymbol{Z}(s)\boldsymbol{J} = \boldsymbol{E^{INC}}$. $\boldsymbol{J}_n$ is the coefficient for the $nth$ basis functions, $\overline{f_n^B}$, and $\boldsymbol{E^{INC}}$ are the inner product of the testing functions and the incident excitation field vector. The testing functions, $\overline{f_m^T}$, should be linearly independent and the basis functions should be chosen such that the range space of the integral operator for each basis function is linearly independent of that of the other basis functions, so that a solution exists for the set of linear equations resulting from the method of moments discretization, and is unique. The result is one equation relating the known incident excitation field to the unknown basis function coefficients at all of the surface points.

Approximating the unknown current density with the basis functions corresponds to satisfying the approximate EFIE on the union of the sub-surfaces (panels), rather

36

Discretization of Sphere:48 panels
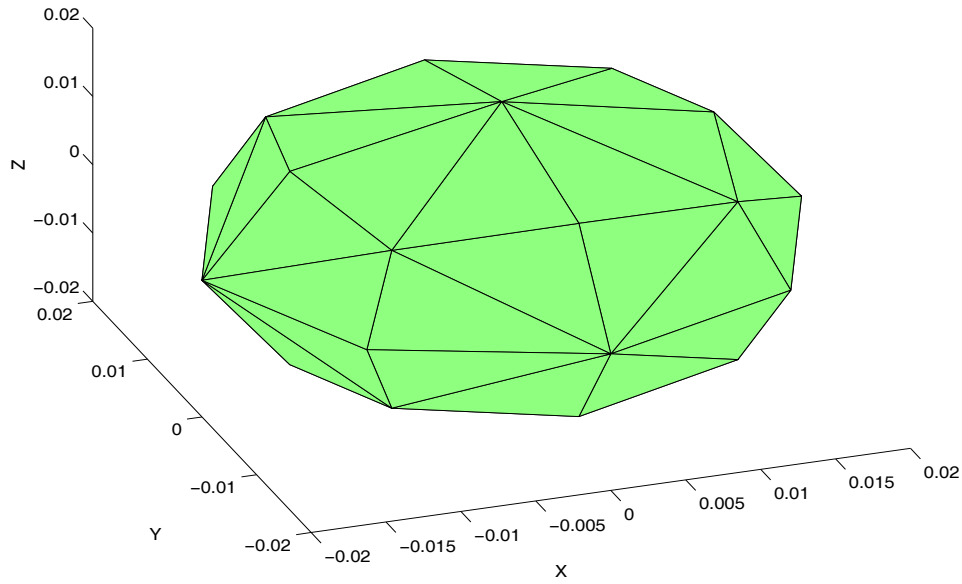
Figure 2-1: Discretization of a sphere is accomplished by introduction of basis functions each supported (non-zero) on a small surface patch that approximates a corresponding portion of the original geometry and zero everywhere else. The EFIE-based solver used in this research approximates the surface of the geometry (a sphere in this case) with the triangular panels. The figure shows the manner in which a sphere might be discretized using basis functions supported on flat triangular panels, which define regions of support associated with each of the basis functions. Panel vertices are located on the original surface and the triangular panels approximate the portions of the original sphere to which each corresponds. Each of the basis functions that are used to approximate the unknown current density is supported on the two triangular patches or flat panels corresponding to a single edge and zero everywhere else. The EFIE-based solver computes both the original EFIE integration and the testing integration (that is required to discretize the original EFIE) over the approximate surface reprented by the union of the triangular panels.

than enforcing the EFIE on the exact surface of the original geometry. Employing the testing process to discretize the EFIE forces the EFIE to be satisfied in some sort of "average" sense over each of the approximate sub-surfaces (panels), rather than at each point.

There are other ways to accomplish discretization. For example, It is possible to choose high order functions, supported over the entire surface, for testing and basis functions. However, for an arbitrary geometry, it would be difficult to construct these function sets to meet all the conditions and with sufficient span of the domain and range space to approximate the unknown or known quantities effectively (as hard as solving the original problem analytically). By breaking the arbitrary geometry into very small, similar subsections as shown for a sphere example in figure 2-1, it becomes feasible to consider constructing a function that is a linear combination of lower order functions each with closed support on individual panels to approximate the known and unknown quantity on each subsection of the geometry and satisfy the governing equations and conditions. Intuitively, it seems if panels are selected to have a sufficiently small diameter relative to both the wavelength and the feature size, then the unknown (current) and known incident field might be smooth enough over the dimensions of one panel to be approximated by a lower order functions.

Why is the testing step necessary? To solve for the unknowns it is necessary to have one equation for each unknown, but in this case, after substituting the current density approximation (equation 2.17) into the EFIE, there is a different linear equation for every surface point, and thus, an infinite number of equations relating the $n_B$ unknowns, or the system is still over-determined. One specific example of the "testing" step is to partition the surface into $n_B$ roughly equal sized panels[6] and choose an evaluation point at the centroid of each panel, forcing the equations to be exact at those "testing" points. This is the equivalent of choosing the testing functions to be $n_B$ delta functions, centered at the selected surface panel centroid points, and integrating the product of each delta function with the terms in the approximated

---

[6]A panel can be described as a closed sets of surface coordinate points where the panel point set is pathwise and simply connected, meaning that a panel is not actually multiple separate regions of the surface and that there are no holes in the panel, respectively.

(by basis functions) IE[7] over the surface.

If the testing functions and basis functions are the same, $\overline{f_m} = \overline{f_m^B} = \overline{f_m^T}$, the discretization procedure is a Galerkin procedure. If each testing function has close support on different subsections of the geometry, then the discretization process is called the Method of Moments. Often, the testing and basis functions are not orthogonal sets. For example, while delta and pulse (constant panel) testing functions are orthogonal, linear and higher order testing functions often are not. If the testing functions are orthogonal, then discretizing the IE's in this manner forces the residual (difference between the exact and approximate tangent incident excitation fields) to be orthogonal to each of the testing functions, which will project the range space (the known incident field for the given EM scattering problems) to the closest function in the span of the testing basis set.

What constraints affect the selection [28] of the basis functions and testing functions? The basis functions are selected to span the domain space (possible current densities) of the integral equation within some given tolerance of the error norm. The basis and testing functions are chosen to satisfy conditions imposed by the governing ODE and boundary conditions and required "smoothness". These functions must be selected such that the resulting matrix equation has a solution. For example, if both basis and testing functions are the delta (impulse) function, centered at each panel, then the diagonal terms of the discretized system matrix, representing the self-panel contributions to the current density, will be infinite due to the singularity of the Helmholtz ( 2.14) and Laplace Green's functions used in the integral equations, and the system wouldn't have a solution. Using step basis functions, each supported on a single panel and zero elsewhere, helps eliminate the singularity problem, and linear basis functions would improve accuracy even further since they offer a higher order approximation.

Many formulations require derivatives of vector potentials and thus of the Green's function. The inner product of the testing function with the Green's function and

---

[7]EFIE 2.19 or MFIE with surface current density approximated by linear combination of the chosen vector basis functions $\overline{J_S}(\overline{r}) \approx \sum_{n=1}^{n_B} J_n \overline{f_n^B}(\overline{r})$

the original integral of the surface current density and the Green's function are each convolutions. The convolution operations commute with the derivatives such that one would expect each derivative order to increase the required "combined" order of the basis and testing functions by one. For example, 1st order derivatives of a pulse (constant panel) basis function would produce a delta function which combined with delta functions might produce problems as discussed earlier. Thus, to choose basis and testing functions it is necessary to take into account the details of the governing equations and boundary conditions.

### 2.5.1 Basis and Testing Functions for EM scattering

For this problem, the EFIE will be used to solve for the scattered fields (induced current density) due to an incident source field. The EFIE has a second order derivative (from gradient and divergence operators) and thus will require at least linear basis functions and pulse testing functions (or vice versa). To gain the advantages of a Galerkin MoM procedure (symmetry) and to improve accuracy even further, we will choose both the testing and basis functions to be linear. The first step in discretization of the IE is to utilize a linear combination of the basis functions to approximate the unknown quantity. For EM scattering, the unknown is the current density on the surface due to the incident source fields. It is approximated:

$$\overline{J_S}(\overline{r}) \approx \sum_{n=1}^{n_B} J_n \overline{f_n^B}(\overline{r}) \tag{2.19}$$

where $\overline{f_m^B}$ is the basis function, such that the unknown of the new, approximate integral equation are the coefficients $J_n$.

The RWG basis/testing functions [38] have many properties that are appropriate to approximate the current density on the surface of a scatterer. Each RWG function is associated with an edge between two panels and models the current in the panel that crosses that edge:
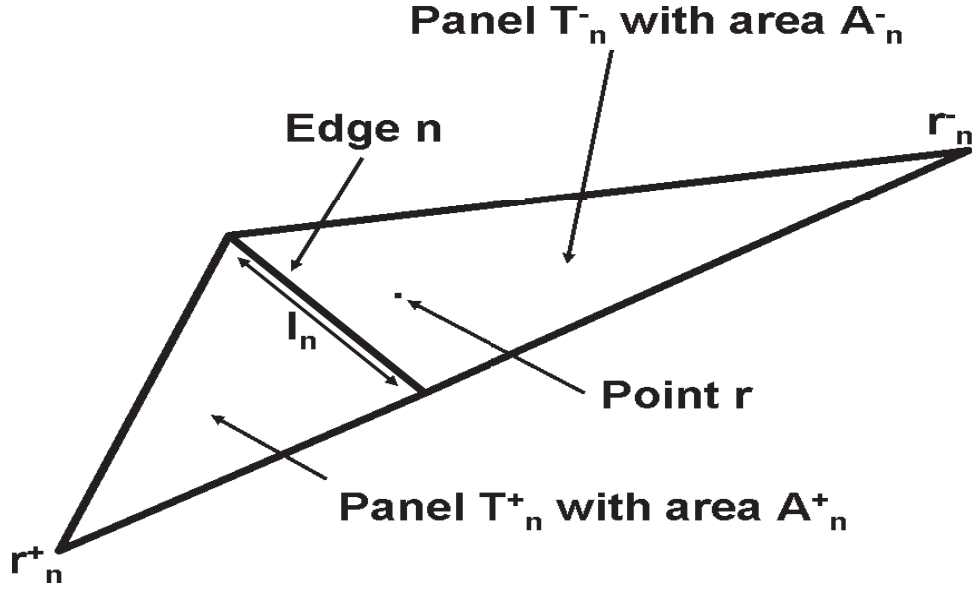
Figure 2-2: Each RWG basis function $\overline{f_n^{RWG}}(\overline{r})$ is associated is associated with an edge $n$ and the edge's two associated panels $T_n^-$ and $T_n^+$.

$$\overline{f_n^{RWG}}(\overline{r}) = \begin{cases} \frac{l_n}{2A_n^+}(\overline{r} - \overline{r_n^+}), \overline{r} \in T_n^+ \\ \frac{l_n}{2A_n^-}(\overline{r_n^-} - \overline{r}), \overline{r} \in T_n^- \end{cases} \tag{2.20}$$

where $T_n^+$ is the + panel (triangle) and $T_n^-$ is the - panel (triangle) associated with the $nth$ edge (and the RWG basis function, $f_n^{RWG}$, at that edge). $l_n$ is the length of the nth edge, $A_n^+$ is the area of the + panel associated with the nth edge, $A_n^-$ is the area of the - panel associated with the nth edge, $r_n^+$ is the vertex, opposite to edge $n$, of the + panel, and $r_n^-$ is the vertex, opposite to edge $n$, of the $-$ panel. These quantities are illustrated in figure 2-2.

The RWG function is always tangential to the discretized surface (panels), an appropriate property for approximating a surface quantity. At all edges on the boundary of the panel pair, the normal component (perpendicular to edges) of the function is zero, and the normal component of the RWG function is always constant with respect to position along the edge shared between the panels and is continuous, implying no charge density can accumulate at panel edges since there are no jumps allowed in normal current across any edge, as expected for continuity of current. The RWG function

41

has enough flexibility to model a variety of simple current flows. For example, it is easy to show how to combine the three basis functions of any panel to produce a constant current flow of any magnitude and any direction across the panel. Since it has a variety of useful properties for solving EM scattering problems, the RWG basis function will be used in this formulation.

The final step in discretization of the IE's is to "test" the IE with the testing (same as basis functions for Galerkin procedures) function or integrate each basis function with the terms on both sides of the IE, producing another linear equation for each testing function. This results in a linear system of equations where the unknowns in each equation are the coefficients introduced by the basis function approximation to the current density. Following these steps, the fully discretized form of the EFIE is

$$\boldsymbol{E} = \int_S \boldsymbol{f}(\overline{r}) \cdot \overline{E^{INC}}(\overline{r}) = \int_S \boldsymbol{f}(\overline{r}) \cdot (\overline{\nabla \Phi_A}(\overline{r}) + i\omega \overline{A_A}(\overline{r})) dS(\overline{r}). \qquad (2.21)$$

where $\Phi_A$ is the approximate[8] electric scalar potential, $\overline{A_A}$ is the approximate electric vector potential, and $\boldsymbol{f}(\overline{r})$ is a vector of all the testing functions evaluated[9] at $\overline{r}$:

$$\boldsymbol{f}(\overline{r}) = \begin{bmatrix} \vdots \\ \overline{f_m}^T(\overline{r}) \\ \vdots \end{bmatrix}. \qquad (2.22)$$

Using a single-point quadrature approximation scheme for the testing integral, we obtain

$$
\begin{aligned}
\boldsymbol{E}_m &= \sum_{T_{m+}, T_{m-}} \overline{f_m}(\overline{r_{\bullet m\pm}}) \cdot \overline{E^{INC}}(\overline{r_{\bullet m\pm}}) \\
&= \sum_{T_{m+}, T_{m-}} \int_S \nabla \cdot \overline{f_m}(\overline{r})|_{\overline{r}=\overline{r_{\bullet m\pm}}} \Phi_A(\overline{r_{\bullet m\pm}}) - i\omega \overline{f_m}(\overline{r_{\bullet m\pm}}) \cdot \overline{A_A}(\overline{r_{\bullet m\pm}}) dS
\end{aligned}
$$

---

[8]The "A" subscript indicates approximation of the unknown current densities by a weighted sum of basis functions.

[9]Only the three RWG testing function associated with the three edges of the panel, containing a selected surface point, will be non-zero at the selected point

$$
= \sum_{T_{m+},T_{m-}} \int_S \frac{\pm l_m}{2A_{m\pm}} \Phi_A(\overline{r_{\bullet m\pm}}) + i\omega \overline{f_m}(\overline{r_{\bullet m\pm}}) \cdot \overline{A_A}(\overline{r_{\bullet m\pm}}) dS \tag{2.23}
$$

$$
= \sum_{T_{m+},T_{m-}} (\pm l_m)\Phi_A(\overline{r_{\bullet m\pm}}) + i\omega \overline{f_m}(\overline{r_{\bullet m\pm}}) \cdot \overline{A_A}(\overline{r_{\bullet m\pm}}),
$$

where $\overline{r_{\bullet m\pm}}$ is the centroid ($\bullet$ signifies a panel centroid) of the $\pm$ panel associated with the mth edge, and, after substituting for $\Phi_A(\overline{r})$ and $\overline{A_A}(\overline{r})$,

$$
\boldsymbol{E}_m = \sum_{n=1}^{n_E} J_n \sum_{T_{m+},T_{m-}} \int_{S'} \frac{\mp l_m}{i\omega\epsilon} \nabla' \cdot \overline{f_n}(\overline{r'}) G(\overline{r_{\bullet m\pm}},\overline{r'}) + i\omega\mu \overline{f_m}(\overline{r_{\bullet m\pm}}) \cdot \overline{f_n}(\overline{r'}) G(\overline{r_{\bullet m\pm}},\overline{r'}) dS'
$$

$$
= \sum_{n=1}^{n_E} J_n \sum_{T_{m+},T_{m-}} \int_{S'} \left( \frac{(\mp l_m)(\mp l_n)}{i\omega\epsilon A_{n\pm}} \right) G(\overline{r_{\bullet m\pm}},\overline{r'}) - i\omega\mu \overline{f_m}(\overline{r_{\bullet m\pm}}) \cdot \overline{f_n}(\overline{r'}) G(\overline{r_{\bullet m\pm}},\overline{r'}) dS' \tag{2.24}
$$

Using a $n_Q$ point quadrature rule to perform the inner surface integration, one obtains the *mth* row of the discretized EFIE,

$$
\boldsymbol{E}_m = \langle \overline{f_m}, \overline{E^{INC}} \rangle = \sum_{n=1}^{n_E} J_n \sum_{j=1}^{n_Q} w_{Qj} \sum_{T_{m+},T_{m-}} \left[ \left( \frac{(\mp l_m)(\mp l_n)}{i\omega\epsilon A_{n\pm}} \right) G(\overline{r_{\bullet m\pm}},\overline{r_{Qj}}) \right.
$$

$$
\left. - i\omega\mu \overline{f_m}(\overline{r_{\bullet m\pm}}) \cdot \overline{f_n}(\overline{r_{Qj}}) G(\overline{r_{\bullet m\pm}},\overline{r_{Qj}}) \right] \tag{2.25}
$$

which relate the unknown $\boldsymbol{J}$ coefficients to the tested incident source field.

## 2.5.2 EM Scattering Model for a target

Equation 2.25 was generated from applying discretization procedures described earlier to the EFIE. If equation 2.25 is written in matrix form, the result is a frequency domain model:

$$
[s\mu \boldsymbol{A}(s) + \frac{\Phi(s)}{s\epsilon_0}]\boldsymbol{J} = \boldsymbol{E}(s)
$$

$$
\Rightarrow \boldsymbol{Z}(s)\boldsymbol{J} = [((s)^2 \boldsymbol{A}(s) + \Phi(s)]\boldsymbol{J} = s\epsilon_0 \boldsymbol{E}(s) \tag{2.26}
$$

$$
y = s\epsilon_0 [\boldsymbol{C}(s)]^T \boldsymbol{Z}(s)^{-1}[\boldsymbol{E}(s)]
$$

43

In Equation 2.26, $s$ is the Laplace frequency variable, $c_0$ is the speed of light, $i = \sqrt{-1}$ , $k$ is spatial frequency, $s = s/c_0$, $\boldsymbol{A}$ is a matrix that specifies contribution from the discretization of the IE term corresponding to the electric vector potential, branch resistances, $\boldsymbol{\Phi}$ is a matrix that specifies contribution from the discretization of the IE term corresponding to the gradient of the electric scalar potential, $\boldsymbol{J}$ are the current coefficients for the RWG basis functions approximating the current density, $\boldsymbol{E}$ is the contribution of the tested source incident field, and $y$ is the desired output scattered field at a selected observation point.

### 2.5.3  Impedance Model for SoB or SoP Interconnect

Maxwell's Laws can also be formulated into integral equations that relate mesh currents and voltages on SoB and SoP interconnect structures. In order to analyze the impedance of the interconnect structures, the FastPep tool employs a formulation based on a set of mixed volume and surface integral equations that enforce Maxwell's Laws on the surface and in the volume of the interconnect structures. FastPep has been modified to capture full-wave effects.

FastPep approximates currents flowing in the volume of the interconnect using constant filament basis functions, each of which approximates the current flow through the small cylindrical portion (filament) of the volume in which the basis function is supported (nonzero). The filament basis functions have constant nonzero value only in the filament to which they correspond. FastPep approximates currents and charges on the surface of the interconnect using constant valued surface panel basis functions. Figure 1-3 illustrates an interconnect structure that has been discretized with filaments and panels, but only the surface panels are visible. The basis functions have a constant value on the small patch (or triangular panel in our implementation) of the surface to which the basis function corresponds and is supported, having zero values at every other portion of the surface and volume. FastPep employs Galerkin procedures to discretize[10] the IEs, and so the testing functions are chosen to be the

---

[10]Although the constant valued basis functions are different from the RWG basis functions used to discretize the EFIE for EM scattering problems, the basis steps in discretization are virtually
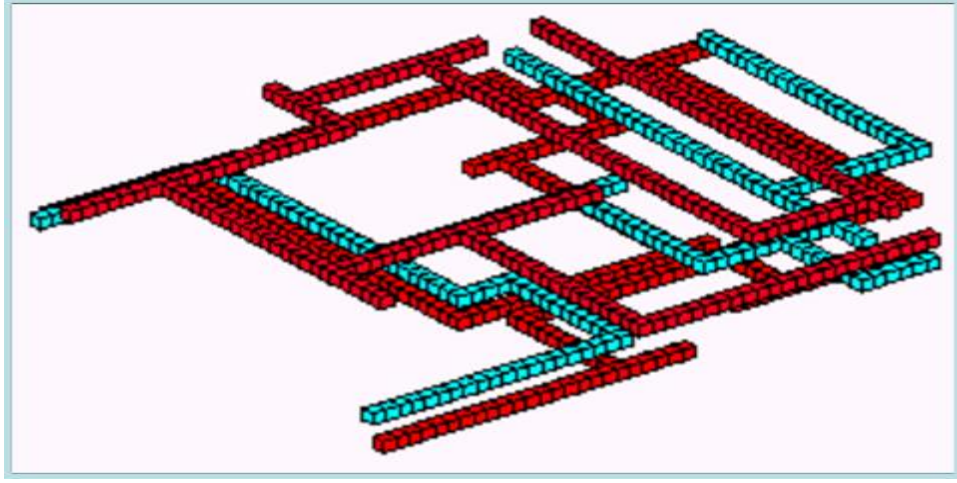
Figure 2-3: Interconnect: This figure is borrowed with permission from Michael Chou

same basis functions.

Following the steps outlined above, our modified version of FastPep generates a Partial Element Equivalent Circuit (PEEC) Model [20] of the system. Applying Kirchoff's current law (KCL) and Kirchoff's voltage law to each of the resulting loops that involve the filaments and/or panels, a mesh formulation for the original system can be derived which relates the mesh currents to the mesh voltage:

$$
\begin{aligned}
\boldsymbol{Z}(s) \ \boldsymbol{J} &= \boldsymbol{B} \\
y &= \boldsymbol{B}^T \boldsymbol{Z}(s)^{-1} \boldsymbol{B}
\end{aligned}
\tag{2.27}
$$

$$
\boldsymbol{Z}(s) = \boldsymbol{M}
\begin{bmatrix}
\boldsymbol{R} + s\boldsymbol{L}(s) & \boldsymbol{0} \\
\boldsymbol{0} & \frac{\boldsymbol{P}(s)}{s}
\end{bmatrix}
\boldsymbol{M}^T .
$$

In equation 2.28 each element of the matrix $\boldsymbol{P}(s)$ corresponds to the full-wave scalar potential interactions between a particular pair of surface panels on the interconnect, $s$ is the Laplace frequency variable, $\boldsymbol{M}$ computes loop voltages from branch, $\boldsymbol{M}^T$

---

identical to those described earlier in sections 2.5 and 2.5.1.

computes branch currents from loop currents, $R$ specifies branch[11] resistances, $L(s)$ specifies branch inductances, $P(s)$ relates the branch voltages to branch charge, $J$ are the mesh loop currents, $B$ is the source voltage, which is zero everywhere except at the specified source panel (in our implementation), and $y$ is the desired output current at that same panel.

## 2.6 Sparsification techniques for rapid system solves

### 2.6.1 Motivation

The linear systems (2.26) and (2.28) comprise of dense matrices $A(s)$ and $\Phi(s)$ that approximate the frequency domain behavior of the original system. For complicated EM structures, the dimension [12], $n_E$, of a discretized model that would be required to accurately approximate the actual structure behavior frequently reach $O(10^5)$ and even $O(10^6)$. Thus, if $n_E > 10^5$ or $10^6$, and the iterative solver costs $O(n_E^2)$ operations, then the cost of solving for the unknown current density of the system at just a single frequency point would be greater than $O(10^{10})$ or even $O(10^{12})$ operations! Thus, the scattering or impedance model's computational complexity would preclude rapid simulation using traditional iterative solution methods due to the infeasible operation counts.

The $n_E$ linear equations with $n_E$ unknowns representing the model 2.26 or the model 2.28 can be solved using iterative techniques, which require $O(n_E^2)$ multiplications and additions. These iterative techniques solve the system by repeated matrix-vector products with the system matrix. Every basis function interacts with every other basis function, so the matrix vector multiply must reflect every such operation. The interactions which must be computed for just one edge are illustrated in Figure 2-4 for an edge on panel 1.

---

[11] Since Fast-Pep is a hybrid mesh formulation, involving filaments, entries of $Z(s)$, $R$, and $L(s)$ do not correspond to pairs of panels.

[12] $n_E$ corresponds to the number of elements in the unknown vector of basis-function coefficients (current density coefficients for the edges or mesh current coefficients for the filaments and panels) for the discretized models represented by equations (2.26) or (2.28)
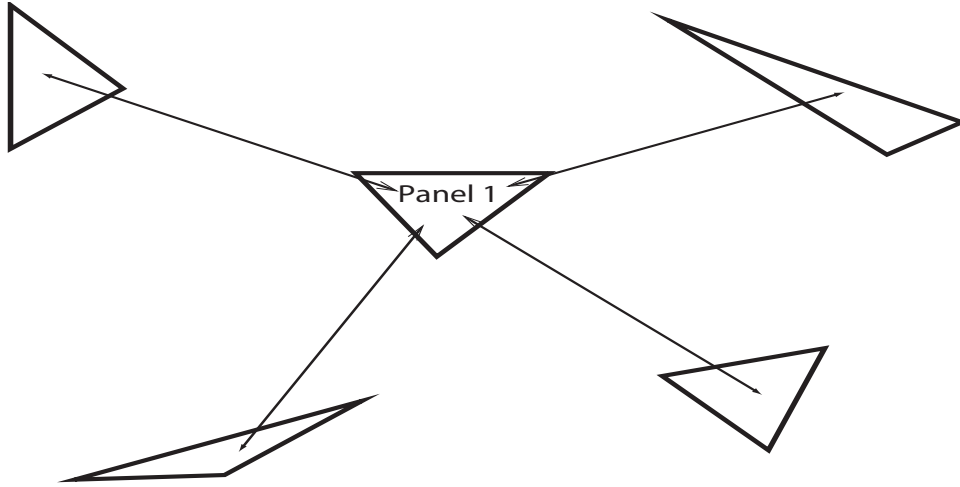
Figure 2-4: The arrows in this diagram of a five panel system represent the interactions associated with just one of the panels. Each of the 5 panels has a similar diagram of interactions. The matrix-vector product in equation 2.26 computes scattered electric field due to induced current sources. This computation requires $O(n_E^2)$ operations, because each edge current basis function interacts with every other edge current basis function. Thus, since each edge basis function is only non-zero on that edge's associated panels, solving the matrix vector product involves computing interactions (numerical quadratures) between each possible pair of panels.

To permit simulation, Electromagnetic scattering analysis solvers and Impedance extraction tools for Interconnect analysis, dramatically accelerate solution of the discretized linear system by employing "sparsification" algorithms in unison with iterative methods [40]. Since these sparsification algorithms require significantly less than $O(n_E^2)$ operations to compute approximate matrix vector products, the result of using iterative methods based on these sparsification algorithms yields very fast solvers (matrix vector products for many problems require roughly $O(n_E)$ operations to compute)!

## 2.6.2  Basics of Sparsification

Since iterative methods solve a system of equations, $\boldsymbol{Z}(s)\boldsymbol{J} = \boldsymbol{E}(s)$, by computing repeated matrix vector products involving the system matrix, $\boldsymbol{Z}(s)$, these methods do not explicitly require the system matrix itself, and require only the result of multiplying $\boldsymbol{Z}(s)$ with a vector. Thus, if one could rapidly compute an approximation

to the desired matrix vector products, the system of equations $\boldsymbol{Z}(s)\boldsymbol{J} = \boldsymbol{E}(s)$ could be rapidly solved, but $\boldsymbol{Z}(s)$ would never actually need to be generated. For certain kinds of problems, this basic idea can be utilized to accelerate computations, by applying one of several alternative "sparsification" techniques, which compute sparse nearby interactions directly, but approximate the far-away interactions in order to reduce operations. These methods can reduce the number of operations required for a matrix vector product from $O(n_E^2)$ to almost $O(n_E)$.

Sparsification methods rely on the same key ideas to accelerate matrix vector products used to solve the system $\boldsymbol{Z}\boldsymbol{J} = \boldsymbol{b}$. The system matrix is decomposed into "nearby" and "far-away" terms. The entries are classified by the interaction distances between the panels (or edges) to which those entries of the matrix correspond. In this manner the original matrix is decomposed into two matrices:

$$\boldsymbol{Z}\boldsymbol{J} = [\boldsymbol{Z_N} + \boldsymbol{Z_F}]\boldsymbol{J} = \boldsymbol{b}. \tag{2.28}$$

The matrix representing the nearby interactions, $\boldsymbol{Z_N}$ is very sparse such that $\boldsymbol{Z_N}\boldsymbol{J}$ requires $O(n_E)$ operations. Under closer examination, the matrix vector product $\boldsymbol{Z_F}\boldsymbol{J}$ has the form:

$$\sum_{n=0}^{n_E} \overbrace{G(\|\overline{x_m} - \overline{x_n}\|)}^{\boldsymbol{Z}_{mn}} J(\overline{x_n}) = b(\overline{x_m}), \tag{2.29}$$

which is a discrete convolution. With minor variations, the key idea behind the various sparsification techniques is to approximate the kernel $G(\|\overline{x_m}-\overline{x_n}\|)$ for distant interactions with a degenerate kernel, for example: $G(\|\overline{x_m} - \overline{x_n}\|) \approx G_1(\overline{x_m})G_2(\overline{x_n})$, resulting in a separable summation:

$$
\begin{aligned}
\sum_{n=0}^{n_E} \boldsymbol{Z}_{mn}\boldsymbol{J}_n &= \boldsymbol{b}_m \\
\sum_{n=0}^{n_E} \overbrace{G_1(\overline{x_m})G_2(\overline{x_n})}^{G(\|\overline{x_m}-\overline{x_n}\|)\approx} J(\overline{x_n}) &= b(\overline{x_m}) \\
\Downarrow &
\end{aligned}
\tag{2.30}
$$

$$G_1(\overline{x_m}) \sum_{n=0}^{n_E} G_2(\overline{x_n}) J(\overline{x_n}) \;\; = \;\; b(\overline{x_m})$$

$$(2.31)$$

which essentially diagonalizes the terms corresponding to the matrix $\boldsymbol{Z_F}$ and requires $O(n_E)$ operations to compute, such that the overall approximation to $\boldsymbol{ZJ} = \boldsymbol{b}$ is $O(n_E)$ instead of $O(n_E^2)$!

For example, the Precorrected Fast Fourier Transform (PFFT) algorithm, which will be described in detail later, essentially transforms the convolution into a "degenerate kernel" approximation to the original for the computation of "far away" interactions. Using the Discrete Fourier Transform (DFT), the PFFT separates the m-index terms from the n-index terms so that the Green's function evaluation is just over the $\overline{x_n}$, :

$$\mathcal{F}^{-1}\left[(\mathcal{F}\boldsymbol{G})(\mathcal{F}\boldsymbol{J})\right] = \sum_{p=0}^{n_G-1} \left[ \overbrace{\sum_{n=0}^{n_G-1} G(\overline{x_n}) e^{\frac{i2\pi np}{n_G}} \sum_{n=0}^{n_G-1} J(\overline{x_n}) e^{\frac{i2\pi np}{n_G}}}^{\text{n-indexed term}} \right] \overbrace{e^{\frac{i2\pi mp}{n_G}}}^{\text{m-indexed term}} \quad , \;\; (2.32)$$

but the benefit of this DFT-based transformation seems questionable because the result is two functions that are both $n_G$ summations of $n_G$ terms ($n_G \approx n_E$), as is the outer inverse DFT. The resulting summations would require a greater number of operations than the original convolution computation. However, the advantage is clearer when one considers that the Fast Fourier Transform (FFT) algorithm performs each DFT in $n_G \log(n_G)$ operations and the element-wise multiplication of the two $n_G$-length vectors $(\mathcal{F}\boldsymbol{G})(\mathcal{F}\boldsymbol{J})$ requires just $O(n_G)$ operations, such that the result of the PFFT sparsification is a matrix vector product which requires only $O(n_E \log n_E)$ operations, a huge savings relative to $O(n_E^2)$ required for the original convolution!

### 2.6.3 Choosing between two Sparsification Methods

For electromagnetic computations the Fast Multipole (FMM) [8], Multilevel Fast Multipole method (MFMM) [43, 4] and Precorrected Fast Fourier Transform (PFFT)

[36, 37, 46] are popular methods for accelerating the matrix-vector product from discretized integral equations with Helmholtz or Laplace kernels. FMM reduces computations to $O(n_E^{1.5})$, MFMM (improvement on FMM) can reduce the computation to $O(n_E \log(n_E))$ operations for sparse scatterers or $O(n_E)$ operations for dense scatterers, and PFFT can reduce the computation to $O(n_E \log(n_E))$ operations. PFFT's performance is somewhat dependent on geometrical considerations because it performs less well on very inhomogeneous geometries with higher ratios of volume to surface grid points[13]. For most problems, the PFFT algorithm is faster because of a high constant factor associated with MFMM cost[14]. For this research, the PFFT algorithm will be used because the PFFT acceleration method is essentially independent of the IE kernel or Green's function [15], making the PFFT method more amenable to modifications required to implement model order reduction. The fundamentals of the Precorrected Fast Fourier Transform (PFFT) [36] algorithm, are reviewed next.

## 2.6.4 Basics of the Precorrected Fast Fourier Transform Algorithm

The EFIE ( 2.16) is a Fredholm IE of first kind with a translationally invariant kernel. It is the sum of two terms, one corresponding to the vector potential and the other corresponding to the gradient of the scalar potential. Each of the terms in the IE has the form of a convolution between the Helmholtz Green's function and another function, which is the current density for the vector potential term and the gradient of the divergence of the current density for the scalar potential term. For example, the vector potential term in the IE is:

$$\overline{A}(\overline{r}) = \oint_S \overline{J_S}(\overline{r}')G(\|\overline{r} - \overline{r}'\|)dS(\overline{r}'), \tag{2.33}$$

---

[13]grid points in a cell through which a surface passes are surface grid points while volume grid points are grid points in cells which contain no surfaces

[14]the crossover point where $\log(n_E)$ is greater than the MFMM factor requires a panel count, $n_E$, not usually approached in typical problems

[15]as opposed to the FMM and MFMM algorithms which are highly dependent on the specific Green's function being used

which is a convolution.

Thus, the discretized EFIE 2.26, $\boldsymbol{Z}(s)\boldsymbol{J} = \boldsymbol{E}(s)$, has the form of a discrete convolution. The discrete convolutions are quite expensive since each involves computing several operations for each observation and source point pair. Convolving two functions at $n_E$ discrete points requires $O(n_E^2)$ operations. However, Fourier Transform theory suggests an idea to improve the situation: if the interacting observation and source points were regularly spaced points, then the Fast Fourier Transform algorithm could compute the discrete convolution in $O(n_E \log(n_E))$ operations[16]. Therefore, in order to take advantage of the efficient FFT algorithm to compute the otherwise time-consuming convolution, the PFFT employs a grid approximation to the original current density coefficients. The grid currents are computed to approximately induce the same far field effects as the original surface current densities.

Thus, the PFFT algorithm uses a grid approximation of the original current density coefficients in order to take advantage of the rapid FFT algorithm. In the first step of this algorithm, the current densities are projected to grid point currents on a regularly spaced grid. The projection operator use polynomial interpolation functions to compute grid point current values that would be *equivalent*[17] to the original panel current density coefficients *with respect to computation of an electric field* at preselected *far-away* observation points.

The observations from the previous paragraphs motivate the main ideas behind the Precorrected Fast Fourier Transform algorithm [36]. Figure 2-5 illustrates the basic steps of the PFFT algorithm when applied to compute the convolution described by the integral equation 2.26 for a 2-D example. First, panels charge densities are projected to the regularly spaced gridpoints of the grid cell containing the panel. Then the grid point charges are convolved with the Green's function via the FFT and IFFT in $O(n_G \log(n_G))$ operations to compute the potential at all grid points. Finally, the grid point potentials are interpolated back to panel quadrature points.

---

[16] Convolution on a regularly spaced grid is equivalent to computing the inverse Discrete Fourier Transform (DFT) of the product of the individual DFT's of the functions to be convolved and this task can be computed very efficiently in $O(n_G \log(n_G))$ operations using the Fast Fourier Transform (FFT), where $n_G$ is the number of grid points, and $O(n_G) = O(n_E)$ for most problems.

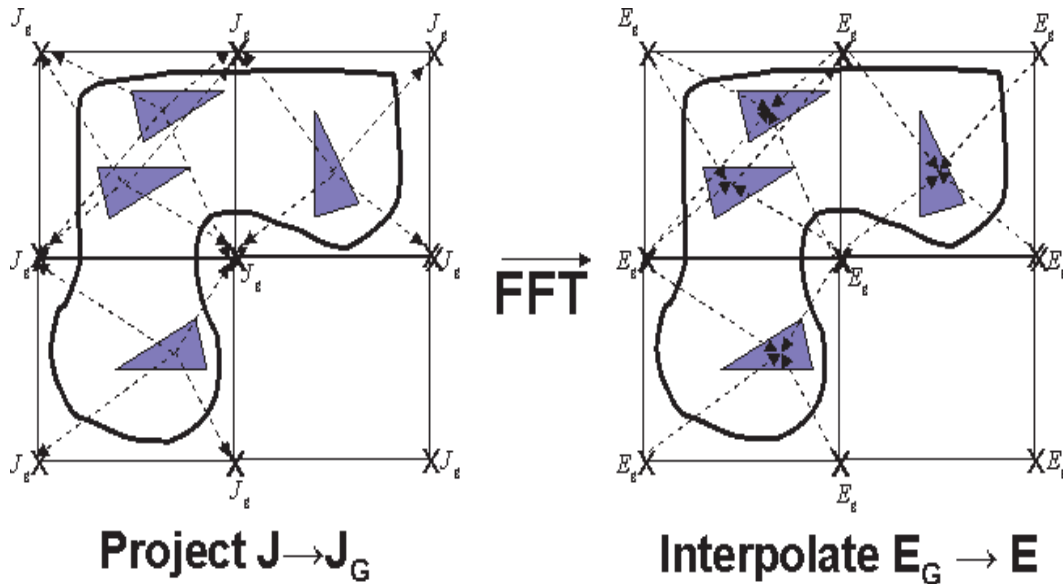[17] within pre-selected accuracy threshold

Figure 2-5: 2-D illustration of basic steps of Precorrected Fast Fourier Transform Algorithm: project panel quantities to regularly spaced grid points , compute incident Electric field at grid points via FFT, interpolate grid fields to compute approximate panel incident Electric fields.

In the PFFT algorithm, there is an additional step required to compute the matrix-vector product accurately: Grid point source values, computed by projecting panel source values, can represent the original source functions accurately for "far away" points in the convolution, but the interactions between nearby points in the convolution need to be solved exactly. Thus, the portions of the tested electric field, which is interpolated from the grid and represents contributions from "nearby" source panels, is subtracted from each panel's tested-electric field total, and the exact contribution due to interaction of the nearby panels is computed directly. The step of removing the inaccurate grid "nearby" contribution and replacing it with directly computed results is called "precorrection".

Since this presentation aims to provide just an overview of the PFFT that is sufficient to understand the research contributions of this dissertation, a number of implementation details have been omitted for the purpose of clarity and brevity. The details of the PFFT algorithm, including constructing the grid, partitioning grid-points into cells, assigning panels to cells, and much more can be explored by further

$$\cdot \ \overset{\bar{r}}{E}(\overset{\bar{}}{r}) = G\ (\overset{\bar{}}{r},\overset{\bar{}}{r'})\ J(\overset{\bar{}}{r'})$$
$$= G\big(\bar{r}_{G1},\bar{r}\big)J_{G1} + G\big(\bar{r}_{G2},\bar{r}\big)J_{G2}$$
$$+ G\big(\bar{r}_{G3},\bar{r}\big)J_{G3} + G\big(\bar{r}_{G4},\bar{r}\big)J_{G4}$$
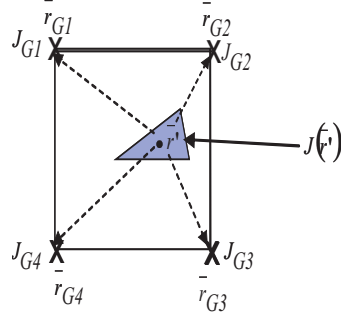


Figure 2-6: Projection involves calculating the current density at grid points, $\overline{r_{G1}}, \ldots, \overline{r_{G4}}$, of a cell that would induce the same electric field, at a distant arbitrary point, as would be induced by the current densities at points $\bar{r}'$ of the panels in that cell.

reading in [36, 37, 46]. Throughout the following sections, the details of numerical integration and how the PFFT is incorporated with discretization are omitted. Note that the following sections show how PFFT can accelerate a discrete convolution between the Green's function and the current density coefficients, suppressing the weights associated with each element of the system matrix that result from computing the two integrations involving the Green's function (which PFFT approximates with the projection and interpolation polynomials) and the basis and testing functions.

### 2.6.5 The PFFT Projection operation

The discretized EFIE described in equation 2.25 and equation 2.26 requires current density values and evaluation of the Green's functions at the panel quadrature points. In order to take advantage of the FFT algorithm, it is necessary to project source quantities (current density) from panels to evenly spaced grid points, as illustrated in figure 2-6. This subsection outlines the steps to construct a operator based on polynomials to accomplish this projection, as demonstrated in [46].

The function $\frac{e^{-ik|x|}}{|x|}$ is smooth away from the origin and has continuous derivatives

up to any order away from the origin. Therefore, it is reasonable to approximate the Helmholtz Green's function $G_H(\overline{r}, \overline{r}') = \frac{e^{-ik\|\overline{r}-\overline{r}'\|}}{\|\overline{r}-\overline{r}'\|}$ as a linear combination of polynomials, $p_m(\overline{r}', \overline{r})$ for far-away interactions:

$$G_H(\overline{r}, \overline{r}') \approx \sum_{m=0}^{n_I} \varphi_m(\overline{r}) p_m(\overline{r}', \overline{r}) = \boldsymbol{\varphi}(\overline{r})^T \boldsymbol{p}(\overline{r}', \overline{r}), \qquad (2.34)$$

where $n_I$ is the order of the polynomial approximation and $\varphi_m(\overline{r})$ is the weighting coefficient corresponding to the $m$-th polynomial.

By hypothesizing an electric field at an arbitrary distant observation point, $\overline{r}$, the polynomial approximation can be utilized to facilitate projection of current densities on panels to "equivalent" currents at grid points. Although the electric field, $E$, is a sum of two terms[18], for simplicity of notation , the following section considers the system matrix as a set of Green's function evaluations and ignores the two weighting factors at each element that results from integration and discretization of the two terms of the EFIE to demonstrate projection for the grid current coefficients, without loss of generality . Thus, at the observation point $\overline{r}$ the $\alpha$-th component of electric field, $E_\alpha(\overline{r})$, induced by the $\alpha$-th component of a source current density, $J_\alpha(\overline{r}')$, at point $\overline{r}'$ is:

$$E_\alpha(\overline{r}) = G_H(\overline{r}, \overline{r}') J_\alpha(\overline{r}') \approx \boldsymbol{\varphi}(\overline{r})^T \boldsymbol{p}(\overline{r}', \overline{r}). \qquad (2.35)$$

To "unclutter" notation, from this point on, during this discussion, the index $\alpha$ of the electric field $E$ and current density $J$ will be suppressed and it will be assumed the variables refer to a single component of those quantities. Figure 2-7 illustrates equation 2.35 for a single panel containing a source point $\overline{r}'$ within a cell composed of four grid points, $\overline{r_{G1}}, \ldots, \overline{r_{G4}}$.

For $n_C$ panels contained in a "cell" of grid points the electric field (component) at an observation point far-away $\overline{r}$ is:

---

[18]EFIE 2.26 has two terms: first corresponds to vector potential and second corresponds to gradient of the scalar potential
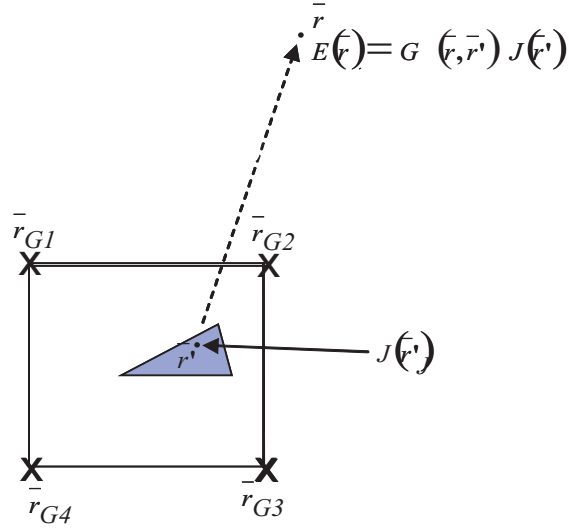
Figure 2-7: This figure illustrates the electric field at $\overline{r}$ that is induced by the current density at point $\overline{r}'$ of panel within a cell defined by the grid points, $\overline{r_{G1}}, \ldots, \overline{r_{G4}}$.

$$E(\overline{r}) = [\boldsymbol{P_C}\boldsymbol{\varphi}(\overline{r})]^T \boldsymbol{J}, \tag{2.36}$$

where

$$\boldsymbol{P_C} \approx \begin{bmatrix} \int_{S'} p_1(\overline{r}',\overline{r})\overline{f_1}(\overline{r}')dS' & \int_{S'} p_2(\overline{r}',\overline{r})\overline{f_1}(\overline{r}')dS' & \cdots & \int_{S'} p_{n_I}(\overline{r}',\overline{r})\overline{f_1}(\overline{r}')dS' \\ \int_{S'} p_1(\overline{r}',\overline{r})\overline{f_2}(\overline{r}')dS' & \int_{S'} p_2(\overline{r}',\overline{r})\overline{f_2}(\overline{r}')dS' & \cdots & \int_{S'} p_{n_I}(\overline{r}',\overline{r})\overline{f_2}(\overline{r}')dS' \\ \vdots & \vdots & \vdots & \vdots \\ \int_{S'} p_1(\overline{r}',\overline{r})\overline{f_{n_C}}(\overline{r}')dS' & \int_{S'} p_2(\overline{r}',\overline{r})\overline{f_{n_C}}(\overline{r}')dS' & \cdots & \int_{S'} p_{n_I}(\overline{r}',\overline{r})\overline{f_{n_C}}(\overline{r}')dS' \end{bmatrix},$$

in which the integrals are the same inner integral in equation 2.24 and are computed by quadrature (as shown in equation 2.25) and the Green's function in the integrand of (2.24) is approximated by the weighted sum of the projection polynomials $p_m$.

If the same electric field were induced at $\overline{r}$ by a set of $n_G$ grid points, comprising the cell C, one could write:

$$E_C(\overline{r}) = \sum_{l=1}^{n_G} G_H(\overline{r},\overline{r_{Gl}})J(\overline{r_{Gl}}) \approx \sum_{l=1}^{n_G} \boldsymbol{\varphi}(\overline{r})^T \boldsymbol{p}(\overline{r_{Gl}},\overline{r})J(\overline{r_{Gl}}) = [\boldsymbol{P_G}\boldsymbol{\varphi}(\overline{r})]^T \boldsymbol{J_G}, \tag{2.37}$$
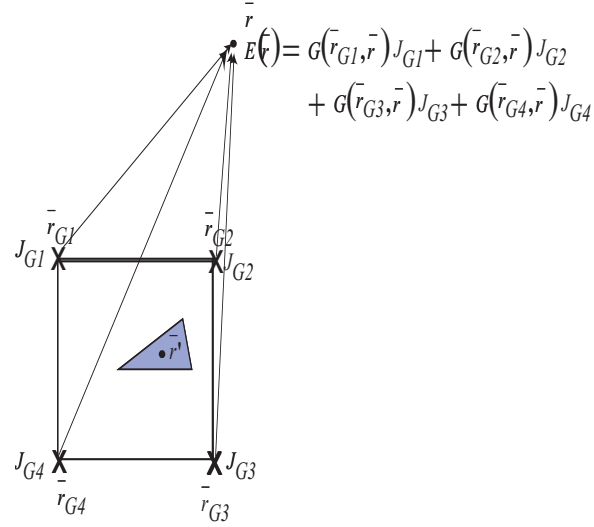
Figure 2-8: This figure illustrates the electric field at $\overline{r}$ that is induced by the grid currents at grid points, $\overline{r_{G1}}, \ldots, \overline{r_{G4}}$, of the cell (containing the panel with current densities that are to be projected).

where

$$
\boldsymbol{P_G} = \begin{bmatrix} p_1(\overline{r_{G1}}) & p_2(\overline{r_{G1}}) & \cdots & p_{n_I}(\overline{r_{G1}}) \\ p_1(\overline{r_{G2}}) & p_2(\overline{r_{G2}}) & \cdots & p_{n_I}(\overline{r_{G2}}) \\ \vdots & \vdots & \vdots & \vdots \\ p_1(\overline{r_{Gn_G}}) & p_2(\overline{r_{Gn_G}}) & \cdots & p_{n_I}(\overline{r_{Gn_G}}) \end{bmatrix},
$$

and the shared $\overline{r}$ dependency has been suppressed in the polynomials, $p_m(\overline{r_{Gm}}', \overline{r})$, to reduce notation. Equation 2.37 is illustrated in figure 2-8

Therefore, the two expressions for the electric field $E_C(\overline{r})$ that is induced at the distant point $\overline{r}$ by the currents contained in the cell, can be equated, and a expression for the grid current density $\boldsymbol{J_G}$ "projected" from the panel current density $\boldsymbol{J_C}$ in the cell can be derived:

$$
[\boldsymbol{P_G}\varphi(\overline{r})]^T \boldsymbol{J_G} = [\boldsymbol{P}(\overline{r}')\varphi(\overline{r})]^T \boldsymbol{J_C} \tag{2.38}
$$
$$
\varphi(\overline{r})^T \boldsymbol{P_G}^T \boldsymbol{J_G} = \varphi(\overline{r})^T \boldsymbol{P}(\overline{r}')^T \boldsymbol{J_C}
$$
$$
\Rightarrow \boldsymbol{J_G} = \underbrace{\boldsymbol{P_G}^{-T} \boldsymbol{P}(\overline{r}')^T}_{\boldsymbol{W}} \boldsymbol{J_C},
$$

which supplies the formula for a projection operator $\boldsymbol{W}$ that maps panel current densities in a cell to *equivalent*[19] grid point currents for the grid points associated with that cell. The projection operation is carried out for each cell, and thus all the panels and gridpoints, in the grid. Note that $\boldsymbol{P_G}$ can be the same for every cell, if it is computed using local coordinates, but to allow this, $\boldsymbol{p}(\overline{r_{Gm}}, \overline{r})$ must be converted to local coordinates.

### 2.6.6 Discrete Convolution via FFT operations for the EFIE

Once current density and required derivatives of the current density have been projected from panel quantities to grid quantities, the grid electric field components are computed by convolving the Helmholtz Green's function with the grid current quantities. Although the electric field, $E$, is a sum of two term, for simplicity of notation , the following section considers the system matrix as a set of Green's function evaluations and ignores the two weighting factors at each element that results from integration and discretization of the two terms of the EFIE to demonstrate FFT-based convolution between the grid current approximation to the panel current coefficient and the Green's function (evaluated at grid points), without loss of generality. Thus, the discrete convolution has the form:

$$\boldsymbol{E_G} = \boldsymbol{G_G}\boldsymbol{J_G}, \tag{2.39}$$

where $\boldsymbol{G_G}$ is the Green's function relating current density to vector potential via 3-D convolution with discrete grid point values,

$$\boldsymbol{G_G} = \begin{bmatrix} G(\overline{r_{G1}} - \overline{r_{G1}}) & G(\overline{r_{G1}} - \overline{r_{G2}}) & \cdots & G(\overline{r_{G1}} - \overline{r_{Gn_G}}) \\ G(\overline{r_{G2}} - \overline{r_{G1}}) & G(\overline{r_{G2}} - \overline{r_{G2}}) & \cdots & G(\overline{r_{G2}} - \overline{r_{Gn_G}}) \\ \vdots & \vdots & \ddots & \vdots \\ G(\overline{r_{Gn_G}} - \overline{r_{G1}}) & G(\overline{r_{Gn_G}} - \overline{r_{G2}}) & \cdots & G(\overline{r_{G1}} - \overline{r_{Gn_G}}). \end{bmatrix} \tag{2.40}$$

---

[19]with respect to far-away interactions

57

Because the points $\overline{r_{Gl}}$ are all on a regular 3-dimensional grid, it is clear that $G_G$ is just a 3-dimensional convolution of discrete functions evaluated at gridpoints, equally spaced within each dimension. Thus, from , we obtain

$$\boldsymbol{E_G}[\alpha, \beta, \gamma] = \sum_{l,m,n=1}^{n_{Gx},n_{Gy},n_{Gz}} \boldsymbol{g_G}[\alpha - l, \beta - m, \gamma - n]\boldsymbol{J_G}[l, m, n], \qquad (2.41)$$

where $\boldsymbol{g_G}$ is a function of discrete (integer) arguments, formed from $\boldsymbol{G_G}$ by dividing the argument variable in each dimension by the grid spacing to obtain the integer values ($x = \alpha h, y = \beta h, z = \gamma h$), where $h$ is the grid spacing). Similarly, the current density is transformed to a function of discrete arguments as well. By applying the Discrete Fourier Transform (DFT, $\mathcal{F}$) in each of the three dimensions, we obtain

$$\tilde{\boldsymbol{E_G}}[\varsigma, \tau, \nu] = \tilde{\boldsymbol{g_G}}[\varsigma, \tau, \nu]\tilde{\boldsymbol{J_G}}[\varsigma, \tau, \nu], \qquad (2.42)$$

for $\varsigma = 1, \ldots, n_{Gx}$, $\tau = 1, \ldots, n_{Gy}$, and $\nu = 1, \ldots, n_{Gz}$, which is a element by element multiplication of two arrays with $n_G$ elements, rather than the $O(N_G^2)$ operations required for the original convolution.

The inverse Fast Fourier Transform (IFFT) operation produces the original desired result for 2.39, replacing the convolution with two FFTs ($\mathcal{F}$) and one IFFT ($\mathcal{F}^{-1}$) .

$$\boldsymbol{E_G}[l, m, n] = \mathcal{F}^{-1}(\tilde{\boldsymbol{g_G}}[\varsigma, \tau, \nu]\tilde{\boldsymbol{J_G}}[\varsigma, \tau, \nu]), \qquad (2.43)$$

for a total cost of $O(n_G + 3n_G \log(n_G))$ , still significantly less (for large $n_G$) than $O(n_G^2)$, required to perform convolution[20].

### 2.6.7 The PFFT Interpolation operation

In order to take advantage of the FFT algorithm, it is necessary to interpolate induced quantities (electric field) from the evenly spaced grid points back to the panels, as illustrated in figure 2-9. This subsection outlines the steps to construct a operator based on polynomials to accomplish this interpolation, as demonstrated in [46]. As

---

[20]Note that in equation 2.43, the 3-dimensional grid is easily "re-indexed" or reshaped to form the original 1-dimensional vector of $n_G$ elements.
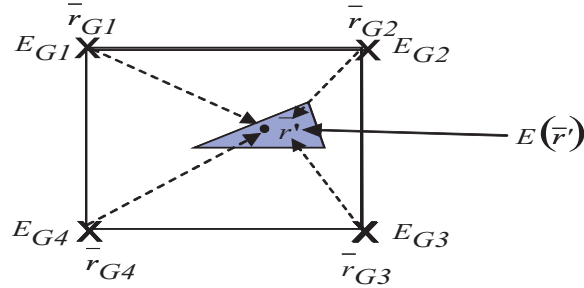
Figure 2-9: Interpolation involves calculating an electric field at the panels in a cell that is approximately equivalent to the computed electric field at the grid points, $\overline{r_{G1}}, \ldots, \overline{r_{G4}}$, of the cell in the sense that each of these electric fields would be induced by the same distant source charge located at an arbitrary point $\overline{r}$.

before, for simplicity of notation , the following section considers the system matrix as a set of Green's function evaluations and ignores the two weighting factors at each element that results from integration and discretization of the two terms of the EFIE to demonstrate interpolation from the grid electric field approximation to the induced fields on the panel, without loss of generality .

Using the same approximation 2.34 to the Helmholtz Green's function, a formula can be derived for the interpolation operator. At an observation point $\overline{r}$ the electric field, $E(\overline{r})$, induced by the source current density, $J(\overline{r'})$, at some arbitrary source point $\overline{r'}$ is:

$$E(\overline{r'}) = G_H(\overline{r'}, \overline{r})J(\overline{r}) \approx \boldsymbol{\varphi}(\overline{r})^T \boldsymbol{p}(\overline{r'}, \overline{r})J(\overline{r}). \tag{2.44}$$

Equation 2.44 is illustrated in figure 2-10 for a point $\overline{r'}$ on a single panel in a cell defined by four grid points, $\overline{r_{G1}}, \ldots, \overline{r_{G4}}$.

If there are multiple panels and multiple evaluation (quadrature) points on each
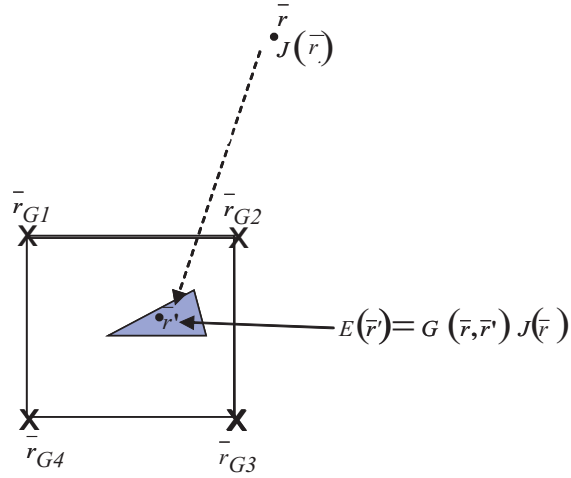
59

Figure 2-10: This figure illustrates the electric field at $\overline{r}$ that is induced by the current density of panel within a cell defined by the grid points, $\overline{r_{G1}}, \ldots, \overline{r_{G4}}$.

of the panels in a cell C, equation 2.44 can be extended to:

$$
\boldsymbol{E_C} = \begin{bmatrix} G_H(\overline{r}, \overline{r_{C1}}) \\ G_H(\overline{r}, \overline{r_{C2}}) \\ \vdots \\ G_H(\overline{r}, \overline{r_{Cn_C}}) \end{bmatrix} J(\overline{r}) \approx \boldsymbol{P_C}\varphi(\overline{r})J(\overline{r}), \tag{2.45}
$$

The key step is to deriving the interpolation operator is to realize that the Green's function is symmetric, and therefore, the polynomial coefficients and polynomials themselves can be "reused" for interpolation as well as projection.

As illustrated in figure 2-11 the electric field induced at the grid points due to the same current at an arbitrary observation point, $\overline{r}$ can be written

$$
\boldsymbol{E_G} = \begin{bmatrix} G_H(\overline{r}, \overline{r_{G1}}) \\ G_H(\overline{r}, \overline{r_{G2}}) \\ \vdots \\ G_H(\overline{r}, \overline{r_{Gn_G}}) \end{bmatrix} J(\overline{r}) \approx \boldsymbol{P_G}\varphi(\overline{r})J(\overline{r}), \tag{2.46}
$$

and the cell panel electric fields $\boldsymbol{E_C}$ can be "interpolated" from the grid electric fields
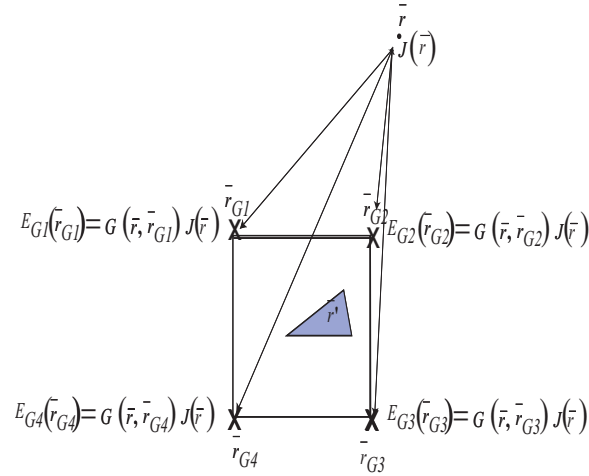
Figure 2-11: This figure illustrates the electric field at the grid points, $\overline{r_{G1}}, \ldots, \overline{r_{G4}}$ defining a cell C, that is induced by the current density at a distant arbitrary point $\overline{r}$.

$\boldsymbol{E_G}$ by eliminating the common term $\varphi(\overline{\boldsymbol{r}})J(\overline{r})$ in equations 2.45 and 2.46:

$$\boldsymbol{E_C} = \underbrace{\boldsymbol{P_C P_G}^{-1}}_{\boldsymbol{W}^T} \boldsymbol{E_G}, \tag{2.47}$$

where $\boldsymbol{W}^T$, the interpolation operator that accomplishes the desired feat illustrated by figure 2-9, is just the transpose of the projection operator $\boldsymbol{W}$.

## 2.6.8 The PFFT Precorrection step

The goal of this FFT-based method is to accelerate the matrix-vector product required for iterative solution of the discretized EFIE scattering system. While much more efficient to compute (rather than convolution), this "FFT-grid" approximation to the original discretized system (equation 2.26) has a serious deficiency. The contribution of nearby gridpoints, including gridpoints in that cell and neighboring cells, is very inaccurate due to the singularity of the Green's function. Furthermore, this nearby contribution is also much larger than the more accurate contribution of all the far-away grid points. Thus, the "FFT-grid" algorithm, described up to this point, would

61

seem to perform the worst on the most important computations. As a result, the final step of the PFFT algorithm is to "precorrect" the result for nearby panels. The grid contribution from all edge currents in nearby cells is removed for each edge result, and the interaction of all edges is computed "exactly" by equation 2.25 for each cell and its adjacent eight neighboring cells. The nearby "grid contribution" to the tested scattered field is

$$\langle \overline{E}(\overline{r}), \overline{f_o}(\overline{r}) \rangle \approx \boldsymbol{W}_{oc}^T \boldsymbol{G_{Gc}} \boldsymbol{W}_{sc} \boldsymbol{J}, \tag{2.48}$$

where $\boldsymbol{J}$ is the coefficient of the source current basis function (in cell $c$), $\overline{f_o}$ is the RWG basis function associated with observation edge $o$ (in cell $c$), $\boldsymbol{W}_{oc}$ is the interpolation from the cell $c$ to observation edge $o$, $\boldsymbol{W}_{sc}$ is the projection ref operator from edge $s$ to cell $c$, and $\boldsymbol{G_{Gc}}$ is the convolution operator between grid points in cell $c$.

Basically, equation 2.48 represents the (poorly approximated) FFT-grid contribution of the nearby source s to the scattered field at nearby observation edge $o$. This quantity can be computed for the interactions between each source edge $s$ in cell $c$ and its adjacent eight cells and each observation edge $o$ in cell $c$. Performing this step for all cells will account for all nearby interaction contributions to the scattered field and we can construct a vector of these inaccurate grid contributions, using the matrix[21] $\boldsymbol{N_G}$, which is subtracted from the results in equation 2.48, leaving only the more accurate contributions of grid-approximated far-away source edges. Note that for just the nearby interactions, convolution may be preferred to compute equation 2.48 instead of three FFTs if the number of points is small enough to save operations.

Finally, the contributions of nearby interactions are accounted for by the matrix[22] $\boldsymbol{N_{EX}}$ and these contributions are added back into equation 2.48, giving us a far more accurate resulting equation for computing the scattered field due to the induced source currents,

---

[21]The symbol $\boldsymbol{N}$ is chosen to signify that the matrix corresponds to "nearby" interactions, and the $G$ subscript denotes "grid" quantities

[22]The symbol $\boldsymbol{N}$ is chosen to signify that the matrix corresponds to "nearby" interactions, and the $EX$ subscript denotes quantities that are computed "exactly" or directly from the corresponding entries in the appropriate matrix in the EFIE (equation 2.25)

$$\langle \overline{E}(\overline{r}), \begin{bmatrix} \overline{f_1}(\overline{r}) \\ \overline{f_2}(\overline{r}) \\ \vdots \\ \overline{f_{n_G}}(\overline{r}) \end{bmatrix} \rangle \approx \boldsymbol{W}^T \boldsymbol{G_G} \boldsymbol{W} \boldsymbol{J} = \boldsymbol{W}^T \mathcal{F}^{-1}(diag(\tilde{\boldsymbol{g}_G})\tilde{\boldsymbol{J}_G}) + \boldsymbol{N_G} + \boldsymbol{N_{EX}}. \quad (2.49)$$

Careful thought about the precorrection suggests that its cost does not eliminate the advantages of utilizing the FFT to compute the approximate contribution of far away sources to the scattered field measured at each panel edge. The intra-cell convolution for each cell, to compute $\boldsymbol{N_G}$, is of $O(n_C)$, where $n_C$ is the number of cells. The intra-cell direct interaction computation, $\boldsymbol{N_{EX}}$, is also $O(n_C)$. Assuming $n_C$ is proportional to the number of panels or edges, means that the FFTs for the grid approximation of far away interactions, still will dominate the overall computation cost in equation 2.49, at $O(n_G \log(n_G))$, a very dramatic reduction over the explicit matrix-vector product of equation 2.26.

## 2.7 Simulation and Fast Parameter Sweeps with Reduced Order Models

Most computational electromagnetic scattering analysis requires calculation of the scattered fields for a given problem, not just at a single frequency point, but at many frequency points. In addition to frequency dependency, the scattered fields are usually dependent on other parameters, such as the look angle from which an incident wave approaches the problem geometry. Typically, scattering analysis requires solving the system at a large, representative set of points for each parameter, so that computing scattered fields at each point in the set will accurately characterize the system behavior across each parameter's desired value range.

In the equations of earlier chapters, parameter dependencies were suppressed in the electromagnetic field and potential quantities being related. Examining the matrix

form of the discretized EFIE 2.26,

$$(\boldsymbol{\Phi}(s) + (s)^2 \boldsymbol{A}(s))\boldsymbol{J} = \boldsymbol{Z}(s)\boldsymbol{J} = s\boldsymbol{E}(s), \tag{2.50}$$

it is apparent that the two different matrix-vector multiplications describe quantities induced by the unknown current density at edges. $\boldsymbol{E}(s)$ corresponds to the known incident fields, which are also frequency dependent. $\boldsymbol{J}$ is the vector of $n_E$ unknown current density coefficients each of which scales a basis function, $\overline{J_S}(\overline{r}, s) \approx \boldsymbol{J}(s)^T \overline{\boldsymbol{f}}(\overline{r})$, $\boldsymbol{\Phi}(s)$ corresponds to the contribution to the gradient of the scalar potential associated with the scattered fields, and $\boldsymbol{A}(s)$ corresponds to the contribution to the vector potential associated with the scattered fields. Each entry of both $\boldsymbol{\Phi}(s)$ and $\boldsymbol{A}(s)$ consists of a summation of scaled terms,

$$\sum_{q=1}^{n_Q} \alpha_{osq} G(\overline{r_o}, \overline{r_{sq}}) = \sum_{q=1}^{n_Q} \alpha_{osq} \frac{e^{-ik\|\overline{r_o} - \overline{r_{sq}}\|}}{\|\overline{r_o} - \overline{r_{sq}}\|}, \tag{2.51}$$

each containing an evaluation of the Helmholtz Green function, corresponding to the interactions between a point $\overline{r_o}$ on an observation panel with panel index $o$ and $n_Q$ quadrature points $\overline{r_{sq}}$ on source panels with panel index $s$ and quadrature point index $q$. '$\alpha_{osq}$' is the weighting coefficient for the $os$ indexed interaction at the $q$-th quadrature point.

Depending on available computational resources, the need to solve equation 2.50 for full parameter sweeps (across entire desired ranges for each parameter) or to use the model for simulation can be prohibitively expensive. For example, in airborne radar simulations, the chosen set of parameter points must contain enough frequency points to characterize the scattering response for frequency ranges of interest and enough look angles to create an image of the target. In this example application, the set of parameter points can be quite large, in the thousands, tens of thousands, or even hundreds of thousands of points. If it requires minutes, hours, or even days to solve the system of equations at a single parameter point, then both simulation and computation of the scattered fields for full parameter sweeps might be infeasible.

A major goal of this research is to develop and implement new algorithms and

techniques to accelerate the solution of very large (many unknowns), parameter-dependent systems of equations across a large set of parameter points. We hope to develop a technique which not only can compute accurate approximations to the scattered field for the entire set of desired parameter points, but one which only requires a few full solves of the discretized EFIE 2.50 at appropriate parameter points [44, 15, 45, 11]. By choosing a frequency of interest, $s_T$, and plugging in the value into equation 2.50, we can solve for $\boldsymbol{J}(s_{TE})$ iteratively at a cost of $O(n_G \log(n_G))$, using the PFFT algorithm. However, even with PFFT acceleration, solving equation 2.50 for the current density over an entire range of frequency points can be prohibitively expensive.

## 2.7.1    Model Order Reduction

Model order reduction is a technique for generating a reduced order model (ROM) which retains parameter dependencies of the original system across a desired parameter range and retains certain properties of the original model. One can readily compute an accurate approximation to desired scattering quantities[23] which characterize the original system from the induced current densities ($y(s) = \boldsymbol{C}^T \boldsymbol{J}(s)$) yielded by solving the ROM by the source at a given parameter point. Since the smaller system of equations of the ROM can solved far more rapidly than the original system of equations, an accurate approximation to the behavior of original system across the desired parameter range can be quickly computed by solving the ROM at each point in a large, representative set of parameter points.

The properties of the original model that will be retained by a ROM are key choices in selecting a MOR algorithm. One method of generating a ROM which accurately approximates the parameter dependency of the original system is based on constructing the ROM to match a certain number of the most significant terms (derivatives) of the Taylor Series representation of the original system, around a carefully selected expansion point. If a new ROM is constructed which matches

---

[23]The desired scattering quantities, denoted $y(s)$, could be scattered field, radar cross section, etc at a chosen observation point

a greater number of terms (and assuming parameter dependencies meet necessary constraints), then the new ROM will model the parameter-dependent behavior of the original system with greater accuracy. MOR techniques of this type, which force the ROM to match terms in the Taylor series representation of the system, are classified as "moment matching" methods. The name stems from the fact that the terms in the Taylor series are often called "moments", particularly when the parameter is frequency.

Using MOR, we hope to solve the full system of EFIE equations, of dimension $n_E$, at only a few, carefully selected parameter points, and then use those solutions to construct a projection [18] matrix which projects a Taylor series expansion (with respect to parameters) of the original EFIE matrices into a subspace of much lower dimension, $q$, thereby generating a reduced order model. The projection matrix is selected to force the ROM to match $q$, moments of the original system. Thus, the ROM retains the desired parameter dependencies because it matches the 1st $q$, terms in Taylor series representation of the original system of equations. If the order of the model is low enough ($q << n_E$), then solving the model at every point in the set of desired parameter points will be trivial, and approximations to the scattered field will be readily constructed from the solutions yielded by the model, using the projection matrix.

Hopefully, extending MOR techniques to handle the unique challenges posed by electromagnetic scattering applications, and integrating the resulting methods into our solver for the EFIE equations, will result in a solver that is able to compute accurate approximations to the scattered fields for the entire desired ranges of frequencies and look angles at a cost equivalent to a few full-system solves. Thus, if the solver uses iterative methods without sparsification techniques, the cost of computing approximate behavior for the entire parameter range (potentially thousands or tens of thousands of points) will be $O(qn_E^2)$ vs $O(n_E^2)$ operations, roughly the same cost for solving the equations at one parameter point. Obviously, if the MOR techniques are compatible with sparsification algorithms, the cost will be much less. For the PFFT sparsification algorithm, discussed in section 2.6.4, this cost would be $O(n_G \log(n_G))$,

66

to approximate the solution of the $n_E$ equations with $n_E$ unknowns over an entire range of parameter points.

## 2.7.2 Review of Moment Matching MOR

Due to the computational efficiency of projection via moment matching, we have chosen to implement this class of MOR algorithms. There is a wealth of literature describing these techniques including [18, 5, 13, 41, 42, 31, 35, 7, 6, 9] just to name a few. Of these, [18] is certainly the most comprehensive treatment.

Before considering how to modify MOR methods to handle challenges posed by electromagnetic scattering applications, we will briefly review the traditional MOR techniques by applying MOR to a simple first order (rather than the higher order frequency dependencies present in equation 2.50) system of equations,

$$\underbrace{(\boldsymbol{I} - s\boldsymbol{X})}_{\boldsymbol{Z}_{(s)}} \boldsymbol{J} = \boldsymbol{B}u$$

$$y = \boldsymbol{B}^T \boldsymbol{J} \qquad (2.52)$$

Above, the identity matrix $\boldsymbol{I}$ and $\boldsymbol{X}$ are the system matrices with $n_E \times n_E$ real elements, $\boldsymbol{J}$ and $\boldsymbol{B}$ are column vectors with $n_E$ elements, and $y$ and $u$ are scalars. $\boldsymbol{J}$ is the unknown state vector, $u$ is the input, $\boldsymbol{B}$ also selects components of the state vector which are relevant to the desired output, and $y$ is the desired output. $\boldsymbol{I}$, $\boldsymbol{X}$, and $\boldsymbol{B}$ are constant with respect to frequency. The frequency variable, $s$, in the equations replaces a time derivative and indicates equation 2.52 is the Fourier Transform of first order differential equations. Equation 2.52 describes the frequency domain[24] of the system. After solving for $\boldsymbol{J}$ and expanding the result with a Taylor Series, the equations can be rewritten,

---

[24]Apart from the governing differential equations, used to describe the various applications, the rest of the equations within this thesis are transformed into the frequency domain.

$$\boldsymbol{J}(s) = (\boldsymbol{I} - s\boldsymbol{X})^{-1}\boldsymbol{B}u = \sum_{j=0}^{\infty} s^j \underbrace{(\boldsymbol{X}^j\boldsymbol{B})}_{\text{Vector}} u, \tag{2.53}$$

Substituting the solution of $\boldsymbol{J}$, from equation 2.53, into the output equation $y = \boldsymbol{B}^T\boldsymbol{J}$, one obtains:

$$y(s) == \sum_{j=0}^{\infty} s^j \underbrace{[\boldsymbol{B}^T\boldsymbol{X}^j\boldsymbol{B}]}_{\text{moments: } m_j} u(s) = h(s)u(s). \tag{2.54}$$

In equation 2.54, $m_j$ are the moments of $h(s)$, the system function which relates the input $u(s)$ to the output $y(s)$. Equation 2.54 defines the moments $m_j$ which are used in the moment-matching Model Order Reduction algorithm.

Moment-matching MOR methods assume that lower order moments are most important to approximate the exact solution, and the reduced order model is constructed to match a certain number, $q$ of the lowest order moments of the original output, $y(s)$. If the largest singular value, $\sigma_{MAX} = max[\boldsymbol{X}]$, of the system $\boldsymbol{X}$ is less than one then the absolute value of the moments $m_j$ , will decrease with increasing $i$. In this case, it is clear that any approximating function $h_{APPROX}(s)$ would approximate $h(s)$ with error $\|h_{APPROX}(s) - h(s)\| \leq (\sigma_{MAX}^{q+1})/(1 - \sigma_{MAX})$, and if $q$ is chosen large enough, the neglected terms corresponding to the moments $m_q, m_{q+1}, \ldots$ will be negligible for frequencies close to a given expansion point if $h_{APPROX}(s)$ matched the first moments in the Taylor series expansion of $h(s)$, shown in equation 2.53. This approximation error will decrease if $q$, the number of matching moment terms, is increased.

Equation 2.53 highlights the fact that the vectors $[\boldsymbol{X}^j\boldsymbol{B}] =$ form a basis for the solution space, $\boldsymbol{J}$:

$$\Rightarrow \boldsymbol{J}(s) \in \left\{\boldsymbol{B}, \boldsymbol{X}\boldsymbol{B}, \boldsymbol{X}^2\boldsymbol{B}, \ldots\right\} \tag{2.55}$$

and from linear algebra's Cayley Hamilton Theorem [21], we know that only the first

$n_E$ terms are required to form a complete basis of the solution space $\boldsymbol{J}$:

$$\boldsymbol{J}(s) \in \left\{ \boldsymbol{B}, \boldsymbol{X}\boldsymbol{B}, \boldsymbol{X}^2\boldsymbol{B}, \ldots, \boldsymbol{X}^{n_E}\boldsymbol{B} \right\} \tag{2.56}$$

If the singular values of $\boldsymbol{X}$ have magnitudes much less than one, as discussed earlier, we can utilize ideas from Krylov-based Model Order Reduction (MOR) methods [18] to generate a reduced order model whose Taylor series expansion matches the most significant moments, corresponding to a *subset* of the solution space of the original system described by equation 2.56, such that the lower order model of size $q$ is small enough ($q << n_E$) to be rapidly solved for frequency sweeps.

The key step to generating a small ROM that accurately approximates the frequency behavior of the original system is to create a projection matrix $\boldsymbol{V}$ that contains a subset ($q << n_E$) of the "most important" or lowest order vectors in the solution space:

$$\begin{aligned} \boldsymbol{V} &= \begin{bmatrix} \boldsymbol{v_1} & \boldsymbol{v_2} & \cdots & \boldsymbol{v_q} \end{bmatrix}, \quad q << n_E \\ \boldsymbol{v_j} &\in \left\{ \boldsymbol{B}, \boldsymbol{X}\boldsymbol{B}, \boldsymbol{X}^2\boldsymbol{B}, \ldots \boldsymbol{X}^{q-1}\boldsymbol{B} \right\} \quad | \quad \boldsymbol{V}^T\boldsymbol{V} = \boldsymbol{I} \end{aligned} \tag{2.57}$$

Note that each new column, $\boldsymbol{v_j}$, of $\boldsymbol{V}$ is constructed by Arnoldi procedures to be orthogonal to the previous columns because, otherwise, repeated multiplication by the same matrix causes the result vector to gradually align in the direction of the largest eigenvalue. Thus the projection matrix $\boldsymbol{V}$ is an orthogonal basis for a $q$-dimensional subspace of the space described by equation 2.55. The first step in constructing the reduced order model or ROM is to approximate the unknown state vector $\boldsymbol{J}$ as a linear combination of the columns of the projection matrix $\boldsymbol{J} \approx \boldsymbol{V}\widehat{\boldsymbol{J}}$.

$$(\boldsymbol{I} - s\boldsymbol{X})\underbrace{\boldsymbol{V}\widehat{\boldsymbol{J}}}_{\approx \boldsymbol{J}} \approx \boldsymbol{B}u \tag{2.58}$$

Multiplying the left side of the equations 2.58 by $\boldsymbol{V}^T$ and solving the resulting system for the new unknown $\widehat{\boldsymbol{J}}$ of the ROM forces a solution that minimizes the
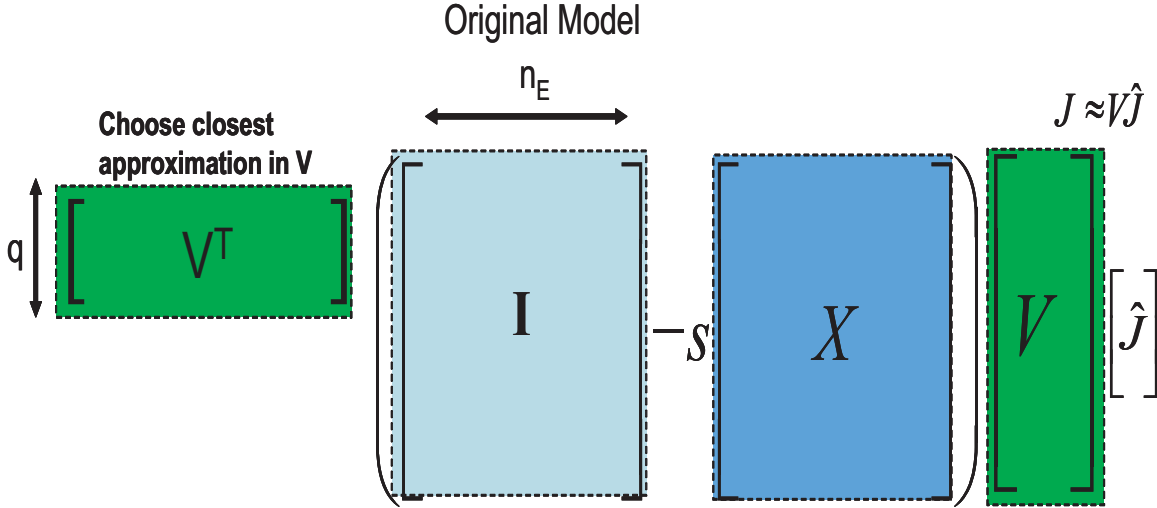
69

Figure 2-12: MOR: This figure illustrates how the projection matrix $\boldsymbol{V}$ is used to project the original $n_E$-dimensional system into a smaller $q$-dimensional subspace. Note that $\boldsymbol{V}$ is long, comprised of $n_E$-length columns, but narrow, having only $q$ of the $n_E$-length columns

residual,

$$(\boldsymbol{I} - s\boldsymbol{X})\boldsymbol{V}\widehat{\boldsymbol{J}} - \boldsymbol{B}u, \tag{2.59}$$

and the result is a ROM is generated by projecting each component of the original system to the lower $q$-dimensional subspace described spanned by the columns of $\boldsymbol{V}$:

$$\begin{aligned}
\boldsymbol{V}^T(\boldsymbol{I} - s\boldsymbol{X})\boldsymbol{V}\widehat{\boldsymbol{J}} - \boldsymbol{V}^T\boldsymbol{B}u &= 0 \\
&\downarrow \\
(\widehat{\boldsymbol{I}} - s\widehat{\boldsymbol{X}})\widehat{\boldsymbol{J}} - \widehat{\boldsymbol{B}}u &= 0.
\end{aligned} \tag{2.60}$$

where $\widehat{\boldsymbol{B}} = \boldsymbol{V}^T\boldsymbol{B}$, $\widehat{\boldsymbol{X}} = \boldsymbol{V}^T\boldsymbol{X}\boldsymbol{V}$, and $\widehat{\boldsymbol{I}}$ is the $q \times q$ identity matrix. Note that the resulting system of equations is $q$ equations each with $q$ unknowns, where $q << n_E$. The process is illustrated graphically in figures 2-12 and 2-13.

Since the $q \times q$ ROM system is very small, it can be solved almost instantaneously (relative to the original $n_E \times n_E$ system) for the unknown ROM current coefficient $\widehat{\boldsymbol{J}}$, and an approximation to the original current density can be obtained:

**Reduced Order Model**

Figure 2-13: ROM: The reduced order model has a $q$-length unknown $\widehat{\boldsymbol{J}}$ which represents the approximate solution which minimizes the residual of the approximating system.

$$
\begin{aligned}
\boldsymbol{J} &\approx \boldsymbol{V}\widehat{\boldsymbol{J}} \\
&= \boldsymbol{V}(\widehat{\boldsymbol{I}} - s\widehat{\boldsymbol{X}})^{-1}\widehat{\boldsymbol{B}}u,
\end{aligned}
\tag{2.61}
$$

where the "reduced" unknown state vector $\widehat{\boldsymbol{J}}$ will match the first $2q$ moments of the Taylor series representation of the original $\boldsymbol{J}$ [18]. An approximation to the desired output quantity $y$ is computed easily from the ROM:

$$
y \approx \boldsymbol{B}^T \boldsymbol{V}\widehat{\boldsymbol{J}}
\tag{2.62}
$$

Since the ROM matches the first 2q moments of the original system, the error in this ROM-approximated output solution will be:

$$
\chi = |\sum_{j=2q}^{\infty} s^j \widehat{\boldsymbol{X}}^j \widehat{\boldsymbol{B}}u - \sum_{j=2q}^{\infty} s^j \boldsymbol{X}^i \boldsymbol{B}u|
\tag{2.63}
$$

However, once the ROM is created, the cost to compute $h(s)$, for the entire desired frequency range is very small, $O(q^3)$ or $O(q^2)$, depending on whether Gaussian Elimination or iterative techniques are faster for the small system.

## 2.7.3 Multi-point Model Order Reduction

Sometimes, the range of frequencies around the frequency point is large enough that a reasonably-sized ROM will fail to accurately characterize the behavior of the orig-

inal system over the entire frequency range. Multi-point Model Order Reduction, described in [18], is a method for creating a ROM that simultaneously matches a small number of low order moments for multiple Taylor series expansions, each at different expansion point.

Considering the original system in the equations 2.53, simple algebra manipulations yield an equivalent set of equations:

$$
\begin{aligned}
\boldsymbol{J}(s) &= (\boldsymbol{I} - s_l \boldsymbol{X} + s_l \boldsymbol{X} - s \boldsymbol{X})^{-1} \boldsymbol{B} u \\
&= [(\boldsymbol{I} - s_l \boldsymbol{X}) - (s - s_l) \boldsymbol{X}]^{-1} \boldsymbol{B} u \\
&= [\boldsymbol{I} - (s - s_l) \underbrace{(\boldsymbol{I} - s_l \boldsymbol{X})^{-1} \boldsymbol{X}}_{\acute{\boldsymbol{X}}}]^{-1} \underbrace{(\boldsymbol{I} - s_l \boldsymbol{X})^{-1} \boldsymbol{B}}_{\acute{\boldsymbol{B}}} u \\
&= [\boldsymbol{I} - (s - s_l) \acute{\boldsymbol{X}}]^{-1} \acute{\boldsymbol{B}} u \\
&= \sum_{j=0}^{\infty} (s - s_l)^j \underbrace{(\acute{\boldsymbol{X}}^j \acute{\boldsymbol{B}})}_{\text{Vector}} u,
\end{aligned}
\tag{2.64}
$$

Clearly the solution space of the unknown state vector $\boldsymbol{J}$ can *also* be described:

$$
\boldsymbol{J}(s) \in \left\{ \acute{\boldsymbol{B}}, \acute{\boldsymbol{X}} \acute{\boldsymbol{B}}, \acute{\boldsymbol{X}}^2 \acute{\boldsymbol{B}}, \ldots, \acute{\boldsymbol{X}}^{n_E} \acute{\boldsymbol{B}} \right\},
\tag{2.65}
$$

in addition to description of the solution space of equation 2.56, and a projection matrix $\boldsymbol{V}$ could be created:

$$
\begin{aligned}
\boldsymbol{V} &= [\ \boldsymbol{v_1} \quad \boldsymbol{v_2} \quad \cdots \quad \boldsymbol{v_q}\ ], \quad q << n_E \\
\boldsymbol{v_j} &\in \left\{ \acute{\boldsymbol{B}}, \acute{\boldsymbol{X}} \acute{\boldsymbol{B}}, \acute{\boldsymbol{X}}^2 \acute{\boldsymbol{B}}, \ldots \acute{\boldsymbol{X}}^{q-1} \acute{\boldsymbol{B}} \right\} \quad | \quad \boldsymbol{V}^T \boldsymbol{V} = \boldsymbol{I}
\end{aligned}
\tag{2.66}
$$

which would create a ROM that matches $2q$ moments of a Taylor expansion of the original system expanded around the frequency point $s_l$. Combining both of the projection matrices, described equations 2.57 and 2.66, and reorthogonalizing the result, one could generate a ROM that simultaneously matches $q$ moments of the original system around $s = 0$ and $s = s_l$ by creating $\boldsymbol{V}$ as the union of $q$ terms

around $s = 0$ and the $q$ terms around $s = s_l$ as follows:

$$V \;=\; [\; v_1 \quad v_2 \quad \cdots \quad v_{2q} \;], \quad q << n_E \tag{2.67}$$

$$v_j \;\in\; \left\{ B, XB, X^2B, \ldots X^{q-1}B, \acute{B}, \acute{X}\acute{B}, \acute{X}^2\acute{B}, \ldots \acute{X}^{q-1}\acute{B} \right\} \;\mid\; V^T V = I$$

Obviously, since $s_l$ was arbitrary and the projection-based MOR algorithm is linear, the principle of superposition can be applied by incorporating Taylor expansion terms for additional frequency expansion points into a projection matrix, as shown above, to generate a multi-point moment-matching ROM that matches q moments around each of an arbitrary number, $n_{MP}$ of Taylor expansion points. Thus, the resulting ROM would be of dimension $n_{MP} * q$.

## 2.7.4 ETAS Method of Model Reduction for systems with weakly oscillatory parameter dependencies

Applying the same system reduction techniques discussed in section 2.7.1 and demonstrated in equations 2.57- 2.60 to the EFIE ( 2.26) would be significantly more complicated than applying them to the system in (equation 2.52) because both sides of equation 2.26 of have frequency dependencies and the matrices $A(s)$ and $\Phi(s)$ themselves have complicated frequency dependencies. One idea is to approximate $Z(s)$ with a truncated Taylor series approximation:

$$[Z_0 + (s - s_T)Z_1 + \frac{(s - s_T)^2}{2}Z_2 + \cdots + \frac{(s - s_T)^{n_T-1}}{(n_T - 1)!}Z_{n_T-1}]J \approx B. \tag{2.68}$$

Note that now the matrices $Z_l$ are frequency independent. As described in [34], the introduction of new state variables,

$$J_0 \;=\; J,$$

$$J_1 = (s - s_T)J_0,$$

$$J_2 = (s - s_T)J_1/2,$$

$$J_3 = (s - s_T)J_2/3,$$

$$\vdots$$

$$J_{n_T-1} = (s - s_T)J_{n_T-1}/n_T - 1, \tag{2.69}$$

permits the equations 2.68 to be rewritten, and the final desired form for the system equations is achieved:

$$\left[\begin{bmatrix} Z_0 & 0 & \cdots \\ 0 & I & \ddots \\ \vdots & \ddots & \ddots \end{bmatrix} + \begin{bmatrix} -Z_1 & -Z_2 & -Z_3 & \cdots & -Z_{n_T-1} \\ \frac{I}{2} & 0 & 0 & \cdots & 0 \\ 0 & \frac{I}{3} & 0 & \cdots & 0 \\ \vdots & \ddots & \ddots & \ddots & 0 \\ 0 & 0 & 0 & \frac{I}{n_T-1} & 0 \end{bmatrix}\right] \begin{bmatrix} J_0 \\ J_1 \\ J_2 \\ \vdots \\ J_{n_T-1} \end{bmatrix} = \begin{bmatrix} B_0 \\ 0 \\ 0 \\ \vdots \\ 0 \end{bmatrix} \tag{2.70}$$

The remainder of this dissertation will refer to equation 2.70 as the Expanded Taylor Approximation System (ETAS). This ETAS corresponds to the original system from equation 2.52, and can be rewritten in simplified notation:

$$[\mathcal{Z}_1 - (s - s_T)\mathcal{Z}_2]\mathcal{J} = \mathcal{B}. \tag{2.71}$$

where $\mathcal{Z}_1$ and $\mathcal{Z}_2$ are the corresponding expanded matrix[25] terms of size $[(n_T - 1)n_E]x[(n_T - 1)n_E]$ and $\mathcal{J}$ and $\mathcal{B}$ are the corresponding expanded vector terms of size $[(n_T-1)n_E]$ in equation 2.70. Note that by multiplying both sides of equations 2.71 by $\mathcal{Z}_1^{-1}$ produces equations that have the same form as equation 2.52, the starting point for MOR. Thus, the entire MOR methodology presented earlier can be applied to generate a reduced order model (ROM) for a weakly oscillatory system $Z(s)J = E(s)$.

---

[25]Hereafter, cursive and bold matrices and vectors will refer to quantities which have ETAS form to distinguish them from the non-ETAS quantities to which they correspond.

# Chapter 3

# Complications for MOR of Electromagnetic systems in the Full-wave regime

Full-wave MOR based on the ETAS model (ETAS-FMOR) methods were designed [35] to approximate structures for which the minimum wavelengths of analysis are greater than the maximum diameter of the geometry, rather than "electromagnetically-large" (EM-Large) structures, which result in highly oscillatory kernels in some elements of the discretized EFIE system. This chapter will further highlight the limitations of ETAS-FMOR by considering examples both for analysis of EM-Large scattering targets and EM-Large interconnect structures.

## 3.1 Difficulties for full-wave ETAS-MOR

For large systems, Model Order Reduction is a critical step in characterizing the parameter-dependent behavior of a system. The linear system of equations 2.28 does approximate the frequency domain behavior of the original system but the matrices $\boldsymbol{R} + s\boldsymbol{L}(s)$ and $\boldsymbol{P}(s)$ are usually so large and dense that the impedance model's computational complexity precludes either simulation or solution at a very large number of frequency points. Unfortunately, the full-wave MOR methods based on the ETAS

model (ETAS-FMOR) fail to generate a lower-order ($n_T < 10$) ETAS approximation to the original system that is accurate over typical desired frequency ranges.

The pre-existing full-wave MOR method based on the ETAS model (ETAS-FMOR) [35] approximates each element of $\boldsymbol{Z}(s)$ with a low-order truncated Taylor Series expansion:

$$[\boldsymbol{Z_0} + i(k - k_T)\boldsymbol{Z_1} + \frac{(s - s_T)^2}{2}\boldsymbol{Z_2} + \cdots + \frac{(s - s_T)^{n_T-1}}{(n_T - 1)!}\boldsymbol{Z_{n_T-1}}]\boldsymbol{J} = \boldsymbol{B}. \qquad (3.1)$$

Each entry of the system matrix is constructed[1] by multiple evaluations of the Green's function, which is of the form $\frac{(e^{-j(2\pi fr)/c_0})}{r}$, where $r$ is the separation distance between the observation and source points on the scattering object.

A truncated Taylor Series expansion of the Helmholtz Green's function only serves as a good approximation over a desired frequency range if the successive terms rapidly grow smaller such that the omitted terms are negligible. Thus, for entries corresponding to larger interaction distances, a low-order polynomial will fail to approximate the sinusodal factor of the Helmholtz Green's function over the desired frequency range, because its argument is proportional to frequency and interaction distance and the interaction distances are large.

The following equation clearly illustrates that the neglected terms of the truncated Taylor series would only be negligible (over the desired frequency range) if $n_T$ is very large relative to the absolute value of the exponent:

$$e^{ix} = \sum_{j=0}^{n_T-1} \frac{(ix)^j}{j!} + \underbrace{\sum_{j=n_T}^{\infty} \frac{(ix)^j}{j!}}_{\to 0 \text{ if } n_T \gg |x|}. \qquad (3.2)$$

If $\lambda$ is wavelength (relative to expansion point) and $r$ is the interaction distance, full-wave analysis is defined to include frequencies for which $\frac{r}{\lambda} \geq 1$. Therefore, for full-wave scattering analysis, where $|x| = 2\pi\frac{r}{\lambda}$, corresponds to $|x| > 2\pi$, equation 3.2

---

[1]Numerical quadrature is utilized to compute the integral of the product of the greens function and current density over the panels corresponding to a each particular entry.

demonstrates that an accurate Taylor approximation would require $n_t >> 6$ terms in the truncation, which is not "low-order" at all!!!

Considering impedance extraction for SoB and SoP, packages and boards are built on scale of centimeters. Thus, elements of the interaction matrix representing a SoB or SoP will have interaction distances between one to 20 centimeters, but often signals present on these electronic systems contain frequencies in excess of 15 GHz, which corresponds to wavelengths smaller than two centimeters. Thus, from the preceding paragraph the reader can verify that $kr$ values for these systems will probably range from $kr = 3$ to $kr = 10$ and a very large truncation order $n_T$ is needed for accurate approximation! As a result ETAS-based MOR would be inefficient.

Electromagnetic scattering analysis frequently involves even more challenging problems. Appendix A lists some typical ground vehicles that might be surveilled by military radar. Consider the scattering from one of those targets due to a source wave with a frequency of 800 MHz: The sinusoidal exponential has an exponent of magnitude $\frac{8\pi r}{3}$ or approximately $8r$ radians. For the simulation of electromagnetic scattering from ground vehicles such as tanks, the separation distances in the Helmholtz Green's functions will be on the order of 10 meters. Thus, for this problem, accuracy requires $n_T >> 80$ terms in a truncated Taylor expansion. For the ETAS, this corresponds to $80 * n_E^2$ entries in the dense portion of the matrix, or roughly $80\times$ the number of operations for a matrix-vector product, making efficient computation of a ROM far less feasible!!!

On the other hand, if the truncation order is kept low, then the ETAS model accuracy will suffer. To demonstrate this shortcoming of ETAS models, scattering analysis of an "electromagnetically large", long, thin wire, illustrated in figure 3-1(a), is performed in a full-wave frequency regime from 80 to 800 MHz. The accompanying results figure 3-1(b) plots the log of relative error of the approximate current density computed from the ETAS model (○), with a low truncation order $n_T = 6$. This figure clearly shows that the ETAS model has a very narrow range of accuracy (highlighted by the dashed lines)! Furthermore, the same figure compares results computed from an ETAS-based ROM (.) that was generated using multi-point MOR to match ETAS

(a) Long thin wire: Over the frequency range, the wire has length $.3\lambda$ to $3\lambda$.
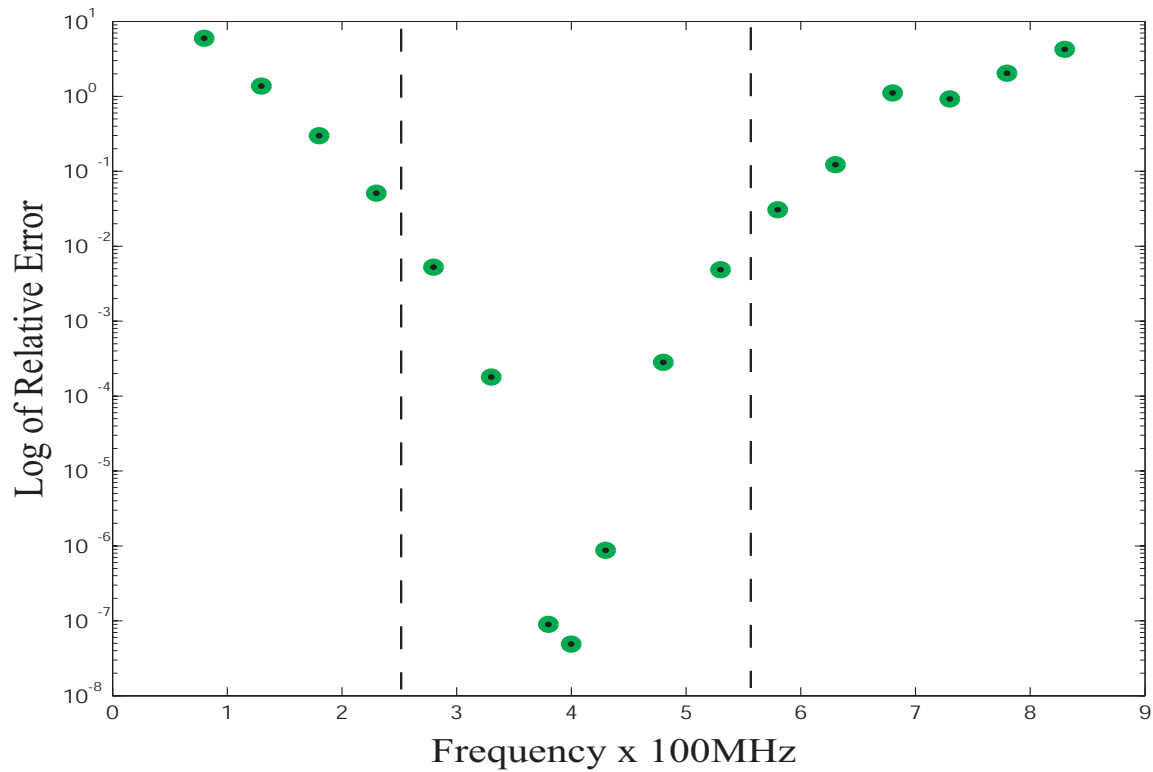


(b) This figure plots the log of the relative error of the ETAS model ($\circ$) for the EM-large long thin wire in a full-wave frequency regime. The results illustrate that the ETAS Model ($\circ$) with $n_T = 6$ has a narrow band of accuracy around the expansion point at 400 MHz. The dashed lines demark a zone, 250 to 560 MHz, with relative error $< .1$. The ETAS-MOR ROM (.) matches the ETAS model over the entire frequency range. Each '.' is within a '$\circ$' !

moments around 250 MHz and 600 MHz, in addition to the central expansion point for the ETAS at 400 MHz. The figure clearly shows while the ETAS-based ROM matches the ETAS at each point in the frequency range, the ETAS model itself has a very poor range of accuracy!

## 3.2 Difficulties for full-wave multi-point ETAS-MOR

Multi-point Model Order Reduction, introduced in [18], is a method to include moments or Taylor Expansion terms from additional expansion points into the subspace spanned by the Projection Matrix $V$ so that a ROM will also match moments of the original model around the additional expansion points. Thus, multi-point MOR is an important tool to extend the frequency range in which ROMs accurately characterize the frequency response of the system. Since the ETAS-FMOR ROMs are accurate in a very narrow range around the expansion point, creating ROM's that match additional expansion points would seem to be the missing key for ETAS-FMOR. Figure 3-1(b) demonstrates that existing multi-point techniques are inadequate to improve full-wave ETAS-based FMOR. The ROM in figure 3-1(b) is computed with two additional ETAS based multipoints at 180 MHz and 680 MHz, yet there are no "dips" corresponding to the additional expansion points, indicating that the inclusion of these additional terms in the projection matrix contributes little to nothing to improve the range of accuracy of the ROMs.

The lack of accuracy improvement or error reduction around the additional expansion points raises questions regarding the utility of the multi-point MOR methods: Are the multi-point MOR algorithms even working properly? The answer is yes, but to understand why, one must remember that constructing ROMs using Krylov subspace projection-based MOR to generate a ROM for frequency dependent system "essentially involves" TWO truncated Taylor Approximations. The first truncated Taylor approximation, described in section 2.7.4, is used to eliminate frequency dependency from the matrix elements and to algebraically manipulate the system into a form similar to equation 2.52 that is conducive for MOR, while the other Taylor

expansion is implicitly incorporated[2] into the model during the process of matching moments or Taylor expansion terms that occurs during construction of the Krylov subspaces for the MOR Projection Matrix $V$, described in section 2.7.2. Thus, although it is disappointing that the results computed from the ROM do not match those of the original system, the multi-point MOR algorithms are working extremely well because the ROM solutions match those of the ETAS (from which it was reduced) almost precisely over the entire range.

Should there be "dips" in error at the additional expansion points where the ROM has been forced (via multi-point MOR) to match the ETAS? The ETAS itself approximates the system about only the original expansion point and is highly inaccurate at the additional expansion points. Multi-point MOR, described in [18], forces the resulting ROM to match the ETAS at the additional expansion points. Due to the double Taylor Approximation, the best that the ETAS-based multi-point ROM can do is match the ETAS results exactly over the entire range. In fact, the ETAS-FMOR ROM matches the ETAS exactly, indicating that increasing the ROM size will not improve accuracy and that only increasing $n_T$, the truncation order of the ETAS can improve the accuracy! Therefore, the existing multi-point MOR methods are clearly not that useful to improve the ETAS-FMOR ROM accuracy. It could be highly beneficial to develop new techniques for multi-point MOR in the context of ETAS.

## 3.3 Conclusion

Certainly, logic suggests that attempting to approximate a rapidly oscillating sinusoidal functions over a wide frequency range with low-order polynomials is doomed to fail. On the other hand, employing some other basis functions to approximate the Green's function could destroy various properties of the parameter dependencies and preclude the wealth of MOR techniques that have already been developed and described in the literature. A nice property of the Taylor Expansion-based ETAS

---

[2]Note that the resulting ROM is not a finite polynomial representation of the original solution space, but an infinite series "reduced" representation that has been forced to match $q$ of the first terms in the Taylor Expansion of the original solution space.

method for full-wave MOR (ETAS-FMOR) is that these methods facilitate the standard MOR algorithms. Therefore, before giving up on Taylor Expansion completely, it is worthwhile to observe that many elements of the truncated Taylor approximation matrix will be reasonable approximations over the desired frequency range because the separation distances are small enough. This observation suggests possible avenues to explore which lead to the new Segregation by Primary Phase Factors MOR algorithms that are the contribution of this research and are presented in subsequent chapters.

# Chapter 4

# Segregation by Primary Phase Factors

Segregation by Primary Phase Factors (SPPF) is a new algorithm for full-wave MOR. The full-wave regime poses challenging difficulties for MOR based on the ETAS model. The discussion in chapter 3 suggested that polynomials, by themselves, may be insufficient to construct a *low-order and accurate* approximation to the system's frequency dependencies in a full-wave analysis regime for a reasonable desired frequency range. However, it is also desirable to find a method that incorporates the rich Krylov-subspace, Projection-based MOR theory that has already been established. Sections 2.7.1 through 2.7.4 of chapter 2 presented a brief overview of the subset of these techniques that are relevant to this dissertation and provided some references for further details. The new SPPF full-wave MOR algorithms are based on a new expanded Taylor approximation to the system (SPPF-ETAS) and will take full advantage of the existing MOR theory to generate reduced order models to accelerate full-wave analysis of "electromagnetically large" structures that are accurate over much wider desired frequency ranges.

Both the goals outlined in the preceding paragraph and the observations discussed in section 3 motivate the SPPF algorithm. The basic steps for SPPF are:

- Classify interactions into discrete "distance bins"

- Decompose interactions into primary and remainder phase

- Segregate system $\boldsymbol{Z}$ by primary phase factors

- Compute Taylor Approximation to "remainder phase"

- Apply full-wave MOR

Each of these steps will be described in detail in sections 4.1 to 4.5, which follow.

## 4.1 Classify interactions into discrete "distance bins"

The Helmholtz Green's Function, corresponding to full-wave EM analysis, is:

$$G_H(r) = \frac{e^{-jkr}}{r}. \tag{4.1}$$

Although the wave number $k$ is the official "frequency variable" from the physical EM problem, from a more general mathematical viewpoint, it is also possible to consider $r$ to be a "frequency variable" with respect to the degree oscillation of the sinusoid over values of some variable $k$. The basic idea of the Segregation by Primary Phase Factors algorithm is to classify the Green's function evaluations of the system matrix according to the size of the interaction[1] distances $r$ , and SPPF divides the range of possible interaction distances into equally spaced segments of length $\breve{R}$, the SPPF parameter[2]. The entries of $\boldsymbol{Z}_{mn}$ are decomposed and classified by the integer value $l_{mn}$, corresponding to its separation distance, $r_{mn}$, using the relation: $r_{mn} = l_{mn}(\breve{R}) + d_{mn}$, where $d_{mn} < \breve{R}$. Thus, every entry $\boldsymbol{Z}_{mn}$ of the system matrix is classified into a segment or "bin" based on its separation distance as illustrated in Figure 4-1.

---

[1] Entries of $\boldsymbol{Z}(s)$ describe interactions between source and observation points

[2] $\breve{R}$ is chosen such that $\breve{R} < r_{MAX}$, where $r_{MAX}$ is the maximum diameter of the structure. This choice ensures the algorithm will produce a more accurate ROM than the existing MOR methods.
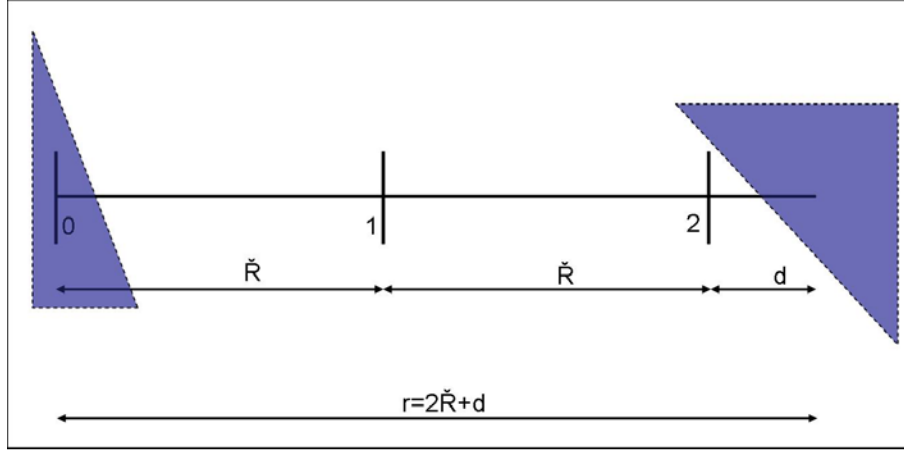
Figure 4-1: Segregation into Primary Phase Factor bins: In this example, the distance $r$ between a pair of triangular panels is classified into the second SPPF bin since $r = 2\breve{R} + d$, and during any computations this interaction would be segregated into a group with all other interactions corresponding to the same Primary Phase Factor of $e^{-ik2\breve{R}}$. This particular interaction would obviously have a remainder phase factor of $e^{-ikd}$.

## 4.2 Decompose interactions into primary and remainder phase

To decompose phase of the entries according to integer multiples of the SPPF parameter $\breve{R}$, the SPPF algorithm applies De Moivre's Theorem[3] for exponential functions to the Helmholtz Green's function evaluations required at each entry during construction of the system matrix $\boldsymbol{Z}(s)$:

$$\boldsymbol{Z}_{mn} = z_{mn}\frac{e^{-ikr_{mn}}}{r_{mn}} = z_{mn}\frac{e^{-ik(\breve{R}l_{mn}+\overbrace{d_{mn}}^{d_{mn}<\frac{\breve{R}}{2}})}}{r_{mn}} = z_{mn}e^{-ik\breve{R}l_{mn}}\frac{e^{-ikd_{mn}}}{r_{mn}}, \qquad (4.2)$$

where $l_{mn} \in 1, \cdots, \breve{n}$, and $\breve{n}$ corresponds to $r_{MAX}$. In this manner, the entries of equation 4.2 are decomposed into a primary phase component $e^{-ikl_{mn}\breve{R}}$ and a remainder phase component $e^{-ikd_{mn}}$, after the interaction distance, $r_{mn}$ is segregated into

---

[3]An exponential function with an exponent that is the sum of two terms equals a product of two of the same exponential functions each with one of the terms as the exponent: $a^{x+y} = a^x a^y$ and therefore $a^{nx} = (a^x)^n$.

a bin corresponding to its integer valued $l_{mn}$ using the relation: $r_{mn} = l_{mn}\check{R} + d_{mn}$, where $|d_{mn}| < \check{R}/2$,

Now, the main *purpose* for this manipulation starts to become clear: Once the exponential function is separated into two exponential function factors, the exponential factor containing the remainder term $d_{mn}$ in the exponent can be approximated *accurately* by a truncated Taylor series with *low number*, $(n_T)$, of terms:

$$\boldsymbol{Z}_{mn} \approx z_{mn}\frac{e^{-ik\check{R}l_{mn}}}{r_{mn}}(1 + -ikd_{mn} + \cdots + \frac{(-ikd_{mn})^{(n_T-1)}}{(n_T - 1)!}) \tag{4.3}$$

Thus, to ensure the approximation of each entry $\boldsymbol{Z}_{mn}$ is accurate over a desired frequency range of each entry, $\check{R}$ must be chosen so that a truncated Taylor Series approximation to the remainder term is acceptably accurate over the desired frequency range for all possible $|d_{mn}| < \check{R}/2$. In other words, the truncated terms in the truncated Taylor Series approximation for $\boldsymbol{e}^{-ikd_{mn}}$ must be negligible for all $k$ in the desired frequency range ($k = 2\pi f$). Clearly, for a given truncation order $n_T$, a choice of $\check{R} < r_{max}$ will result in improvement. For a given order, a truncated Taylor approximation of $\boldsymbol{e}^{-ikd_{mn}}$ will be accurate over a wider range than truncated Taylor expansion of $\boldsymbol{e}^{-ikr_{mn}}$. Smaller $\check{R}$ will achieve a wider bandwidth of accurate approximation around a selected Taylor expansion point.

## 4.3 Segregate system $\boldsymbol{Z}$ by primary phase factors

By classifying the separation distances into appropriate bins and decomposing each entry into primary and remainder phase components, the system matrix can be segregated into $\check{n}$ component matrices each corresponding to a different integer multiple of $\check{R}$ present in the separation distances of all of its entries, as shown in figure 4-2.

Using an operator $P_l$ that multiplies entries corresponding to the *lth* separation distance bin by 1 and multiplying all entries that are classified in other separation distance bins by 0, the equation corresponding to figure 4-2 can be segregated into sparse sub-matrices:
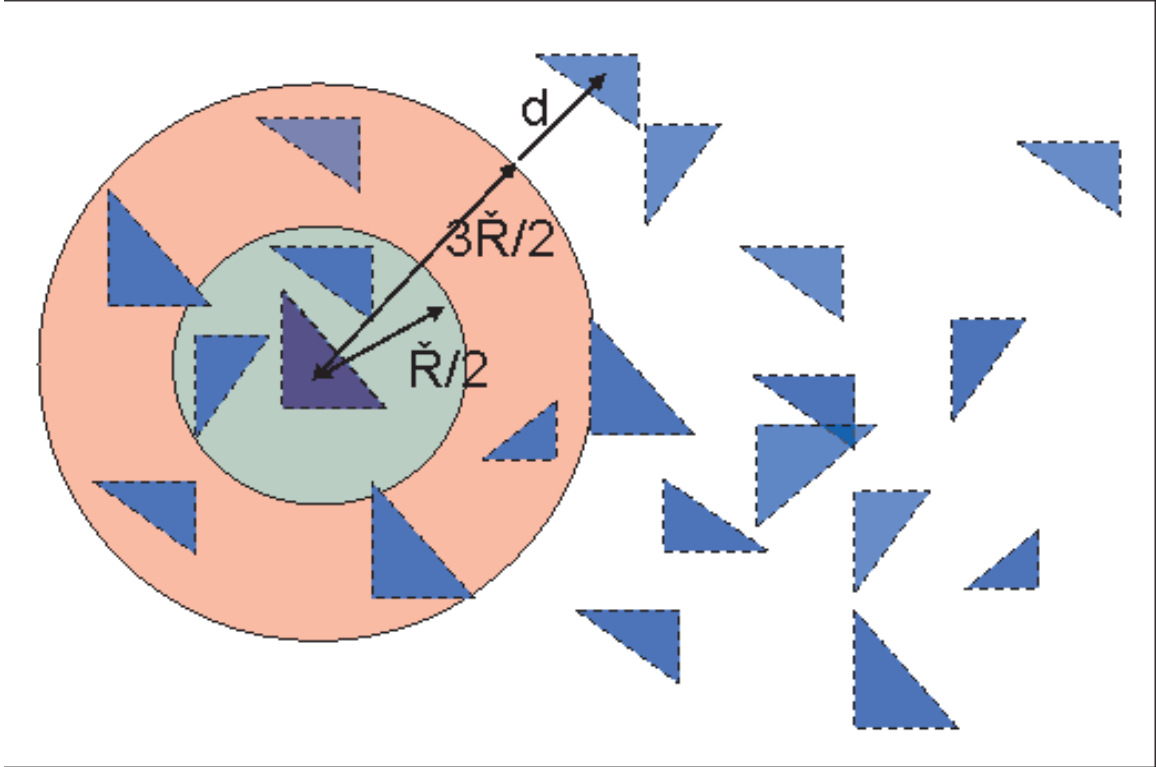
Figure 4-2: Segregating $\boldsymbol{Z}(s)$ by Primary Phase Factors: The innermost sphere around the indicated observation panel corresponds to the zero bin with primary phase factor of one, and the second innermost spherical shell corresponds to the $\check{R}$ bin with primary phase factor of $e^{-ik\check{R}}$. While the spherical shells corresponding to $e^{-ik2\check{R}}$, $e^{-ik3\check{R}}$, etc are not shown, the panels within a radius of $(m+1/2)\check{R}$ but greater than a radius of $max((m-1/2),0)\check{R}$ correspond to the $m$-th bin and have primary phase factor of $e^{-ikm\check{R}}$. Each such spherical shell also corresponds to group of entries in selected rows of the SPPF interaction matrix $\check{\boldsymbol{Z}}(s)$, and those rows correspond to the observation edges associated with the given panel.

$$Z(s) = e^{-ik\breve{R}0} P_0 \breve{Z}(s) + e^{-ik\breve{R}} P_1 \breve{Z}(s) + \cdots + e^{-ik\breve{R}\breve{n}} P_{\breve{n}} \breve{Z}(s), \qquad (4.4)$$

Note that $P_l$ is not a matrix and that a new SPPF system matrix $\breve{Z}$ is constructed: $\breve{Z}_{mn} = \frac{e^{-ikd_{mn}}}{r_{mn}}$.

In equation 4.4 , $P_0$ selects the entries of $\breve{Z}(s)$ corresponding to the $\breve{R}$ circle in above, $P_1$ selects the entries of $\breve{Z}(s)$ corresponding to the $2\breve{R}$ circle, and $P_2$ selects the entries of $\breve{Z}(s)$ corresponding to $3\breve{R}$ circle, which is not shown. Thus, the $P_l$ operator is used to segregate the original system into these sparse component matrices, each of which corresponds to the requisite $e^{-ik\breve{R}l_{mn}}$ factor present in each of those entries of the original matrix, and this step is how the algorithm was named Segregation by Primary Phase Factors (SPPF). This crucial segregation step enables *accurate and efficient* truncated Taylor approximation, which facilitates full-wave analysis using traditional MOR methods to develop accurate SPPF-based reduced order models (SPPF-ROMs)!

## 4.4   Compute Taylor Approximation to "remainder phase"

Because the entries, $\breve{Z}_{mn}(s)$ have small exponents ($|d_{mn}| < \breve{R}/2$, where $\breve{R}$ is chosen appropriately) or phase, the component matrices can be accurately approximated by truncating the Taylor Series representation of each element, resulting in:

$$
\begin{aligned}
Z(s) &= e^{-ik\breve{R}0} P_0 [\breve{Z}_0 + \Delta(s)\breve{Z}_1 + \cdots + \frac{\Delta(s)^{(n_T-1)} \breve{Z}_{(n_T-1)}}{(n_T - 1)!}] \\
&+ e^{-ik\breve{R}} P_1 [\breve{Z}_0 + \Delta(s)\breve{Z}_1 + \cdots + \frac{\Delta(s)^{(n_T-1)} \breve{Z}_{(n_T-1)}}{(n_T - 1)!}] + \cdots \\
&+ e^{-ik\breve{R}\breve{n}} P_{\breve{n}} [\breve{Z}_0 + \Delta(s)\breve{Z}_1 + \cdots + \frac{\Delta(s)^{(n_T-1)} \breve{Z}_{(n_T-1)}}{(n_T - 1)!}],
\end{aligned}
\qquad (4.5)
$$

Equation 8.2 and equation 4.4 are the key concepts behind the SPPF algorithm

that enables FMOR. Applying these ideas, Impedance Models[4], in the form of equation 2.28, can be expanded into the SPPF Expanded Taylor Approximation System (SPPF-ETAS),

$$
\begin{aligned}
\breve{\boldsymbol{\mathcal{Z}}}(s)\breve{\boldsymbol{\mathcal{J}}} = \sum_{j=0}^{\breve{n}} e^{-ik\breve{R}j} \boldsymbol{\mathcal{P}}_{|} & \left[ \left[ \begin{array}{cccc} \breve{\boldsymbol{Z}}_0 & \boldsymbol{0} & \cdots & \\ \boldsymbol{0} & \boldsymbol{I} & \ddots & \\ \vdots & \ddots & \ddots & \end{array} \right] \right. \\
+\Delta(s) & \left. \left[ \begin{array}{ccccc} -\breve{\boldsymbol{Z}}_1 & -\breve{\boldsymbol{Z}}_2 & -\breve{\boldsymbol{Z}}_3 & \cdots & -\breve{\boldsymbol{Z}}_{n_T-1} \\ \frac{\boldsymbol{I}}{2} & \boldsymbol{0} & \boldsymbol{0} & \cdots & \boldsymbol{0} \\ \boldsymbol{0} & \frac{\boldsymbol{I}}{3} & \boldsymbol{0} & \cdots & \boldsymbol{0} \\ \vdots & \ddots & \ddots & \ddots & \boldsymbol{0} \\ \boldsymbol{0} & \boldsymbol{0} & \boldsymbol{0} & \frac{\boldsymbol{I}}{n_T-1} & \boldsymbol{0} \end{array} \right] \right]
\left[ \begin{array}{c} \breve{\boldsymbol{J}}_0 \\ \breve{\boldsymbol{J}}_1 \\ \breve{\boldsymbol{J}}_2 \\ \vdots \\ \breve{\boldsymbol{J}}_{n_T-1} \end{array} \right] \approx \boldsymbol{\mathcal{B}}. \qquad (4.6)
\end{aligned}
$$

Equation 4.6 can be rewritten in simplified notation:

$$
\breve{\boldsymbol{\mathcal{Z}}}(s)\breve{\boldsymbol{\mathcal{J}}} = \sum_{j=0}^{\breve{n}} e^{-ik\breve{R}j} \boldsymbol{\mathcal{P}}_j (\breve{\boldsymbol{\mathcal{Z}}}_1 + (s-s_T)\breve{\boldsymbol{\mathcal{Z}}}_2)\breve{\boldsymbol{\mathcal{J}}} = \boldsymbol{\mathcal{B}}, \qquad (4.7)
$$

## 4.5   Apply full-wave Model Order Reduction to Impedance Models

Model Order Reduction methods can be readily applied to an impedance model approximated by equation 4.7 to yield a ROM, by pre-multiplying and post-multiplying with the projection matrix $\boldsymbol{\mathcal{V}}$ as follows:

---

[4]Scattering Models will be considered in chapter 5 because the right hand side source vectors have complicated frequency dependencies. The SPPF-FMOR algorithms will be extended for EM scattering.

$$
\hat{\breve{\mathcal{Z}}}(s)\hat{\breve{\mathcal{J}}} = \sum_{j=0}^{\breve{n}} e^{-ik\breve{R}j} \boldsymbol{\mathcal{V}}^T \boldsymbol{\mathcal{P}}_| \left[ \left[ \begin{array}{cccc} \breve{Z}_0 & 0 & \cdots & \\ 0 & I & \ddots & \\ \vdots & \ddots & \ddots & \end{array} \right] \right.
$$

$$
+\Delta(s) \left[ \begin{array}{ccccc} -\breve{Z}_1 & -\breve{Z}_2 & -\breve{Z}_3 & \cdots & -\breve{Z}_{n_T-1} \\ \frac{I}{2} & 0 & 0 & \cdots & 0 \\ 0 & \frac{I}{3} & 0 & \cdots & 0 \\ \vdots & \ddots & \ddots & \ddots & 0 \\ 0 & 0 & 0 & \frac{I}{n_T-1} & 0 \end{array} \right] \left. \right] \boldsymbol{\mathcal{V}} \left[ \begin{array}{c} \breve{\hat{J}}_0 \\ \breve{\hat{J}}_1 \\ \breve{\hat{J}}_2 \\ \vdots \\ \breve{\hat{J}}_{n_T-1} \end{array} \right] \approx \boldsymbol{\mathcal{V}}^T \boldsymbol{\mathcal{B}}. \quad (4.8)
$$

or in SPPF-ETAS matrix notation:

$$
\hat{\breve{\mathcal{Z}}}(s)\hat{\breve{\mathcal{J}}} \;\rightarrow\; \sum_{j=0}^{\breve{n}} \boldsymbol{\mathcal{V}}^T e^{-ik\breve{R}j} \boldsymbol{\mathcal{P}}_| (\breve{\mathcal{Z}}_1 - (s-s_T)\breve{\mathcal{Z}}_2)\boldsymbol{\mathcal{V}}\hat{\breve{\mathcal{J}}} = \boldsymbol{\mathcal{V}}^T\boldsymbol{\mathcal{B}}
$$

$$
= \sum_{j=0}^{\breve{n}} e^{-ik\breve{R}j}(\hat{\breve{\mathcal{Z}}}_{1j} - (s-s_T)\hat{\breve{\mathcal{Z}}}_{2j})\hat{\breve{\mathcal{J}}} = \hat{\mathcal{B}} \quad (4.9)
$$

The resulting MOR algorithm is called Segregation by Primary Phase Factors for Full-wave-MOR (SPPF-FMOR).

The astute reader might be wondering how the projection matrix $\boldsymbol{V}$ used in equation 4.8 was constructed. Although it is a subject for further research, it is unclear how to use the SPPF-ETAS to construct a Projection Matrix $\boldsymbol{\mathcal{V}}$ that can be used to generate a ROM. As the reader might have surmised, $\boldsymbol{\mathcal{V}}$ is based on the original ETAS system $\boldsymbol{\mathcal{Z}}(s)$ of equation 2.70 which was shown to be inaccurate description of the system for low-order, wideband approximations. If the ETAS is an inadequate model of the original system $\boldsymbol{Z}(s)$, what justification is there to use the ETAS to form a projection matrix $\boldsymbol{V}$, the basis for the ROM approximation?

The ETAS is inaccurate because it lacks components (Taylor expansion terms) in the frequency solution space, not because the components it possesses are incorrect. Therefore, this ETAS does contain a subset of the components that are present in

the exact system, and basis "directions" formed using the ETAS for the Projection Matrix's Krylov-subspace will be present in the original solution space. This reasoning suggests that the original ETAS still might be helpful in generating the Projection Matrix $V$ required for MOR. This subject will be explored further in later chapters, but the results presented in the next section demonstrate that this choice seems to work.

## 4.6 Results of SPPF-FMOR

This section present results of applying SPPF-FMOR to generate reduced order models. Two example problems illustrated in figure 4-3 were selected for this demonstration:

- Transmission Line with 10 ohm resistance

- Transmission Line with open circuit

A modified version of the Fast Pep solver [23] was used to generate the original models of dimension $n = 183$, in the form of equation 2.28, for each of these structures. It should be noted, while these SIE-based BEM techniques enable modeling of structures with arbitrary geometries, transmission lines were chosen because the results can be verified analytically and to save compute time. However, as the reader will see, these simple examples will illustrate the great potential of SPPF-FMOR for full-wave analysis!

For the Transmission line with 10 ohm resistance, figure 4-4(a) compares the phase of the admittance computed by the original model, SPPF-FMOR model, and the ETAS-FMOR model, and figure 4-4(b) compares the log of the relative magnitude of the error of the current computed by ROMs generated by both the new SPPF-FMOR algorithm and standard FMOR based on the ETAS model (MOR-ETAS). Comparison of results shows that the new SPPF-FMOR algorithm achieves relative error almost 10 to 100 times (or one to two decades) smaller than MOR-ETAS, over the entire frequency range up to 15 GHz!!!
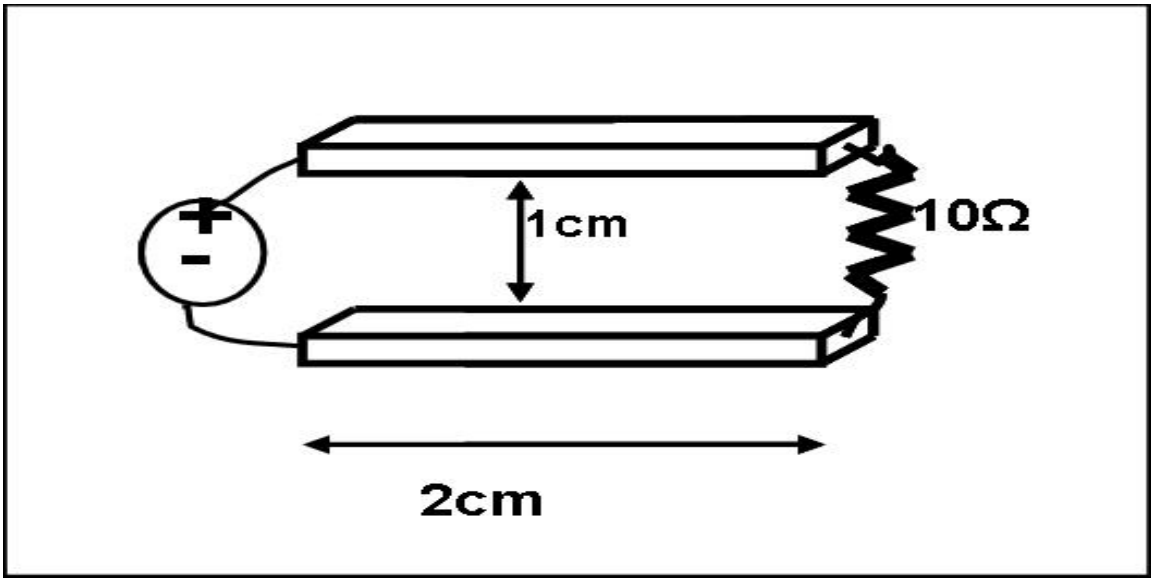
Figure 4-3: 2 Transmission Line examples (length=2cm, separation=1cm, width=37e-6m , height=15e-6m ): One example has the 10 ohm resistor shown in this figure. Another example, which is not shown, has an open circuit instead of the resistor.
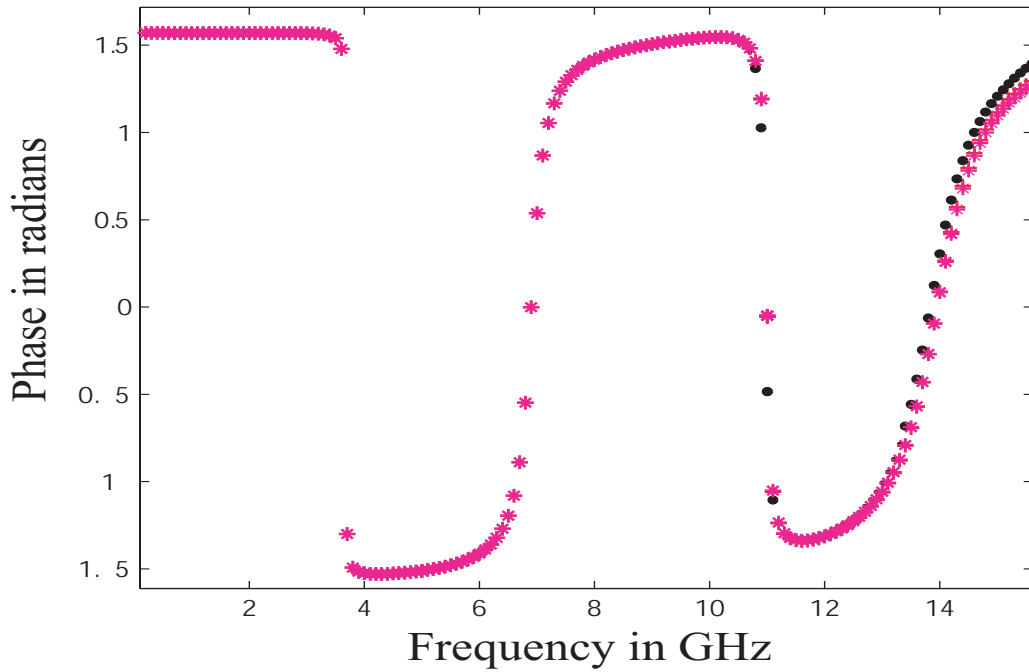
For the Transmission line open circuit, figure 4-4(d) plots the log of the relative magnitude of the error for both the new SPPF-FMOR algorithm and the pre-existing MOR-ETAS algorithm. Comparison of results shows that the new SPPF-FMOR algorithm achieves relative error almost 100 to 1000 times (or two to three decades) smaller than MOR-ETAS, over the entire frequency range up to 15 GHz!!!
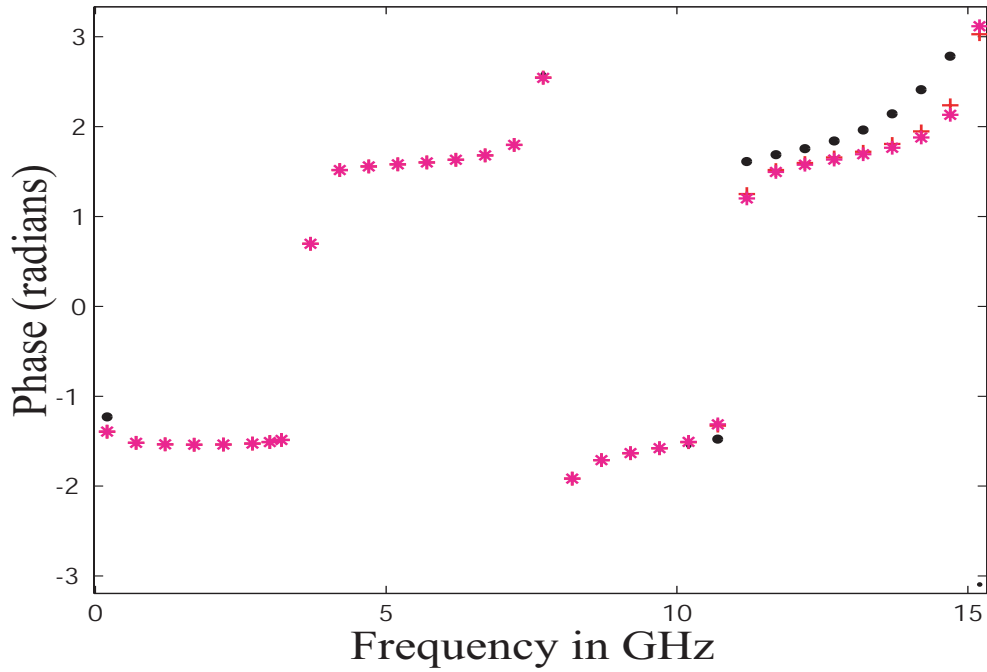
(a) Transmission Line with 10 ohm resistance: Phase of the Admittance computed by original model(+), SPPF-FMOR (*), and ETAS-FMOR(•). The SPPF-FMOR model matches the original over the entire frequency range up to 15Ghz (the + symbols are not visible beneath the * symbols) but the ETAS-FMOR model(•) deviates after the resonance at 11GHz.
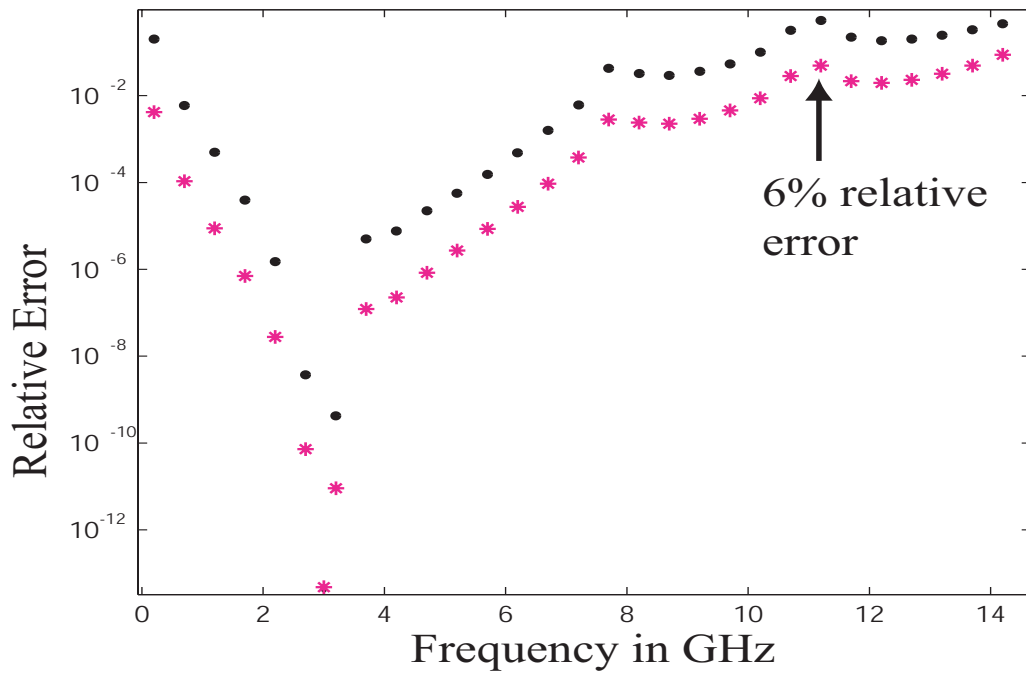


(b) Transmission Line with 10 ohm resistance: Log scale plot of Relative Error SPPF-FMOR(○) and standard MOR(•) vs frequency

93

(c) Transmission Line with open circuit: Phase of the Admittance computed by original model(+), SPPF-FMOR (*), and ETAS-FMOR(•). The SPPF-FMOR model matches the original over the entire frequency range up to 15Ghz (the + symbols are not visible beneath the * symbols) but the ETAS-FMOR model(•) deviates after the resonance at 11GHz.
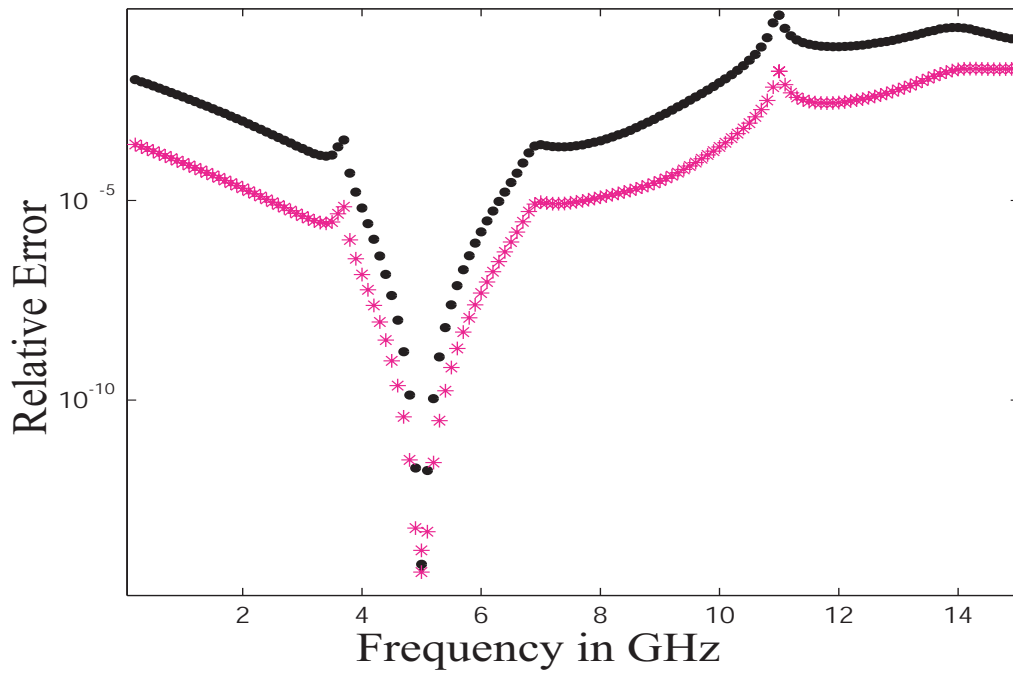


(d) Transmission Line with open circuit: Log scale plot of Relative Error SPPF-FMOR(*) and standard MOR(•) vs frequency.

94

# Chapter 5

# Full-wave Model Order Reduction for problems with source vectors that have complicated frequency-dependencies

Electromagnetic Scattering problems have more complicated frequency dependencies than Impedance Extraction problems. In the Interconnect analysis examples shown in section 4.6, the FastPep extraction tool computed full-wave models for the impedance behavior of the Interconnect. The impedance models had the form of equation 2.28, in which the source vector $B$ corresponded to a voltage or current source connected to a single panel of the discretization. Therefore, any frequency dependency could be easily factored from the source vector as a scalar multiple and thereby preserved in a ROM without any special consideration. Superposition principles can be used to facilitate additional sources.

For many problems in Electromagnetic Scattering, each element of the source vector has a different frequency dependence. For example, an incident source wave will contact different panels of a scattering target at different moments due to the shape of the target. As a result, for scattering problems, the source vector $E$ (due to

incident electric field) will have frequency dependent elements:

$$\mathbf{Z}(s)\mathbf{J} = \mathbf{E}(s). \tag{5.1}$$

This complicated frequency dependency of the source term $\mathbf{E}(s)$ presents an obstacle to applying the basic MOR methods discussed in the background, let alone full-wave MOR. The right hand side of equation 5.1 is frequency dependent and thus the Krylov-based construction of the Projection Matrix $\mathbf{V}$ would require computation of a different $\mathbf{V}(s)$ at each frequency point, thereby defeating the purpose of the generating a ROM.

## 5.1 MOR for source with complicated frequency dependencies

To benefit from the MOR methods described in chapter 4, one must extend them to apply to problems with frequency dependence in the source term. Several approaches have been devised and developed for this purpose. Each of these approaches depends on superposition principles. Although further study and comparison is a goal for future research, these approaches are briefly outlined in the following subsections.

### 5.1.1 Enriched, larger Krylov Subspace

One idea to facilitate MOR for systems with right-hand-side source terms that have complicated frequency dependencies is to expand the system into the ETAS 2.70 and then to expand the right hand side source vector into its Taylor series representation:

$$\mathbf{E}(s) = [\mathbf{E_0} + (s - s_T)\mathbf{E_1} + (s - s_T)^2 \mathbf{E_2} + \cdots + (s - s_T)^j \mathbf{E_j} + \cdots] \tag{5.2}$$

and then approximate the $\mathbf{E}(s)$ by truncating the series to $n_T$ terms.

Then, it is possible to construct the projection matrix $\mathbf{V}$ to be the orthogonalized

union of $n_T$ separate orthogonal Krylov subspaces each corresponding to a term, $\boldsymbol{E}_j$ ($i = 1, \ldots, n_T$) in the truncated expansion of $\boldsymbol{E}(s)$. Letting $\boldsymbol{X} = (\boldsymbol{\mathcal{Z}}_1^{-1} \boldsymbol{\mathcal{Z}}_2)$ and $\boldsymbol{B}_j = (\boldsymbol{\mathcal{Z}}_1^{-1} \boldsymbol{\mathcal{E}}_j)$, the projection matrix, $\boldsymbol{\mathcal{V}}$, for the ETAS of the system in equation 5.1 would be

$$
\begin{aligned}
\boldsymbol{V} &= [\ \boldsymbol{v_1} \quad \boldsymbol{v_2} \quad \cdots \quad \boldsymbol{v_{\widehat{n}}}\ ],\ \widehat{n} << n_E \\
\boldsymbol{v}_j &\in \left\{ \boldsymbol{B}_0, \boldsymbol{X}\boldsymbol{B}_0, \ldots, \boldsymbol{X}^{\widehat{n}}\boldsymbol{B}_0, \boldsymbol{B}_1, \boldsymbol{X}\boldsymbol{B}_1, \ldots, \boldsymbol{X}^{\widehat{n}}\boldsymbol{B}_1, \ldots, \right. \\
&\qquad \left. \boldsymbol{B}_{n_T-1}, \boldsymbol{X}\boldsymbol{B}_{n_T-1}, \ldots, \boldsymbol{X}^{\widehat{n}}\boldsymbol{B}_{n_T-1} \right\} \\
&|\quad \boldsymbol{V}^T\boldsymbol{V} = \boldsymbol{I}
\end{aligned}
\tag{5.3}
$$

.

This matrix $\boldsymbol{V}$ projects the original system to a $(\widehat{n} \times n_T)$-dimensional subspace, and the projected ROM will match $\widehat{n}$ moments of the exact system solved with a right hand side including at least the first $n_T$ terms in the Taylor series representation of $\boldsymbol{E}(s)$. The difference between this method and that in the previous paragraph is subtle and does not affect the worst case error analysis. The ROM generated, using V to project the system into a lower dimensional subspace, has $n_T \times n_T$ elements, a increase in size (versus $\widehat{n} \times \widehat{n}$) that negates some of the benefits of MOR.

## 5.1.2   Introducing new state variables

An alternative technique to facilitate MOR for systems with right-hand-side source terms that have complicated frequency dependencies is to introduce of $n_T - 1$ new state variables, each of length $n_E$:

$$
\begin{aligned}
\boldsymbol{J}_{n_T} &= \boldsymbol{E_1} + \frac{(s - s_T)}{2}\boldsymbol{J}_{n_T+1}, \\
\boldsymbol{J}_{n_T+1} &= \boldsymbol{E_2} + \frac{(s - s_T)}{3}\boldsymbol{J}_{n_T+2}, \\
&\vdots
\end{aligned}
$$

$$\begin{aligned}
\boldsymbol{J_{2n_T-2}} &= \boldsymbol{E_{n_T}} - 2 + \frac{(s - s_T)}{n_T - 1}\boldsymbol{J}_{2n_T-1}, \\
\boldsymbol{J_{2n_T-1}} &= \boldsymbol{E_{n_T}} - 1
\end{aligned} \tag{5.4}$$

The ETAS system equations can be rewritten with these new state variable definitions,

$$\left[\begin{bmatrix} \boldsymbol{\mathcal{Z}_1} & \boldsymbol{0} & \cdots \\ \boldsymbol{0} & \boldsymbol{I} & \ddots \\ \vdots & \ddots & \ddots \end{bmatrix} + \Delta(s)\begin{bmatrix} -\boldsymbol{\mathcal{Z}_2} & -\boldsymbol{I} & \boldsymbol{0} & \cdots & \boldsymbol{0} \\ \boldsymbol{0} & \boldsymbol{0} & \frac{\boldsymbol{I}}{2} & \ddots & \vdots \\ \boldsymbol{0} & \ddots & \ddots & \ddots & \boldsymbol{0} \\ \vdots & \ddots & \boldsymbol{0} & \boldsymbol{0} & \frac{\boldsymbol{I}}{(n_T-1)} \\ \boldsymbol{0} & \boldsymbol{0} & \boldsymbol{0} & \boldsymbol{0} & \boldsymbol{0} \end{bmatrix}\right]\begin{bmatrix} \boldsymbol{\mathcal{J}_0} \\ \boldsymbol{J_{n_T}} \\ \vdots \\ \boldsymbol{J_{n_T+n_R-2}} \end{bmatrix} = \begin{bmatrix} \boldsymbol{\mathcal{E}_0} \\ \boldsymbol{E_1} \\ \vdots \\ \boldsymbol{E_{n_R-1}} \end{bmatrix},$$
$$\tag{5.5}$$

where $\boldsymbol{\mathcal{Z}_1}$ and $\boldsymbol{\mathcal{Z}_2}$ are defined as in equation 2.71, and the first block row of 5.5 has $(n_T - 1)$ times the number of scalar rows as the rest of the block rows. Note that the right hand size is now frequency-independent. Also, note that it is not necessary to truncate the right hand side at the same order as the ETAS truncation order or, in other words, $n_R$ can be different from $n_T$. Throughout this dissertation, equation 5.5 will be referred to as the Expanded Taylor Approximation system for systems with right-hand-side source vectors that have complicated frequency dependencies (ETASR). Introducing new notation, the ETASR equation 5.5 is rewritten

$$[\boldsymbol{\mathcal{Z}_{R1}} + (s - s_T)\boldsymbol{\mathcal{Z}_{R2}}]\boldsymbol{\mathcal{J}} = \boldsymbol{\mathcal{E}}_R. \tag{5.6}$$

where the $R$ subscript indicates to ETASR quantities corresponding to the appropriate terms in 5.5. The dimensions of ETASR are twice the size of those for the ETAS (assuming $n_T$ is the same for the system matrices and right hand size). Once again, as with the ETAS developed for impedance extraction, the resulting ETASR system of equations has a form similar to equation 2.52: frequency-independent matrices, a frequency-independent right hand side, and a single linear frequency dependency.

Thus, standard MOR procedures are easily applied to the ETASR,

$$[\boldsymbol{V_R}^T\boldsymbol{\mathcal{Z}_{R1}} + (s - s_T)\boldsymbol{\mathcal{Z}_{R2}}]\boldsymbol{V_R}\widehat{\boldsymbol{\mathcal{J}}} = \boldsymbol{V_R}^T\boldsymbol{\mathcal{E}}_R, \qquad (5.7)$$

where the $R$ subscript in the projection matrix, $\boldsymbol{V_R}$, signifies the Krylov subspace is formed with the ETASR system. Using the approach outlined above it is possible to obtain a ROM for systems like the EFIE model ( 2.26) that have a right hand side with complicated frequency dependencies.

### 5.1.3  Creating $n_T$ ROMs

Equation 5.1 is a linear system and both of the previous algorithms, described in sections 5.1.1 and 5.1.2, took advantage of that fact to generate reduced order models. A third approach to developing a ROM for the Electromagnetic scattering equations also takes advantage of linearity to employ principles of superposition to construct a ROM. In this approach, the right hand side is expanded in a truncated Taylor series approximation, as in the previous two methods. However, in this approach, a separate projection matrix $\boldsymbol{V}_j$ and ROM is created for each of the $j = 1, \ldots, n_T$ vector term associated with expansion. In essence, to create the required ROMs, the system will be solved (once or more if multipoint-MOR is used) for each of the $n_T$ vector term associated with expansion. The basic idea is shown below:

$$\boldsymbol{Z}(s)\boldsymbol{J} = \boldsymbol{E}(s) \approx \sum_{j=0}^{n_T} \frac{(s - s_T)^{n_T-1}}{(n_T - 1)!}\boldsymbol{E}_j$$

$$\Rightarrow \quad 1 \text{ idea: let } \boldsymbol{Z}(s)\boldsymbol{J}_j = \boldsymbol{E}_j$$

$$(5.8)$$

Since the $\boldsymbol{E}_j$ terms are frequency independent, MOR can be applied to yield a ROM for each of the $n_T$ $\boldsymbol{E}_j$ terms. The resulting set of $n_T$ ROM's would be solved, and the solutions scaled by the appropriate frequency terms and summed to yield the desired result:

$$\boldsymbol{J}(s) \approx \sum_{j=0}^{n_T} \frac{(s - s_T)^{n_T - 1}}{(n_T - 1)!} \boldsymbol{J}_j \qquad (5.9)$$

The advantage of this approach are that the resulting ROM is only $\widehat{n}n_{MP} \times \widehat{n}n_{MP}$ ($n_{MP}$ refers to the number of "multipoint" Krylov subspaces [18], associated with additional frequency expansion points, whose union forms the basis of the projection matrix $\boldsymbol{V}$), and the resulting ROM allow freedom to choose a different expansion variable for constructing the ETAS equations from the expansion variable used in approximating the right hand side known source vector with a truncated Taylor series. In comparison, the method described in section 5.1.1 generates a ROM that is $n_T \widehat{n}n_{MP} \times n_T \widehat{n}n_{MP}$ by creating a single projection matrix that forces the resulting ROM to match the $\widehat{n}$ moments of the ETAS system at each of the $n_{MP}$ Taylor expansion points (multi-points). While the ROM generated in section 5.1.2 is of size $\widehat{n}n_{MP} \times \widehat{n}n_{MP}$ ROM, the ETASR-based methods require the expansion variable of the left hand side of the ETAS equations to be the same as the expansion variable used to approximate the right hand side incident source field. Thus, the ETASR system may not be optimal when considering techniques for multi-parameter MOR, discussed later in sections 6, which depend on different expansion variables on the left and right hand sides of the equations.

## 5.2 Incorporating SPPF algorithms when source field has complicated frequency dependencies

When the system source vector term has complicated frequency dependencies, the retardation effects can be even more significant than the effects observed in the system matrix, discussed in section 3. For an incident plane wave, traveling along the z-axis, the frequency dependence of this electric field source has the form $\boldsymbol{E}_m = E_m e^{-ikz_m}$ where $z_m$ is the z-axis position coordinate, as measured from the origin, but the $1/r$ factor that appears in the system Green function is absent from the incident source field vector. Therefore, the source vector entries with the worst case phase factors

do not have the smallest amplitudes, as in the system matrix. Therefore, it is even more crucial to develop SPPF algorithms for incident field vectors that have terms with of different frequency dependencies. In addition, yet another consequence of the same observation is that it may be optimal to have separate SPPF parameters for the right-hand side, $\breve{n}_R$ and $\breve{R}_R$, in addition the system matrix SPPF parameters, $\breve{n}$ and $\breve{R}$ or the system matrix.

It is easy to apply the Segregation by Primary Phase Factors Algorithm to the ETAS and ETASR approximations. Similar to the $\boldsymbol{P_j}$, used to select the elements of the $\boldsymbol{\breve{\mathcal{Z}}}(s)$ matrix, the $\boldsymbol{P_{Ei}}$ selector operator is used to select only the elements of the source "remainder" vector $\breve{E}(s)$ corresponding to the phase factor $i\breve{R}_R$ for $i = 1, \ldots, \breve{n}_R$, and each of these terms is summed to yield an accurate approximation to the original source term,

$$\boldsymbol{\breve{\mathcal{Z}}}_R(s)\boldsymbol{\breve{\mathcal{J}}}_R = \sum_{j=0}^{\breve{n}} e^{-ik\breve{R}i}\boldsymbol{P_j}(\boldsymbol{\breve{\mathcal{Z}}}_{R1} + (s - s_T)\boldsymbol{\breve{\mathcal{Z}}}_{R2})\boldsymbol{\breve{\mathcal{J}}}_R = \sum_{j=0}^{\breve{n}_R} e^{-ik\breve{R}_R i}\boldsymbol{P_{Ei}}\boldsymbol{\breve{\mathcal{E}}}_R. \qquad (5.10)$$

Since primary phase factors are segregated and the phase of the entries in the remainder source vector $\breve{E}(s)$ are smaller than $\breve{R}_R$, the truncated Taylor series used in equation 5.10 to approximate $\boldsymbol{E}(s)$ will be far more accurate than just the truncated Taylor series approximation.

## 5.3  Applying SPPF-FMOR when source field is frequency dependent

Combining SPPF-FMOR with the techniques for handling frequency-dependent right-hand-side source terms (ETASR) SPPF-FMOR can be applied to electromagnetic scattering problems with minimal changes:

$$\widehat{\boldsymbol{\breve{\mathcal{Z}}}}_R(s)\widehat{\boldsymbol{\breve{\mathcal{J}}}}_R = \sum_{j=0}^{\breve{n}} e^{-ik\breve{R}i}\boldsymbol{V_R}^T\boldsymbol{P_j}(\boldsymbol{\breve{\mathcal{Z}}}_{R1} + (s - s_T)\boldsymbol{\breve{\mathcal{Z}}}_{R2})\boldsymbol{V_R}\widehat{\boldsymbol{\breve{\mathcal{J}}}}_R$$

$$= \sum_{j=0}^{\check{n}_R} e^{-ik\check{R}_R i} \boldsymbol{V_R}^T \boldsymbol{P_{Ei}} \check{\boldsymbol{\mathcal{E}}}_R, \tag{5.11}$$

using the same FMOR projection matrix $\boldsymbol{V}$, to obtain a ROM. The steps involved are shown in more detail with the full ETASR notation below:

$$\check{\boldsymbol{\mathcal{Z}}}_R(s)\check{\boldsymbol{\mathcal{J}}}_R = \sum_{j=0}^{\check{n}} e^{-ik\check{R}i} \boldsymbol{V_R}^T \boldsymbol{P_j} \left[ \begin{bmatrix} \boldsymbol{\mathcal{Z}}_1 & \boldsymbol{0} & \cdots & \boldsymbol{0} \\ \boldsymbol{0} & \boldsymbol{I} & \boldsymbol{0} & \vdots \\ \vdots & \boldsymbol{0} & \ddots & \boldsymbol{0} \\ \boldsymbol{0} & \cdots & \boldsymbol{0} & \boldsymbol{I} \end{bmatrix} \right.$$

$$\left. + \Delta(s) \begin{bmatrix} -\boldsymbol{\mathcal{Z}}_2 & -\boldsymbol{I} & \boldsymbol{0} & \boldsymbol{0} & \cdots & \boldsymbol{0} \\ \boldsymbol{0} & \boldsymbol{0} & \frac{\boldsymbol{I}}{2} & \boldsymbol{0} & \ddots & \vdots \\ \boldsymbol{0} & \boldsymbol{0} & \boldsymbol{0} & \frac{\boldsymbol{I}}{3} & \ddots & \boldsymbol{0} \\ \boldsymbol{0} & \ddots & \ddots & \ddots & \ddots & \boldsymbol{0} \\ \vdots & \ddots & \boldsymbol{0} & \boldsymbol{0} & \boldsymbol{0} & \frac{\boldsymbol{I}}{(n_T-1)} \\ \boldsymbol{0} & \boldsymbol{0} & \boldsymbol{0} & \boldsymbol{0} & \boldsymbol{0} & \boldsymbol{0} \end{bmatrix} \right] \boldsymbol{V_R}\widehat{\boldsymbol{\mathcal{J}}}_R = \boldsymbol{V_R}^T \begin{bmatrix} \boldsymbol{\mathcal{E}}_0 \\ \boldsymbol{E}_1 \\ \boldsymbol{E}_2 \\ \vdots \\ \boldsymbol{E}_{n_T-1} \end{bmatrix}. \tag{5.12}$$

The choice of utilizing the same projection matrices to reduce the SPPF-ETAS system as would be used for the ETAS system is not a heuristic, because, although the SPPF Taylor series expansion has different derivative terms, that is only because the primary phase factors are segregated. Therefore, the ETAS projection matrices are still appropriate to match Taylor expansion terms or moments of the original system.

Incorporating the $\boldsymbol{P_j}$ and $\boldsymbol{P_{Ej}}$ operators into the matrix and vector indices yields

$$\widehat{\check{\boldsymbol{\mathcal{Z}}}}_R(s)\widehat{\check{\boldsymbol{\mathcal{J}}}}_R = \sum_{j=0}^{\check{n}} e^{-ik\check{R}i} (\widehat{\check{\boldsymbol{\mathcal{Z}}}}_{R1i} + (s - s_T)\widehat{\check{\boldsymbol{\mathcal{Z}}}}_{R2i})\widehat{\check{\boldsymbol{\mathcal{J}}}}_R$$

$$= \sum_{j=0}^{\check{n}_R} e^{-ik\check{R}_R j} \widehat{\check{\boldsymbol{\mathcal{E}}}}_{Rj}. \tag{5.13}$$

Since superposition principles apply to the right hand side for all the algorithms discussed here, as opposed to the system matrix that must be inverted, the motivation to employ the SPPF algorithm to the right hand side is not as obvious. For frequency dependent right hand sides, one could disregard SPPF concepts and expand the right hand side into the necessary (very large) number of terms, $n_{TE}$, to construct an accurate approximation, but generate a projection matrix using only a smaller number of those terms in order to achieve efficiency, and use some sort of multipoint MOR algorithm to capture a wider band of frequencies, as necessary. However, even if the number of overall terms was comparable to the SPPF truncated Taylor approximation to the right hand side, the terms would not be sparse as they are for SPPF. Therefore, such a method would require more computation. In addition to the sparsity, for certain geometries, such as smaller objects separated by distances greater than a wavelength, SPPF enables accurate truncated Taylor approximation with a far smaller number of total terms, which in turn leads to far less computation in the MOR procedures and analysis. However, as mentioned earlier, we hope to address and examine these issues in greater detail during future research.

## 5.4   Example problems

Three example structures were chosen to demonstrate the utility of SPPF-FMOR for Electromagnetic Scattering Computations.

- Long thin wire

- Another long thin wire

- 4 spheres in a row

For all 3 example structures, the source is a plane wave traveling along the axis of symmetry, exciting the scattering targets between frequencies of 80 MHz and 800 MHz. The plane wave has non-zero electric field in the x direction and zero electric field in the y and z directions.
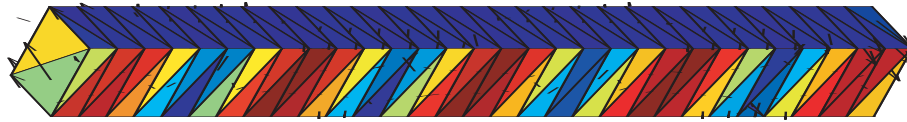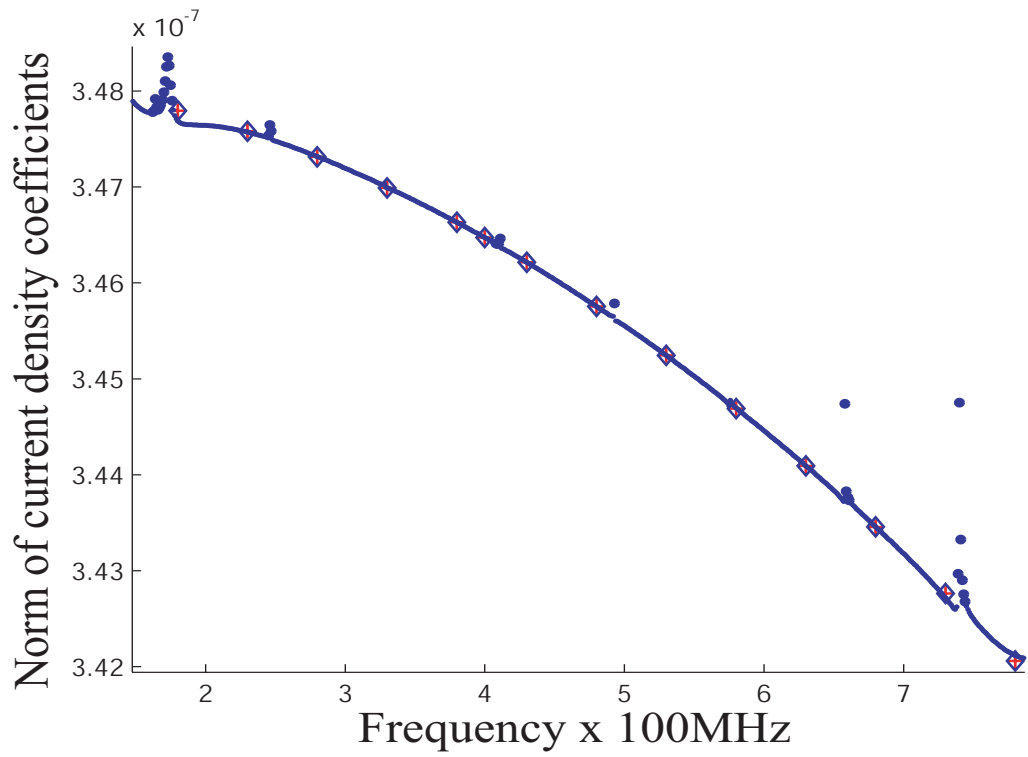
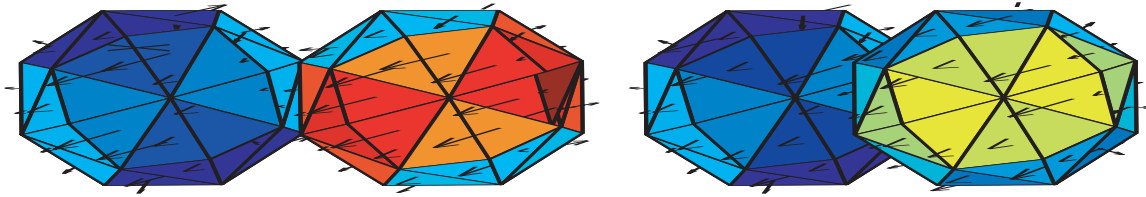(e) Long thin wire. Over the frequency range, the wire has length $.3\lambda$ to $3\lambda$.
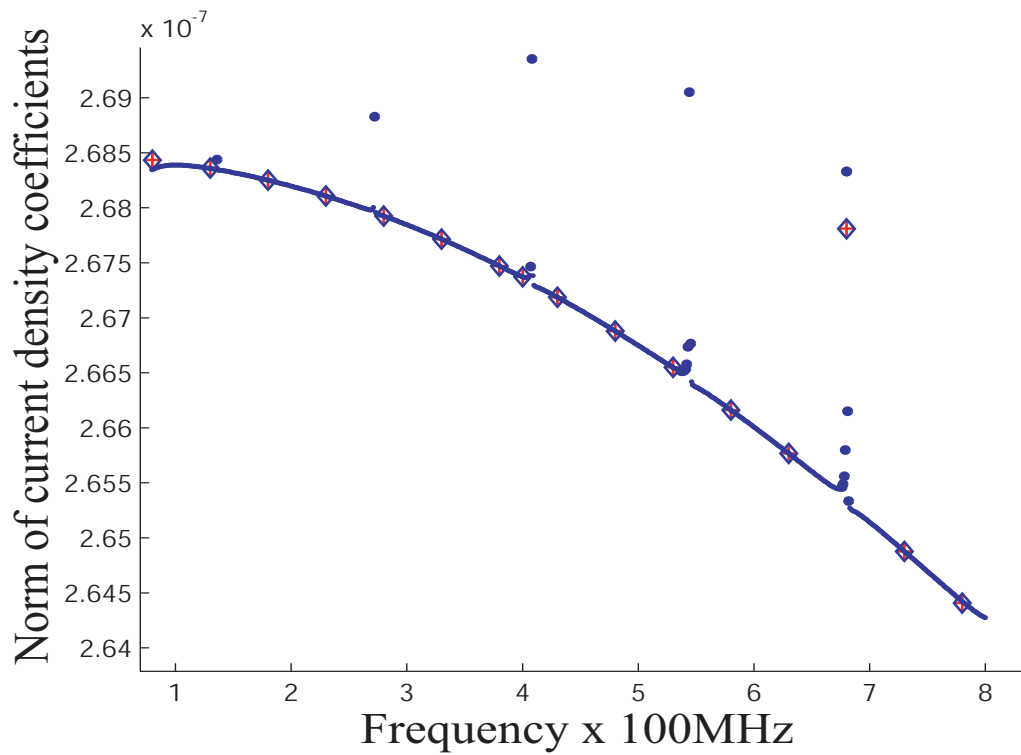


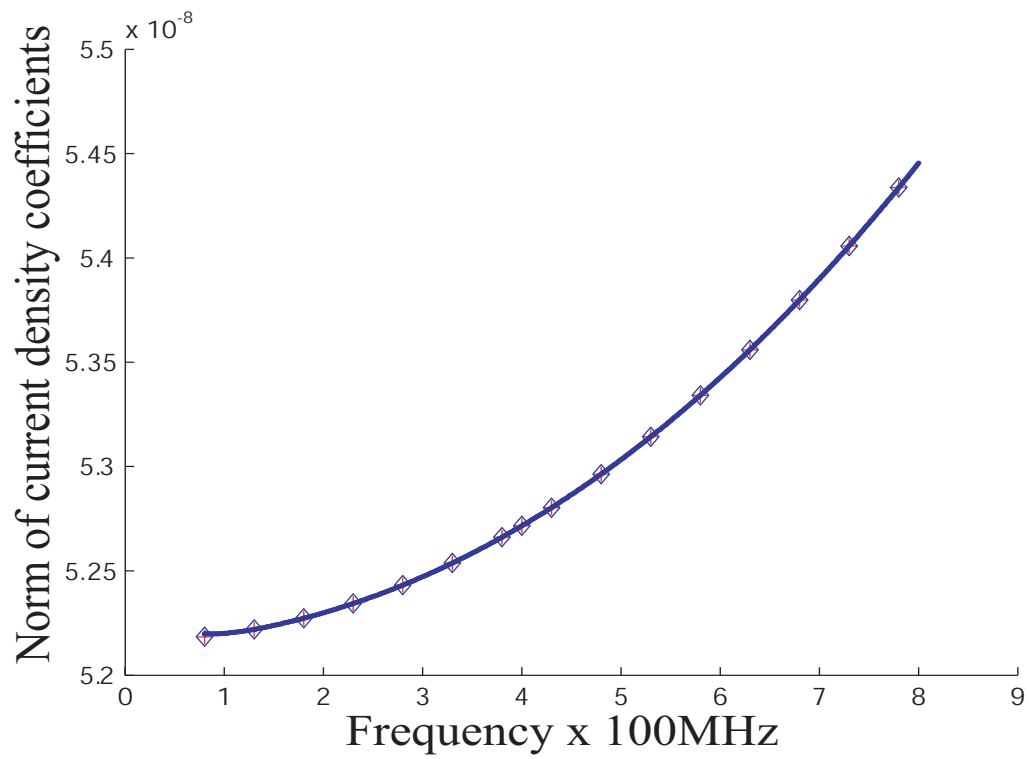(f) Norm of the vector of edge current density coefficients. Note the sharp resonances.
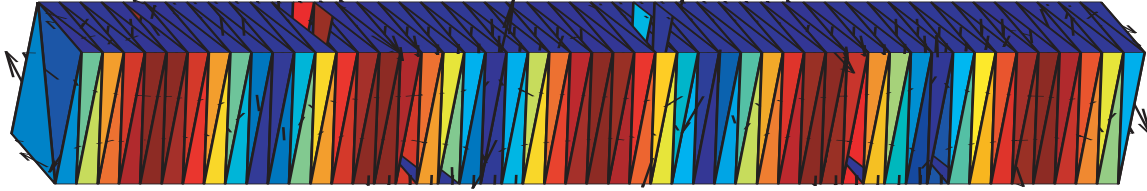
(g) Long thin wire. Over the frequency range, the wire has length $.5\lambda$ to $5\lambda$.



(h) Norm of the vector of edge current density coefficients. Note the sharp resonances.

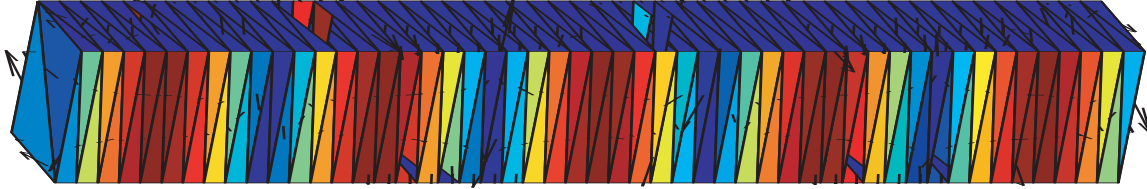(i) 4 Spheres in a row. Over the frequency range, each sphere has diameter of $.01\lambda$ to $.1\lambda$ and the row has length of $.6\lambda$ to $6\lambda$)



(j) Norm of the vector of edge current density coefficients.

The figures in this section, (5.4,5.4, and 5.4), show the three structures and plots of the norm of the vector of edge current density coefficients over the desired frequency range. Model Order Reduction is used to plot the intermediary points since it would be too time consuming to solve the original system at each point. Note the sharp resonances of the long wire structures.

## 5.5    Results for SPPF-FMOR applied to EM Scattering analysis

For each of the structure discussed in the previous section, the relative error is compared between ROMs generated by SPPF-MOR and the FMOR-ETAS methods in this section. Both models incorporate $n_T = 8$ Taylor expansion terms with the expansion point at 400 MHz and two additional multipoint at approximately 250 MHz and 600 MHz. Figure 5.5 demonstrates 100 to 1000 improvement for SPPF-MOR ROM accuracy vs the ROM generated by FMOR-ETAS methods, over the entire frequency range. Figure 5.5 demonstrates 10,000 to 1,000,000 improvement for SPPF-MOR ROM accuracy vs the ROM generated by FMOR-ETAS methods, over the entire frequency range. These results strongly support the notion that SPPF-FMOR will be of great benefit to EM scattering applications.

The error plots show great potential for the SPPF algorithm to meet the full-wave challenge, but the long wire plot does also raise some concern, mainly the lack of improvement due to additional multipoint frequency expansion points. There are no "dips" in the graph and error rises very rapidly away from the central Taylor Expansion point. From one point of view, the graph highlights how poorly FMOR-ETAS performs in approximating the original system between 80 MHz and 800 MHz, rather than how well SPPF-MOR performs. Furthermore, while performance of the SPPF-FMOR ROM is quite good, over most of the frequency range, just outside the edges of the desired 80 MHz to 800 MHz frequency ranges the error is almost 100% even though it is much lower than the alternative ROM. This suggests that the
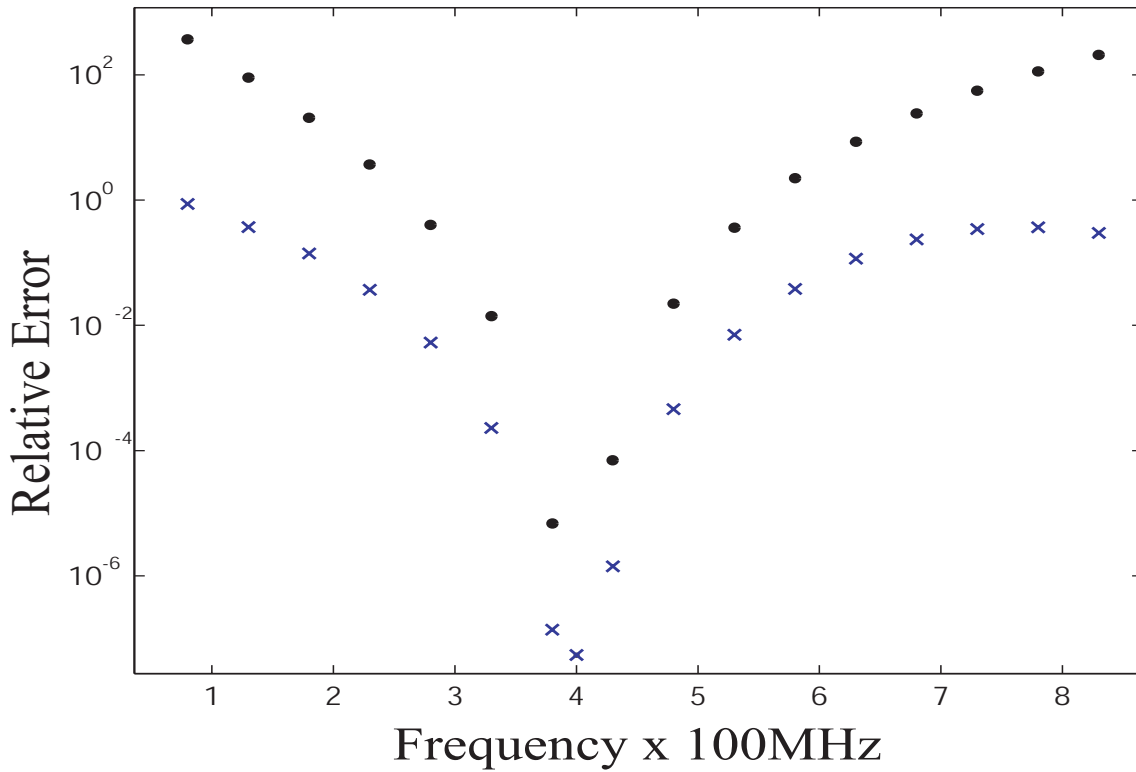
(k) Long thin wire. Over the frequency range, the wire has length .5$\lambda$ to 5$\lambda$.
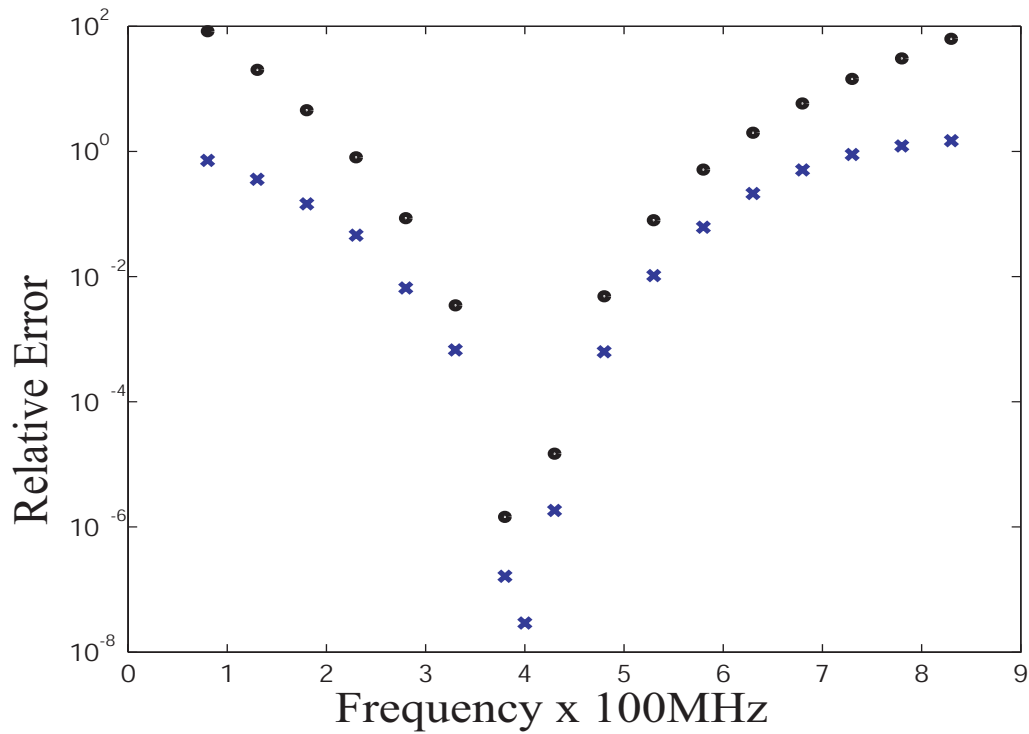


(l) This figure compares the Log scale plot of Relative Error of the Current coefficients computed by the new SPPF-FMOR (x) algorithm and by the previous ETAS-FMOR (.) methods plotted versus frequency. The SPPF-FMOR ROM achieves 10 to 100 times better accuracy than the ROM produced by the previous ETAS-FMOR method, over much of the frequency range.
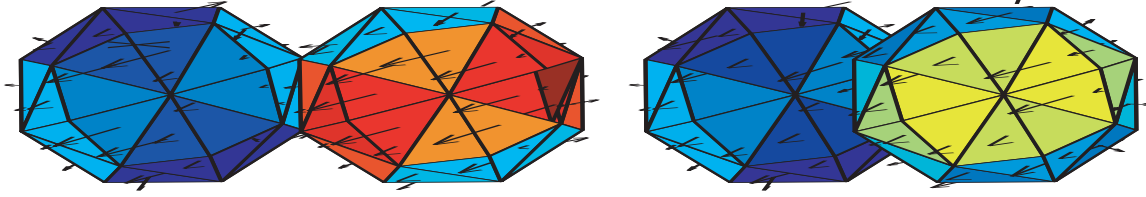
(m) 4 Spheres in a row. Over the frequency range, each sphere has diameter of $.01\lambda$ to $.1\lambda$ and the row has length of $.6\lambda$ to $6\lambda$)



(n) This figure compares the Log scale plot of Relative Error of the Current coefficients computed by the new SPPF-FMOR (x) algorithm and by the previous ETAS-FMOR (.) methods plotted versus frequency. The SPPF-FMOR ROM achieves 100 to 1,000 times better accuracy than the ROM produced by ETAS-FMOR over much of the frequency range.

additional expansion points are adding little to the ROM performance.

Examining a slightly shorter wire $.3\lambda$ to $3\lambda$, figure 5.5 compares log relative error performance of the FMOR-ETAS and SPPF-FMOR ROMs. The results are disappointing, showing only five to ten times improvement of the new algorithm and are not accurate at the edge of the desired frequency range. These results suggest that developing a multipoint SPPF-FMOR algorithm might be highly advantageous.

In summary, the results of this section were extremely convincing in two respects: First, that SPPF-FMOR has a lot of potential to improve the bandwidth of ROM accuracy. Second, that to realize that potential, it is crucial to study multipoint MOR and develop new techniques for multipoint full-wave MOR in the context of the SPPF-FMOR algorithm.

(o) Long thin wire. Over the frequency range, the wire has length .3λ to 3λ.
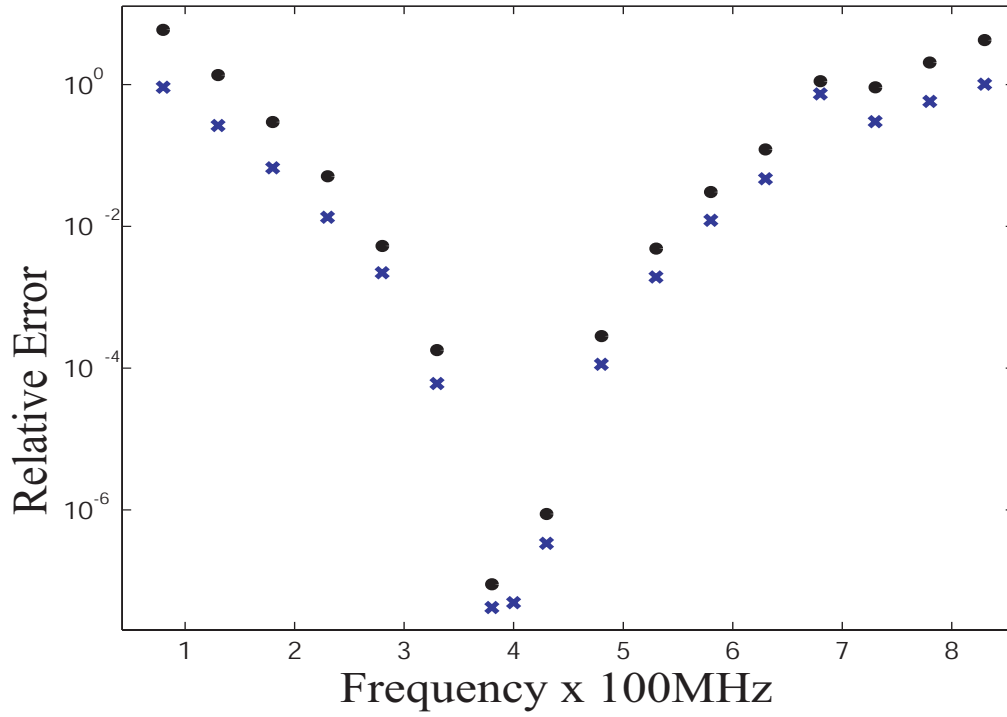


(p) This figure compares the Log scale plot of Relative Error of the Current coefficients computed by the new SPPF-FMOR (x) algorithm and by the previous ETAS-FMOR (.) methods plotted versus frequency. The SPPF-FMOR ROM achieves up to 10 times better accuracy than the ROM produced by ETAS-FMOR, over much of the frequency range.

# Chapter 6

# Multipoint-MOR for Full-wave Analysis

Figure 6-1(r) demonstrates why existing multi-point techniques are inadequate to improve full-wave ETAS-based FMOR. Figure 6-1(r) plots the log of the error of the current density coefficients for the ETAS($\circ$), ETAS-FMOR ROM (.), SPPF-ETAS ($\diamond$), and SPPF-FMOR ($\bullet$). The ETAS-FMOR ROM points are all within the circles, everywhere on the plot. Both ROMs are computed with two additional ETAS based multipoints at 180 MHz and 680 MHz, yet there are no "dips" corresponding to the additional expansion points, indicating that the inclusion of these additional terms in the projection matrix contributes little to nothing to improve the range of accuracy of the ROMs. The ETAS-FMOR ROM matches the ETAS exactly, indicating that increasing the ROM size will not improve accuracy and that only increasing $n_T$, the truncation order of the ETAS can improve the accuracy! The SPPF-FMOR ROM barely beats the ETAS-FMOR ROM and ETAS by hardly a factor of ten but also shows no improvement due to the multi-points evaluated from the original ETAS.

The SPPF-ETAS accuracy is very high over the entire frequency range, suggesting that there is much potential in this algorithm, if only MOR methods, such as multi-point MOR, could take advantage of it. It is unclear how MOR theory for multi-point moment-matching, described in section 2.7.3, would be extended for full-wave MOR. Multi-point moment-matching was not considered in [35] or [37]. Figure 6-1(r)

(q) Long thin wire: Over the frequency range, the wire has length .3λ to 3λ.
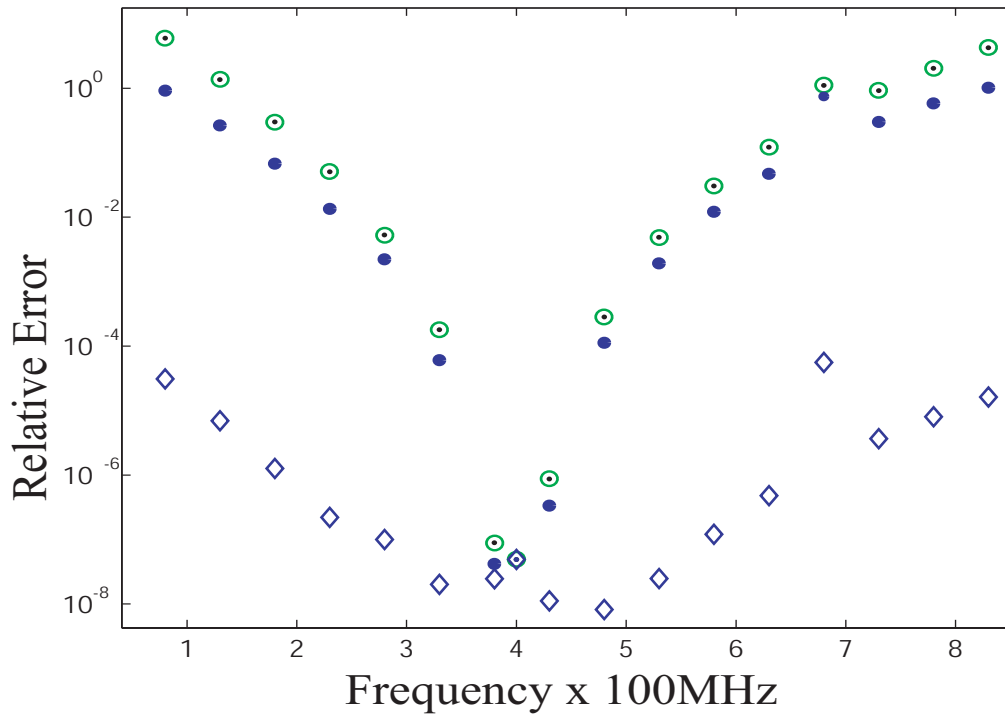


(r) Log plot of relative error in current computed from: ETAS(∘), SPPF-ETAS(◇), ETAS-FMOR(.), SPPF-FMOR(•). This figure plots the log of the relative error of the ETAS model (∘) for the EM-large long thin wire in a full-wave frequency regime. The results illustrate that the ETAS Model (∘) with $n_T = 6$ has a narrow band of accuracy around the expansion point at 400 MHz. The dashed lines demark a zone, 250 to 560 MHz, with relative error < .1. The ETAS-MOR ROM (.) matches the ETAS model over the entire frequency range. Each '.' is within a '∘' !

demonstrates that the SPPF-FMOR ROM has a wider band of accuracy than the FMOR-ETAS ROM, and the other SPPF results in previous chapters were also much better than the ETAS-FMOR, so why should one worry about multi-point MOR? First of all, the SPPF-FMOR ROM errors were unacceptable (reaching almost 100%) towards the edges of the desired frequencies ranges. Second, the results of figure 6-1(r), for the same long wire, demonstrates that the SPPF-ETAS model ($n_T = 6$) is far more accurate over the entire desired frequency range and illustrates the full "potential" of SPPF. In other words, while the SPPF-ETAS model is approximately 1,000,000 times more accurate over much of the frequency range, the the multi-point SPPF-FMOR ROM is no-where near that accurate. Thus, SPPF-FMOR without some sort of multi-point scheme would not "tap into" the full potential of SPPF!

The ROM results computed by the SPPF algorithm are clearly an improvement, but they do not show much benefit due to the additional points added via multi-point MOR and nowhere near the improvement that the SPPF-ETAS is capable of. Since the results of the previous chapter demonstrate that the poor performance of multi-point MOR carries over to SPPF-FMOR ROMs as well, those results help establish the fact that the ETAS model is the limiting factor for ROM accuracy, in both SPPF-FMOR and ETAS-FMOR algorithms. The last paragraph of section 4.5 hinted at the importance of the Projection Matrix $V$ and questioned the use of the ETAS-based $V$ to reduced the SPPF-ETAS, given the ETAS model's narrow band of accuracy. However, there are two major motivations to choose an ETAS-based $V$: it is easy to compute and it is unclear how to use the SPPF-ETAS model itself to compute a projection matrix.

As described in section 3.2 and [18], Multi-point MOR applied to the ETAS forces the resulting ROM to match the ETAS at the additional expansion points. Due to the double Taylor Approximation, the best that the ETAS-based multi-point ROM can do is match the ETAS results exactly over the entire range. Since additional expansion points are chosen to extend the range of accuracy for the resulting ROM, it is desirable to choose them outside the range of accuracy of the ETAS (which approximates the system at the original expansion point), but in that case the ETAS

115

values will not be accurate at any desirable expansion points! Therefore, since the Krylov subspaces contributed by the additional expansion points do not seem to expand the span of the approximating subspace, $V$, in directions that are closer to the exact solutions at the additional frequency points, this first, cursory consideration of the matter would suggest that results computed by the SPPF-FMOR ROM should only be better than the ETAS or ETAS-based ROM because of "luck". This raises an interesting observation and question: Why do the SPPF-FMOR ROM results beat the ETAS?

The answer is easiest understood by examining what the ROMs retain from the original model. The ETAS-FMOR ROMs retain the directions in the ETAS corresponding to the q-dimensional Krylov subspace generated from the $n_T$-order ETAS evaluated at the additional points. The SPPF-FMOR ROMs retain the directions in the SPPF-ETAS corresponding to the q-dimensional Krylov subspace generated from the $n_T$-order ETAS. Thus, since the SPPF-ETAS contains the full-contribution of the primary phase components and only approximates the remainder phase components, the directions in the q-dimensional Krylov subspace generated from the $n_T$-order ETAS may project more of the original system's first q moments into the SPPF-FMOR ROM than the ETAS-FMOR ROM at the additional expansion points. This observation is very important and may serve as a little hint to possible approaches to obtain a new SPPF-based multi-point MOR algorithm with true multi-point moment matching!

The example problems in section 4.6 and section 5.5 demonstrated that SPPF-FMOR can generate ROMs which have a much wider band of accuracy than ROMs generated by the pre-existing FMOR-ETAS methods. However, it would be nice to find a way to extend the frequency range for which SPPF-ROMs are accurate further and tapping the full potential revealed in the accuracy of the SPPPF-ETAS by taking better advantage of multi-point MOR techniques. The goal for developing a new multi-point algorithm is to find a compromise that preserves easy construction of $V$, improves accuracy of the ROM significantly with addition of new expansion points, and takes advantage of the accuracy improvements of SPPF-FMOR. The next

sections will present new algorithms for multi-point moment matching in the context of SPPF-FMOR.

## 6.1 Multi-point SPPF-FMOR using multiple source expansion points

Since the algorithm for multi-point MOR, described in this section, uses multiple source or right-hand-side (RHS) expansion points and is appropriate for full-wave MOR with SPPF-ETAS, we will refer to it as RHSMP-FMOR. The RHSMP-FMOR algorithm for multi-point SPPF-FMOR was developed based on a philosophy of incrementalism. At the onset, the goal was to merely improve the both the projection matrix and the resulting SPPF-ROMs with minimal additional computational and implementation costs. The research, for chapter 5, to develop full-wave MOR algorithms for problems with frequency-dependent source vectors, yielded an important observation: For a source plane wave, a source vector entry $\boldsymbol{E}_m(s)$ has the form of a sinusoidal function $e^{ikz_m}$ as opposed to the Helmholtz Green's function, $\frac{e^{ikr_{mn}}}{r_{mn}}$ form of a system matrix $\boldsymbol{Z}_{mn}(s)$. This difference is significant because it indicates the source vector plays a greater role in determining error-efficiency tradeoffs for developing ETAS-based models, since the $\boldsymbol{Z}_{mn}(s)$ ETAS terms with the worst phase error correspond to the largest $r_{mn}$ and are scaled by $1/r_{mn}$ which decreases their influence somewhat.

Taking advantage of this interesting observation, RHSMP-FMOR makes choices to compromise in the direction of efficiency. RHSMP-FMOR extends the projection matrix $\boldsymbol{V}$ by adding terms corresponding to multiple right-hand-side source expansion points, but the Krylov matrix is formed just by using the ETAS evaluated at the additional expansion points. The justification for opting for this "incremental improvement" of just using exact source vectors but not computing the exact system matrix used to form the Krylov matrix for the additional expansion points, is the savings of not computing and storing all the terms in the expansion of $\boldsymbol{Z}(s)$ at

additional expansion points. The steps of the RHSMP-FMOR algorithm are:

- Choose additional frequency expansion points $s_{MPl}$ for $l = 1, \cdots, n_{MP}$

- Let $\boldsymbol{X}_0 = \boldsymbol{\mathcal{Z}_1}(s_T)^{-1}\boldsymbol{\mathcal{Z}_2}(s_T)$

- Let $\boldsymbol{X}_l = [\boldsymbol{\mathcal{Z}_1}(s_T) - (s_{MPl} - s_T)\boldsymbol{\mathcal{Z}_2}(s_T)]^{-1}\boldsymbol{\mathcal{Z}_2}(s_T)$ for $l = 1, \cdots, n_{MP}$

- Let $\boldsymbol{B}_{0,j} = E_j(s_T)$ for $j = 1, \cdots, n_T$

- Let $\boldsymbol{B}_{l,j} = E_j(s_{MPl})$ for $j = 1, \cdots, n_T$ and $l = 1, \cdots, n_{MP}$

Using the choices and notation above, the RHSMP-FMOR projection matrix is then constructed very similar to the previous projection matrices, except for the inclusion of Krylov subspaces at additional expansion points:

$$
\begin{aligned}
\boldsymbol{V} &= \begin{bmatrix} \boldsymbol{v_1} & \boldsymbol{v_2} & \cdots & \boldsymbol{v_q} \end{bmatrix}, \quad q << n_E \\
\boldsymbol{v_j} &\in \Big\{ \boldsymbol{B}_{0,0}, \boldsymbol{X}_T\boldsymbol{B}_{0,0}, \boldsymbol{X}_T^2\boldsymbol{B}_{0,0}, \dots \boldsymbol{X}_0^{q-1}\boldsymbol{B}_{0,0}, \dots, \\
&\qquad \boldsymbol{B}_{0,(q-1)}, \boldsymbol{X}_0\boldsymbol{B}_{0,(q-1)}, \boldsymbol{X}_0^2\boldsymbol{B}_{0,(q-1)}, \dots, \boldsymbol{X}_0^{q-1}\boldsymbol{B}_{0,(q-1)}, \\
&\qquad \boldsymbol{B}_{1,0}, \boldsymbol{X}_1\boldsymbol{B}_{1,0}, \boldsymbol{X}_1^2\boldsymbol{B}_{1,0}, \dots, \boldsymbol{X}_1^{q-1}\boldsymbol{B}_{1,0}, \dots, \\
&\qquad \boldsymbol{B}_{1,(q-1)}, \boldsymbol{X}_1\boldsymbol{B}_{1,(q-1)}, \boldsymbol{X}_1^2\boldsymbol{B}_{1,(q-1)}, \dots, \boldsymbol{X}_1^{q-1}\boldsymbol{B}_{1,(q-1)}, \dots, \\
&\qquad \boldsymbol{B}_{n_{MP},(q-1)}, \boldsymbol{X}_{n_{MP}}\boldsymbol{B}_{n_{MP},(q-1)}, \boldsymbol{X}_{n_{MP}}^2\boldsymbol{B}_{n_{MP},(q-1)}, \dots \boldsymbol{X}_{n_{MP}}^{q-1}\boldsymbol{B}_{n_{MP},(q-1)} \Big\} \\
&| \quad \boldsymbol{V}^T\boldsymbol{V} = \boldsymbol{I}
\end{aligned}
\tag{6.1}
$$

## 6.1.1 Results for SPPF-RHSMP-FMOR applied to EM Scattering analysis

Three example structures were chosen to highlight the utility of SPPF-RHSMP-FMOR for Electromagnetic Scattering Computations. To demonstrate the results of this section, the several examples are analyzed in the frequency range of 80 MHz to 800 MHz:

- Long thin wire with length of $.3\lambda$ to $3\lambda$

- 4 spheres in a row

- Another long thin wire with length of length of $.5\lambda$ to $5\lambda$

For all the example structures, the source is a plane wave traveling along the axis of symmetry, exciting the scattering targets, and the relative error is compared between ROMs generated by SPPF-RHSMP-MOR and the FMOR-ETAS methods. Both ROMs incorporate $n_T = 6$ Taylor expansion terms with the expansion point at 400 MHz and two additional multi-point at approximately 250 MHz and 600 MHz. The results will show the great improvement, in some cases 100,000 to 1,000,000 times better accuracy, relative to the results in the previous chapter due to the SPPF-RHSMP-FMOR algorithm.

The results[1] of applying the RHSMP-FMOR algorithm with SPPF-FMOR (RHSMP SPPF-FMOR) to the long, thin wire example of figure 6-1(s) are quite good and much improved over the multi-point MOR results based on the SPPF-ETAS in the previous chapter. As figure 6-1(t) demonstrates, SPPF-RHSMP-FMOR is 1000 times more accurate over most of the frequency range than multi-point MOR based on the ETAS (ETAS-MP-FMOR).

Figure 6-1(v) shows the results of applying the SPPF-RHSMP-FMOR to the longer ($.5\lambda$ to $5$ $5\lambda$, electromagnetically larger), thin wire example of figure 6-1(u). The accuracy of SPPF-MRHS-FMOR also is significantly better than multi-point MOR based on the ETAS (ETAS-MP-FMOR) and much improved over the multi-point MOR results based on the SPPF-ETAS in the previous chapter.

Figure 6-1(v) demonstrates that the RHSMP SPPF-FMOR ROM achieved 1,000 to 10,000 times better accuracy than the multi-point FMOR-ETAS ROM over much of the frequency range. Since, we saw in 8.2 of section 5.5 that SPPF-FMOR with ETAS-based multi-point achieved 10-100 times accuracy improvement, it is obvious RHSMP has helped tremendously (almost 100 times or two decades better) at negligible additional computational or storage costs.
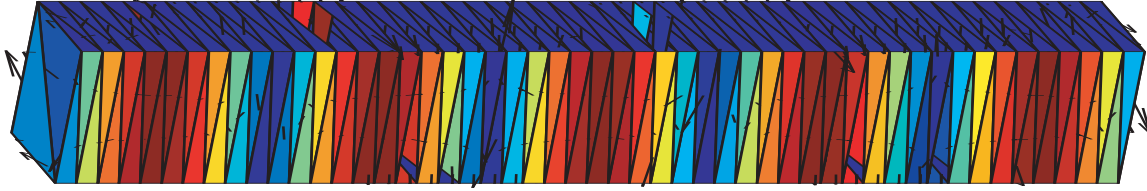
---

[1]All ETAS or SPPF-ETAS models include $n_T = 6$ terms, in the results.
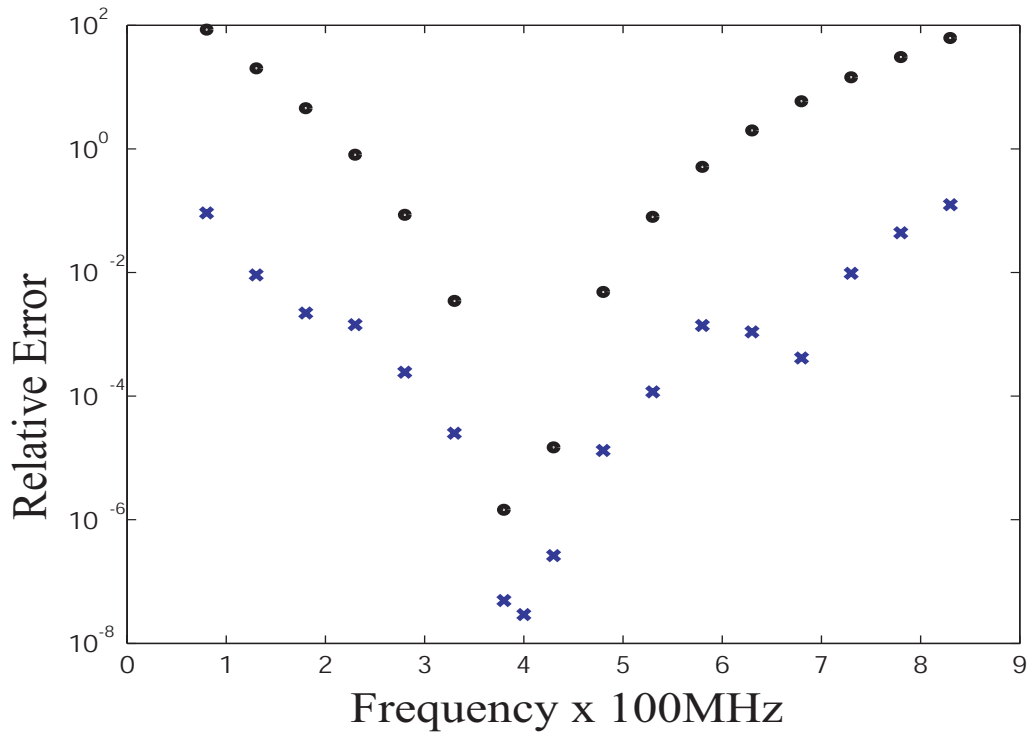
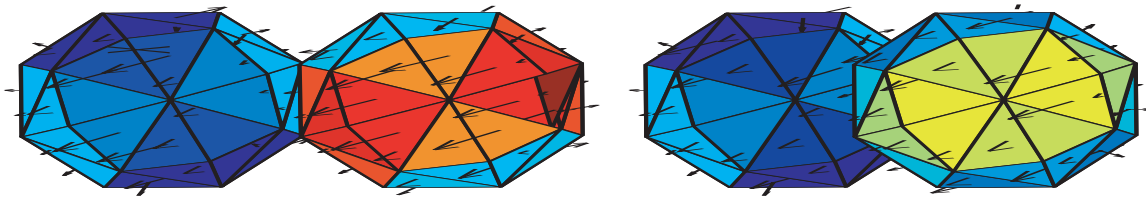(s) Long thin wire. Over the frequency range, the wire has length .3λ to 3λ.
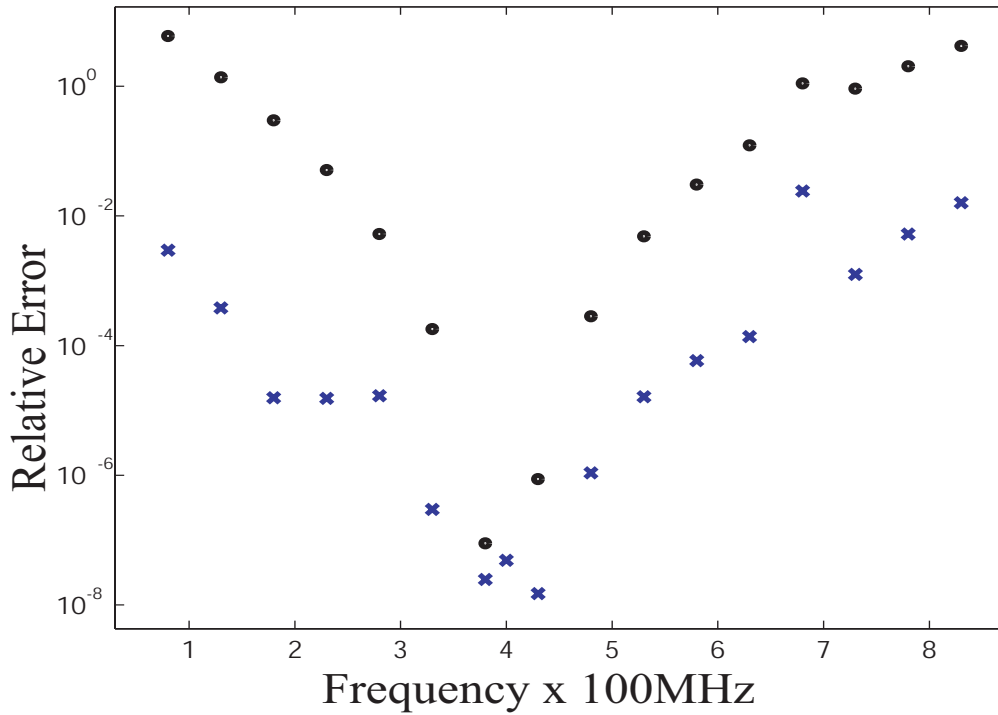


(t) This figure compares the Log scale plot of Relative Error of the Current coefficients computed by the new SPPF-FMOR (x) algorithm and by the previous ETAS-FMOR (.) methods plotted versus frequency. Using the new RHSMP multipoint MOR, the SPPF-FMOR ROM achieves almost 10,000 time better accuracy than the ROM produced by ETAS-FMOR, over much of the frequency range!

(u) Long thin wire. Over the frequency range, the wire has length $.5\lambda$ to $5\lambda$.



(v) This figure compares the Log scale plot of Relative Error of the Current coefficients computed by the new SPPF-FMOR (x) algorithm and by the previous ETAS-FMOR (.) methods plotted versus frequency. Using the new RHSMP multipoint MOR, the SPPF-FMOR ROM achieves almost 1,000 time better accuracy than the ROM produced by ETAS-FMOR, over much of the frequency range!

Examining the final example, the reader will see that the results of applying the RHSMP-FMOR algorithm with SPPF-FMOR (RHSMP SPPF-FMOR) to the row of spheres example of figure 6-1(w) are outstanding!!! Figure 6-1(x) demonstrates *100,000 to 1,000,000 times* improvement for SPPF-RHSMP-FMOR ROM accuracy vs the ROM generated by FMOR-ETAS methods, over much of the frequency range.

In summary, the new SPPF-RHSMP-FMOR algorithm for SPPF-based multi-point full-wave model order reduction has demonstrated the potential to generate ROMs that accurately characterize the EM scattering behavior of the original scattering target over an entire desired frequency range. This algorithm enables the user to include additional expansion points into the projection matrix that will increase the frequency range of the ROM's accuracy.

## 6.2 Multi-point SPPF-FMOR using multiple source expansion points

There is one key observation from figure 6-1(r), which is that the SPPF-ETAS is very accurate over the entire range. From this observation, the key to multi-point for SPPF can be deduced. If SPPF-ETAS is a very accurate approximation, then it should be equal to ETAS expanded at any point rather than just the selected central expansion point! Thus, if new ETAS are constructed at new multi-points and insert Krylov subspaces, based on those additional ETAS, into the projection matrix, more of the SPPF-ETAS (expanded around the main expansion point) moments will be projected into the approximate ROM and the solution subspace will be closer to the original unknown! This idea has been implemented but there has been insufficient data at the time of writing this dissertation to include here.

(w) 4 Spheres in a row. Over the frequency range, the spheres each have diameter of $.01\lambda$ to $.1\lambda$ and the row has length of $.6\lambda$ to $6\lambda$
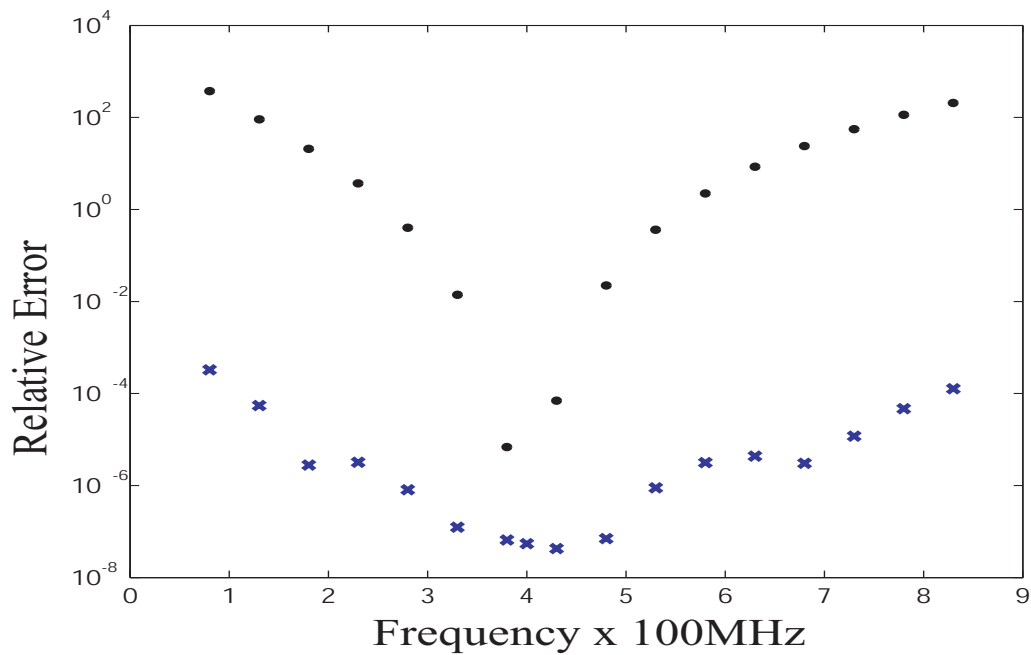


(x) This figure compares the Log scale plot of Relative Error of the Current coefficients computed by the new SPPF-FMOR (x) algorithm and by the previous ETAS-FMOR (.) methods plotted versus frequency. Using the new RHSMP multipoint MOR, the SPPF-FMOR ROM achieves almost 1,000,000 time better accuracy than the ROM produced by ETAS-FMOR, over much of the frequency range!!!

# Chapter 7

# Full-wave Model Order Reduction for problems with output selection vectors that have complicated frequency-dependencies

## 7.1 SPPF for Output Selection Vectors with complicated frequency dependencies

The desired output for a scattering solver is some user-specified function of the computed induced scattering current density coefficients. Examples of outputs that users frequently desire for scattering analysis of a target include radar cross-sections or components of the scattered electric or magnetic field at some observation point. Computation of the desired output typically involves computing the scattered fields at an observation point outside the volume and surface of the scattering target. This chapter briefly presents the steps necessary to incorporate SPPF when the output selection vector $\boldsymbol{C}(s)$ has complicated frequency dependencies:

$$y(s) = \boldsymbol{C}(s)^T \boldsymbol{J}(s). \tag{7.1}$$

In equation 7.1, the desired scattering output $y(s)$ is a weighted sum of the induced current densities, and the weighting has the phase $e^{ikr_m}$, but $r_m$ differs for each element $\boldsymbol{C}_m$ to be multiplied by the corresponding element $\boldsymbol{J}_m(s)$. The output selection vector, $\boldsymbol{C}(s)$, is used perform the weighted summation of the edge current densities to compute the desired output.

This challenge seems very similar to the difficulty posed by complicated frequency dependencies in the right hand side source vector, but it is even greater. As before, SPPF can be applied in order to facilitate truncated Taylor approximation, but the challenge for truncated Taylor approximation of $\boldsymbol{C}(s)$ is compounded by the fact that the observation point of interest can be miles away from the geometry for certain problems[1], resulting in $r_m$ values that are many thousands of meters. Thus, even quasistatic analysis of structures that are not "electromagnetically large" can pose a serious difficult with respect to application of traditional full-wave MOR algorithms.

Therefore, a new parameter $R_{SC}$, the distance between the observation point and the centroid of the scattering geometry, is introduced in order to extend the SPPF algorithms for use with frequency dependent output selection vectors. Since the output selector phase factors are of different magnitude than the system matrix entries, it follows to reason that it will be beneficial to have separate SPPF parameters for the right-hand side, $\breve{n}_C$ and $\breve{R}_C$. Thus the output selection vector interaction distances are decomposed in the following way:

$$r_m = R_{SC} + \breve{R}_C l_m + d_m \tag{7.2}$$

So, in the case of output selection vectors with complicated frequency dependencies , Segregation by Primary Phase Factors for output selection vectors (SPPF-OSV) now involves three parameters, $\breve{n}_C$, $\breve{R}_C$, and $R_{SC}$, instead of just the two system matrix SPPF parameters, $\breve{n}$ and $\breve{R}$ and the two right-hand side SPPF parameters $\breve{n}_R$ and $\breve{R}_R$. Figure 7-1 illustrates the steps for applying Segregation into Primary Phase Factors to the output selection vector used to compute the output,

---

[1] Surveillance airplanes will attempt to use radar to detect and identify ground vehicle targets from great distances, often many miles from the target
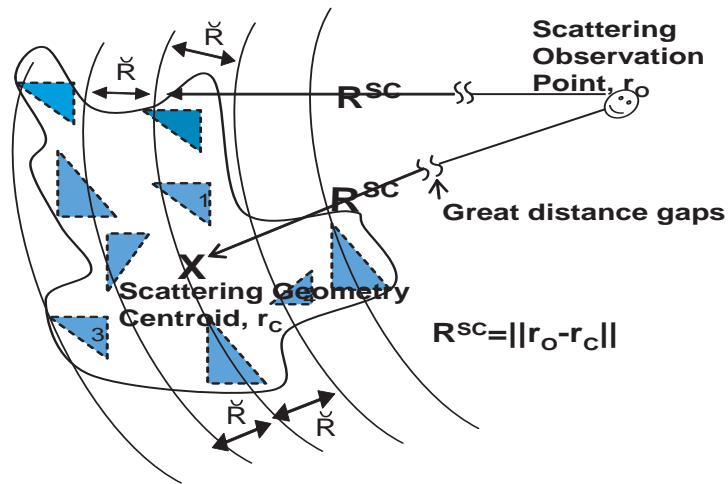
Figure 7-1: Segregating of $\boldsymbol{\mathcal{C}}(s)$, the output selection vector, by Primary Phase Factors (SPPF-OSV): Observe how $r$, the distance between the observation point and points on the geometry that are in the $mth$ output selection vector SPPF bin, is segregated as follows: $r = R_{SC} + m\breve{R}_C + d$, where $m$ can be positive OR negative integers. Panel 1 is in bin 0, Panel 2 is bin 1, and Panel 3 is bin -1.

$$y = e^{-ikR\breve{}_{SC}} \sum_{j=0}^{n\breve{}_C} e^{-ikR\breve{}_{Cj}} \boldsymbol{P_{Cj}} [\breve{\boldsymbol{\mathcal{C}}}(s)]^T \breve{\boldsymbol{\mathcal{J}}}(s). \tag{7.3}$$

Figure 7-1 illustrates that bin 0 has a primary phase factor of 1 , bin 1 has a primary phase factor of $e^{-ikR\breve{}_C}$ , bin -1 has a primary phase factor of $e^{+ikR\breve{}_C}$ , bin j has a primary phase factor of $e^{-ikR\breve{}_{Cj}}$, and every bin shares the scalar phase factor $e^{-ikR\breve{}_{SC}}$ corresponding to the distance from the output observation point to the centroid of the target or origin.

## 7.2   Example Problems

To highlight the performance of the SPPF algorithm for output selection vectors with complicated frequency dependencies (SPPF-OSV), the results of this chapter will analyze several examples in the frequency range of 80 MHz to 800 MHz:

- Long thin wire with length of .3λ to 3λ

- Another long thin wire with length of length of .5λ to 5λ

- 4 spheres in a row

For all 3 example structures, the source is a plane wave traveling along the axis of symmetry, exciting the scattering targets between frequencies of 80 MHz and 800 MHz. The plane wave has non-zero electric field in the x direction and zero electric field in the y and z directions.

The figures in this section, (7.2,7.2, and 7.2), show the three structures and plots of the x component of the scattered electric field at the observation point $< 10, 10, 10 >$ over the desired frequency range. Model Order Reduction is used to plot the intermediary points since it would be too time consuming to solve the original system at each point.
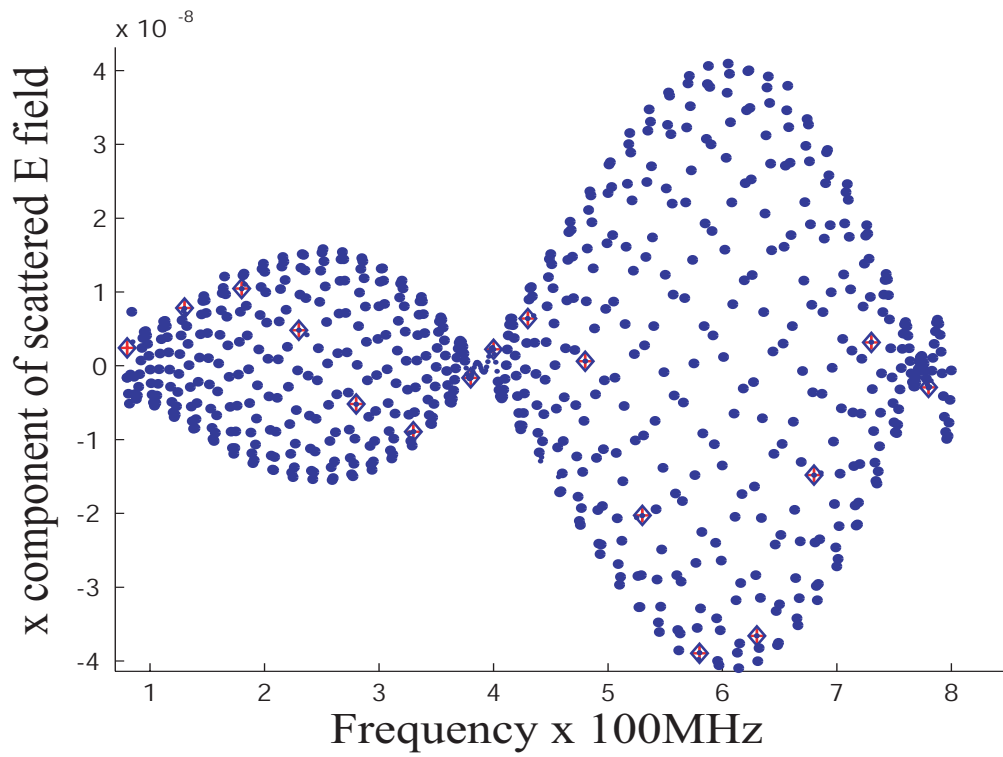
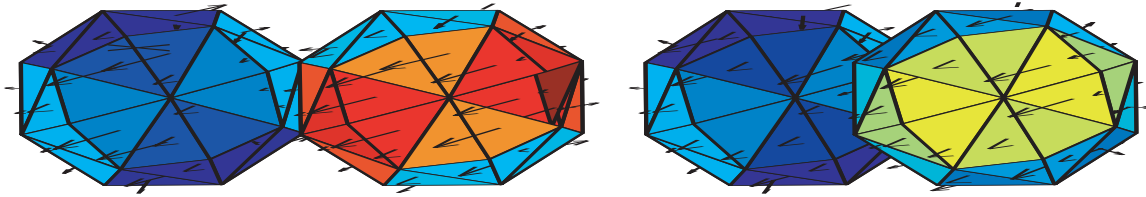(a) Long thin wire. Over the frequency range, the wire has length $.3\lambda$ to $3\lambda$.
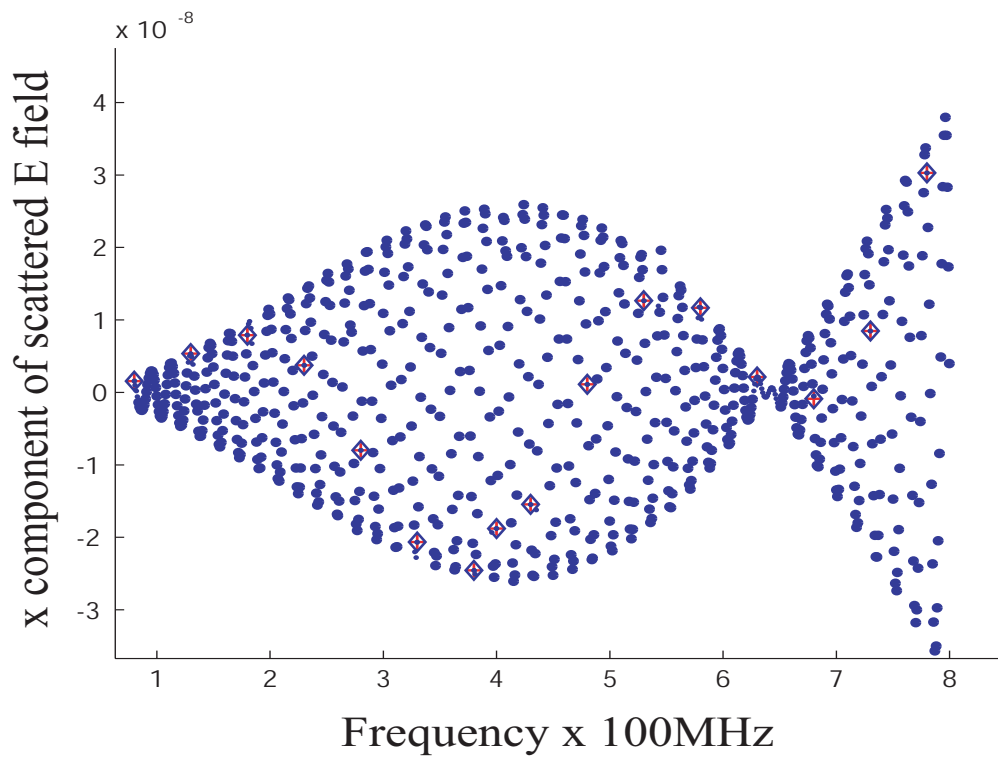


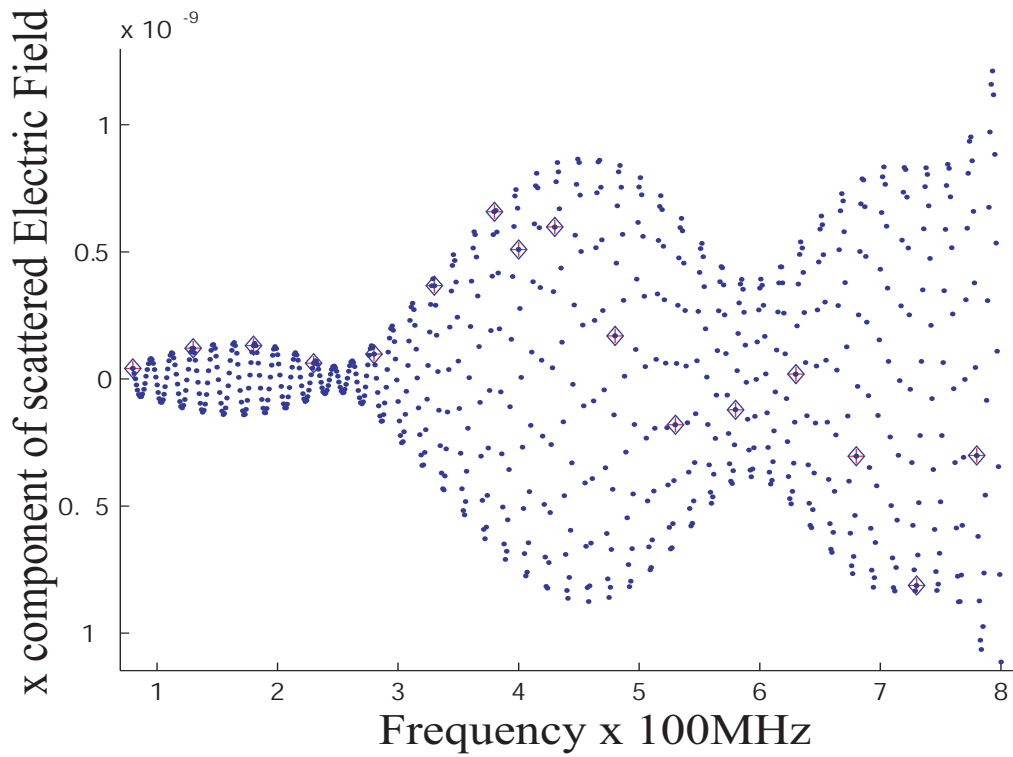(b) x component of the scattered electric field at the observation point $< 10, 10, 10 >$.
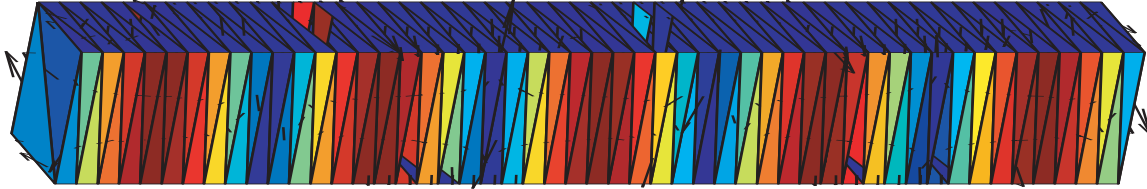
(c) Long thin wire. Over the frequency range, the wire has length $.5\lambda$ to $5\lambda$.



(d) x component of the scattered electric field at the observation point $< 10, 10, 10 >$.

(e) 4 Spheres in a row. Over the frequency range, each sphere has diameter of .01λ to .1λ and the row has length of .6λ to 6λ)



(f) x component of scattered Electric Field.

## 7.3    Results

For the examples presented in the previous section, an output selection vector $\boldsymbol{C}(s)$ with complicated (Helmholtz) frequency dependency will be required to compute the x component of the scattered electric field from the (scattering) currents induced by the incident source wave.

Since the previous chapter presented the new SPPF-RHSMP-FMOR algorithm, the output selection vector results in this section, will further compare results between the SPPF-OSV-RHSMP-FMOR and the preexisting ETAS-based multi-point full-wave model order reduction for output selection vectors with complicated frequency dependencies (ETAS-OSV-MP-FMOR) algorithms. Subsection 7.3.1 will show results that compare SPPF-OSV-FMOR and ETAS-OSV-FMOR, obtained using ETAS-based MP-FMOR with additional expansion points at 250 MHz and 600 MHz. Subsection 7.3.2 will show results that compare SPPF-OSV-FMOR and ETAS-OSV-FMOR, obtained using RHSMP-FMOR with additional expansion points at 250 MHz and 600 MHz. While all results highlight the accuracy improvement enabled by the SPPF algorithms (extended for the output-selection vectors), the results in subsection 7.3.2 will show that SPPF-OSV-RHSMP-FMOR ROMs have the capability to characterize the desired output behavior of original scattering target over the entire desired frequency range by including additional frequency expansion points, as necessary.

### 7.3.1    Results for SPPF-OSV-FMOR using ETAS-based multi-point MOR

This subsection presents results for the SPPF-OSV-FMOR algorithm using ETAS-based multi-point (ETAS-MP) to compute a ROM to characterize the the x component of scattered electric field at the observation point $< 10, 10, 10 >$ due to scattering from the original scattering target. For each of the example problems, the corresponding figure compares the error between the SPPF-OSV-FMOR ROM and ETAS-OSV-FMOR ROM to show the improved accuracy of the new SPPF-OSV-

FMOR algorithm applied to output selection vectors with complicated frequency dependencies. The compared ROMs are of equal size and both were generated using equal truncation order and ETAS-based multi-point MOR with additional expansion points at 250 MHz and 600 MHz.

The results in figure 7-2(h) compare the error in the computed x component of the electric field scattered from the wire in figure 7-2(g) between the SPPF-OSV-FMOR algorithm and the ETAS-FMOR using ETAS-MP. The improvement in accuracy is noticeable on the log error plot but it is less than a factor of 10, and at some points the results of the SPPF-OSV-FMOR are actually worse. These results are somewhat disappointing since they fail to realize the potential accuracy of the SPPF algorithms that the SPPF-ETAS figure 6-1(r) shown in chapter 6 suggests is possible. Furthermore, since there seems to be no dips in error at the additional expansion points, these results seem to highlight the poor performance of ETAS-based multi-point. Using the ETAS for multipoint expansions seems to hardly help increase the ROM's range of accuracy at all.

The second example scattering target is the longer wire shown in figure 7-2(i). The results, in figure 7-2(j), compare the error in the computed x component of the electric field scattered from the wire between the SPPF-OSV-FMOR algorithm and the ETAS-FMOR using ETAS-MP. The improvement in accuracy is noticeable on the log error plot, up to 1000 times better over a small range of frequencies, but not that great over much of the range. Furthermore the error in SPPF-OSV-FMOR is almost 100% over a significant portion of the frequency range. These results are even more disappointing (as would be expected for an electromagnetically larger problem) since they are further from realizing the potential accuracy of the SPPF algorithms that SPPF-ETAS model results such as figure 6-1(r) of chapter 6, suggested should be attainable. Once again, since there seems to be no dips in error at the additional expansion points, these results also highlight the poor performance of ETAS-based multi-point.

The third example scattering target is the row of 4 spheres shown in figure 7-2(k). The results, in figure 7-2(l), compare the error in the computed x component of
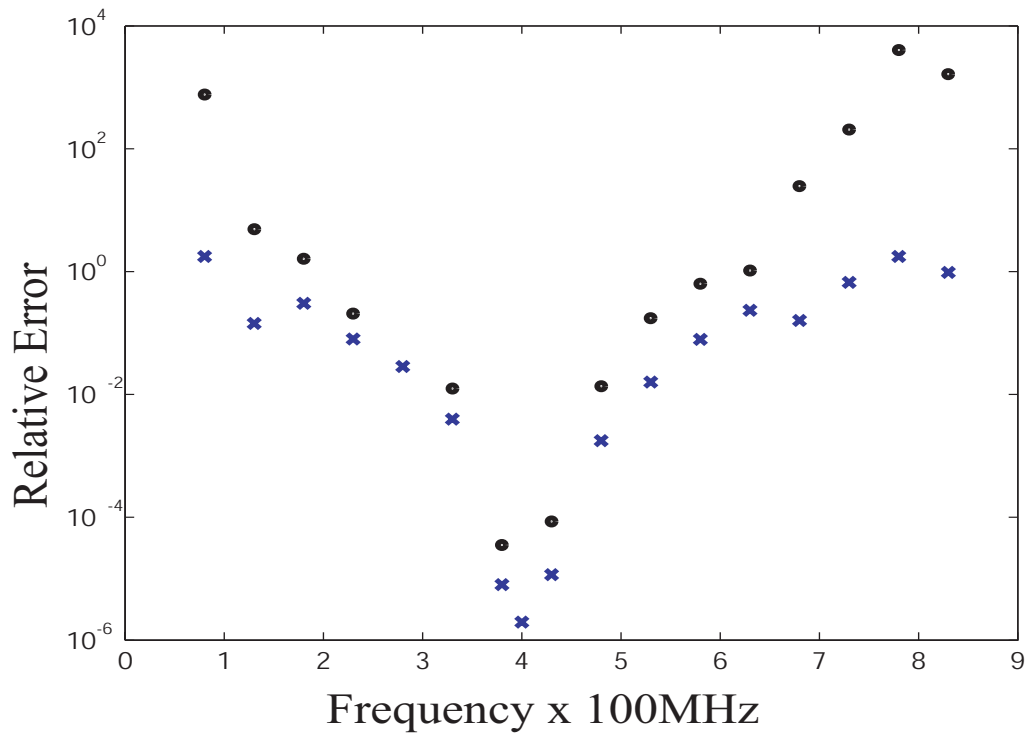
(g) Long thin wire. Over the frequency range, the wire has length .3λ to 3λ.
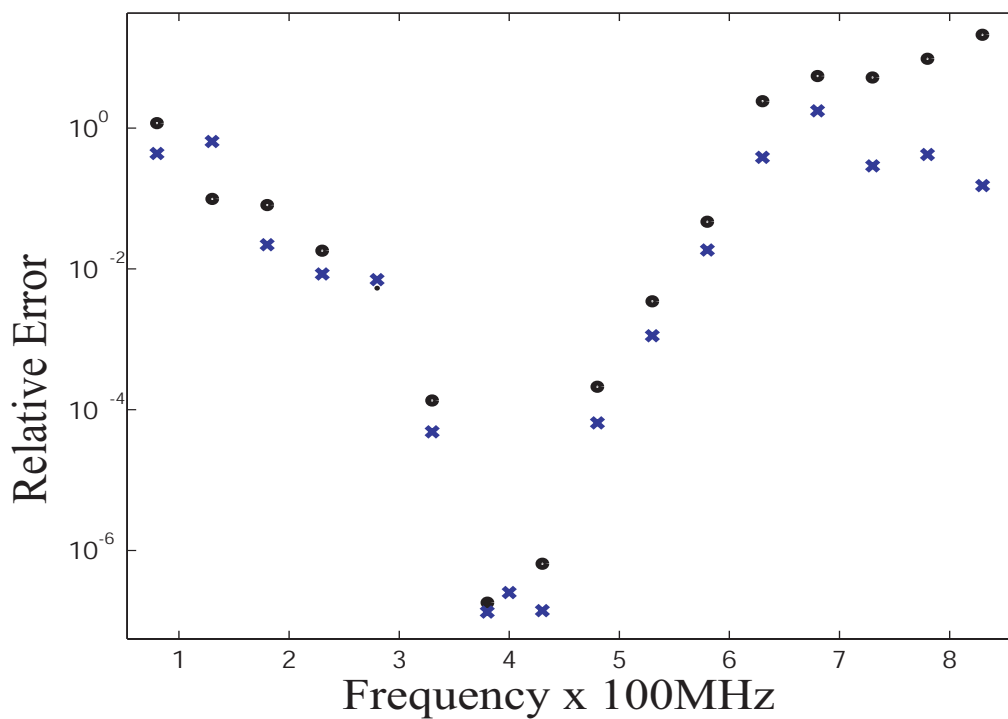


(h) This figure compares the Log scale plot of Relative Error of the X component of scattered electric field at observation point < 10, 10, 10 > computed by the new SPPF-FMOR (x) algorithm and by the previous ETAS-FMOR (.) methods plotted versus frequency. Both methods are using ETAS-based multipoint MOR. The ROM produced by new SPPF-OSV-FMOR achieves roughly 10 to 100 times better accuracy than the previous ETAS-OSV-FMOR method across the frequency range, although at some points it is worse.
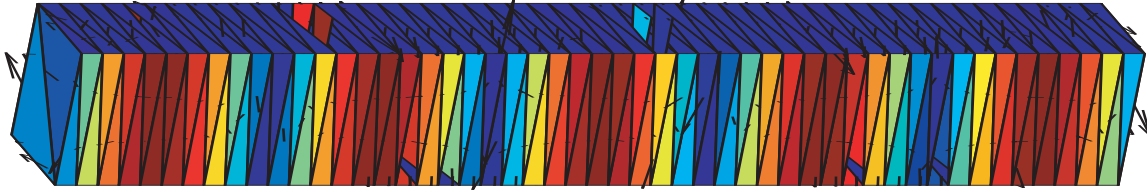
(i) Long thin wire. Over the frequency range, the wire has length $.5\lambda$ to $5\lambda$.



(j) This figure compares the Log scale plot of Relative Error of the X component of scattered electric field at observation point $<10, 10, 10>$ computed by the new SPPF-OSV-FMOR (x) algorithm and by the previous ETAS-OSV-FMOR (.) methods plotted versus frequency from 80MHz to 800 MHz for long thin wire example. The ROMs are designed to match additional expansion points using ETAS-based multipoint MOR. The SPPF-OSV-FROM algorithm achieves 10 to 10,000 times better accuracy over much of the frequency range.

the electric field scattered from the wire between the SPPF-OSV-FMOR algorithm and the ETAS-FMOR algorithm using ETAS-MP. The results of this example really highlight the strengths of the new algorithm. The improvement in accuracy quite good, but not as good as the SPPF-RHSMP-FMOR results of the previous chapter, and it would be nicer to demonstrate even better accuracy since output selection vectors often reduce the state that a ROM must characterize to retain accuracy. Furthermore, once again, over a small portion of the frequency range, the error of the SPPF-OSV-FMOR ROM reaches almost 100% . Yet again, for a third time, there seems to be no dips in error at the additional expansion points, which highlights the poor performance of ETAS-based multi-point and motivates use of the RHSMP presented in chapter 6.

### 7.3.2   Results for SPPF-OSV-RHSMP-FMOR Algorithm

This subsection shows results for computation of the x component of scattered electric field at the observation point $< 10, 10, 10 >$ using the SPPF-OSV-RHSMP-FMOR algorithms and compares these results those of the ETAS-based FMOR to show the improvements of this algorithm. The ROMs are of equal size and were generated using equal truncation order and each with additional expansion points at 250 MHz and 600 MHz.

The results in figure 7-2(n) compare the error in the computed x component of the electric field scattered from the wire in figure 7-2(m) between the SPPF-OSV-RHSMP-FMOR algorithm and the ETAS-FMOR. The improvement in ROM accuracy due to SPPF and RHSMP has jumped considerably almost 100-fold relative to the ETAS-FMOR ROM! Furthermore, dips in error are clearly visible near the additional expansion points (would be even clearer if the expansion points and more points around them were plotted), which clearly highlight the positive impact of RHSMP.

Figure 7-2(m) shows the longer wire which is "electromagnetically larger" in this full-wave analysis regime. Figure 7-2(p) compares the error in the computed x component of the electric field scattered from the wire between the SPPF-OSV-RHSMP-FMOR algorithm and the ETAS-FMOR. The improvement in ROM accuracy due to
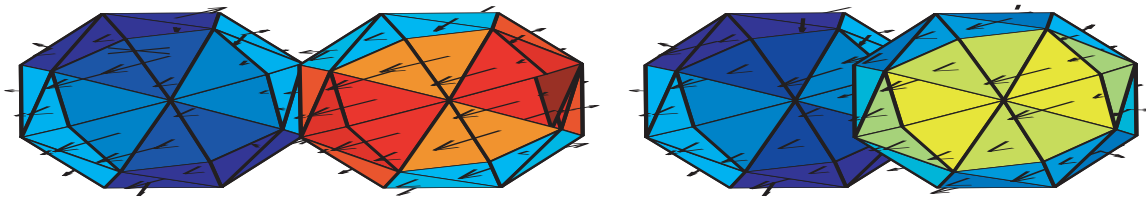
(k) 4 Spheres in a row. Over the frequency range, each sphere has diameter of $.01\lambda$ to $.1\lambda$ and the row has length of $.6\lambda$ to $6\lambda$)
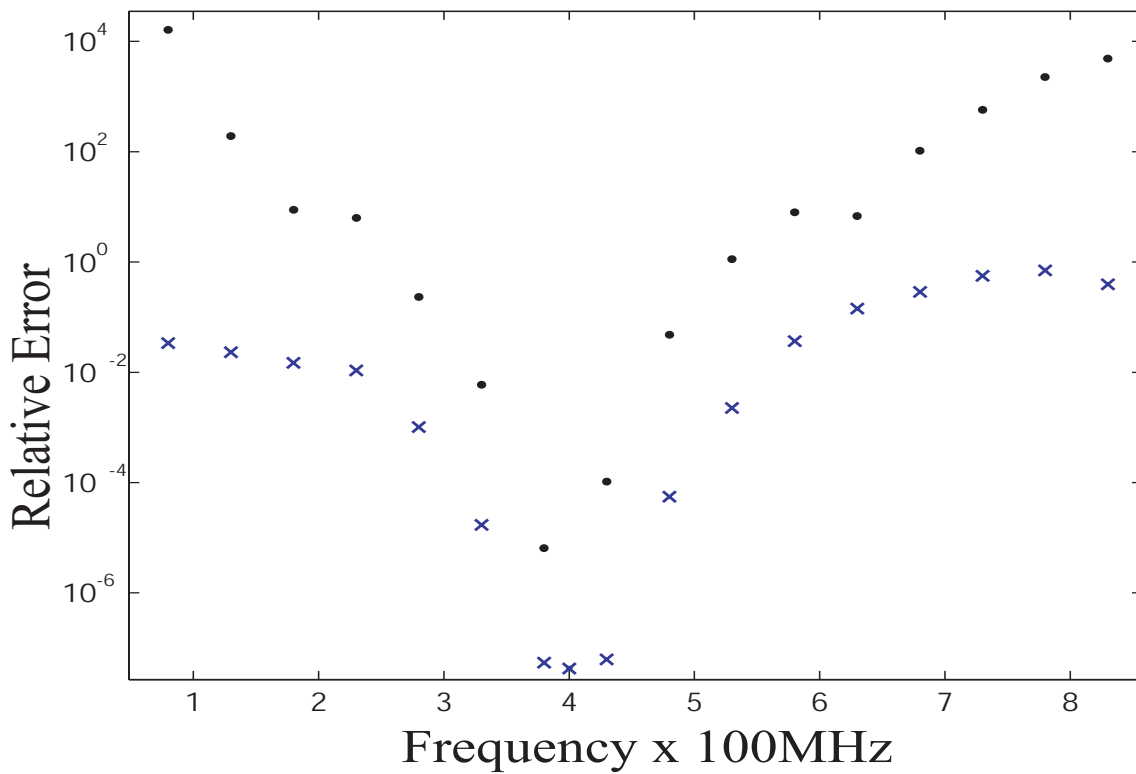


(l) This figure compares the Log scale plot of Relative Error of the X component of scattered electric field at observation point $< 10, 10, 10 >$ computed by the new SPPF-OSV-FMOR (x) algorithm and by the previous ETAS-OSV-FMOR (.) methods plotted versus frequency from 80MHz to 800 MHz for the row of 4 spheres example. The ROMs are designed to match additional expansion points using ETAS-based multipoint MOR. the SPPF-FMOR ROM achieves 1,000 to 1,000,000 times better accuracy than the ROM produced by ETAS-FMOR over much of the frequency range!

137

(m) Long thin wire. Over the frequency range, the wire has length $.3\lambda$ to $3\lambda$.
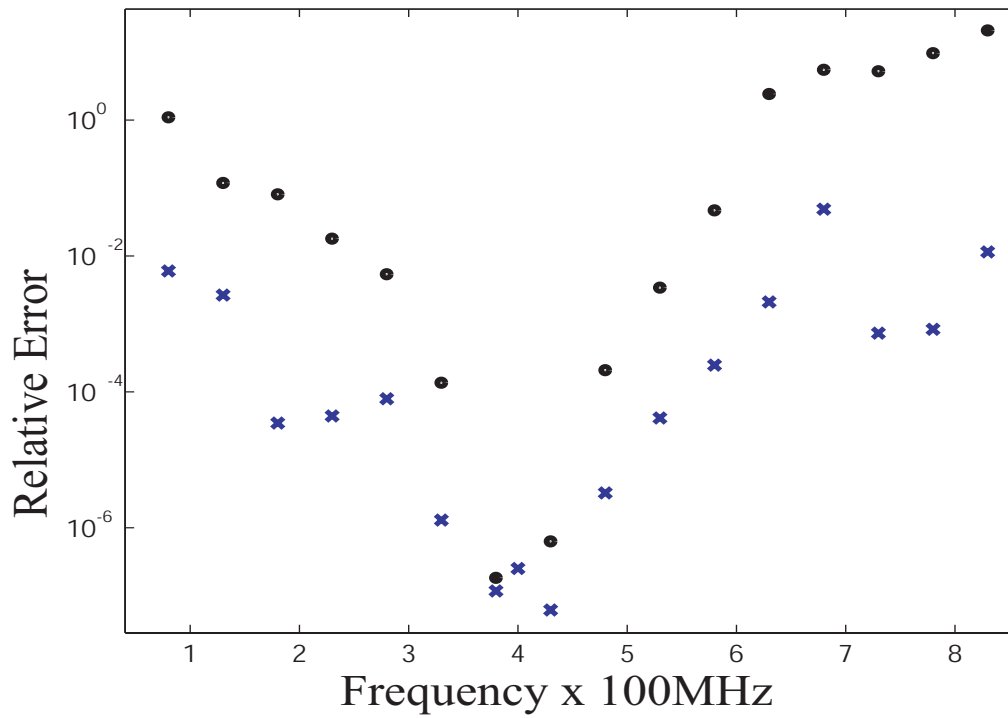


(n) This figure compares the Log scale plot of Relative Error of the X component of scattered electric field at observation point $< 10, 10, 10 >$ computed by the new SPPF-OSV-FMOR (x) algorithm and by the previous ETAS-OSV-FMOR (.) methods plotted versus frequency from 80MHz to 800 MHz for the long thin wire example. The SPPF-OSV-FMOR ROM achieves 1,00 to 10,000 times better accuracy than the ROM produced by ETAS-FMOR over much of the frequency range! This demonstrates a remarkable improvement in the SPPF-ROM's range of accuracy due to the new RHSMP multipoint MOR algorithm.

SPPF and RHSMP is even clearer, as the figure demonstrates 1,000 to 10,000-fold improvement relative to the ETAS-FMOR ROM! Furthermore, as in the previous example, dips in error are clearly visible near the additional expansion points (would be even clearer if the expansion points and more points around them were plotted), which clearly highlight the positive impact of RHSMP.

The final example scattering target of this chapter is the row of 4 spheres shown in figure 7-2(q). The results, shown in figure 7-2(r), compare the error in the computed x component of the electric field scattered from the wire between the SPPF-OSV-RHSMP-FMOR and the ETAS-FMOR algorithms. The accuracy of the SPPF-OSV-RHSMP-FMOR ROM is astonishing, almost 100,000,000 times less error than the ETAS-FMOR! The geometry of the 4 spheres aligned in a row is particularly suitable for SPPF-based analysis, but this final result suggests that RHSMP is required to fully realize its potential!

In summary, both SPPF-OSV-FMOR and SPPF-OSV-RHSMP-FMOR demonstrate significant improvements over ETAS-FMOR for generating ROMs that characterize the behavior of a desired output quantity $(y(s) = \boldsymbol{C}(s)^T \boldsymbol{J})$. Both the results in this chapter and the previous chapter highlight the strong impact of multi-point MOR, using RHSMP and potentially other multi-point algorithms (and suggest that multi-point algorithms that are based on evaluating the ETAS at the additional expansion points are ineffective).

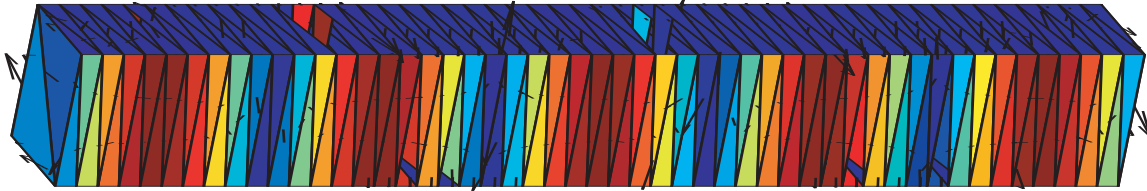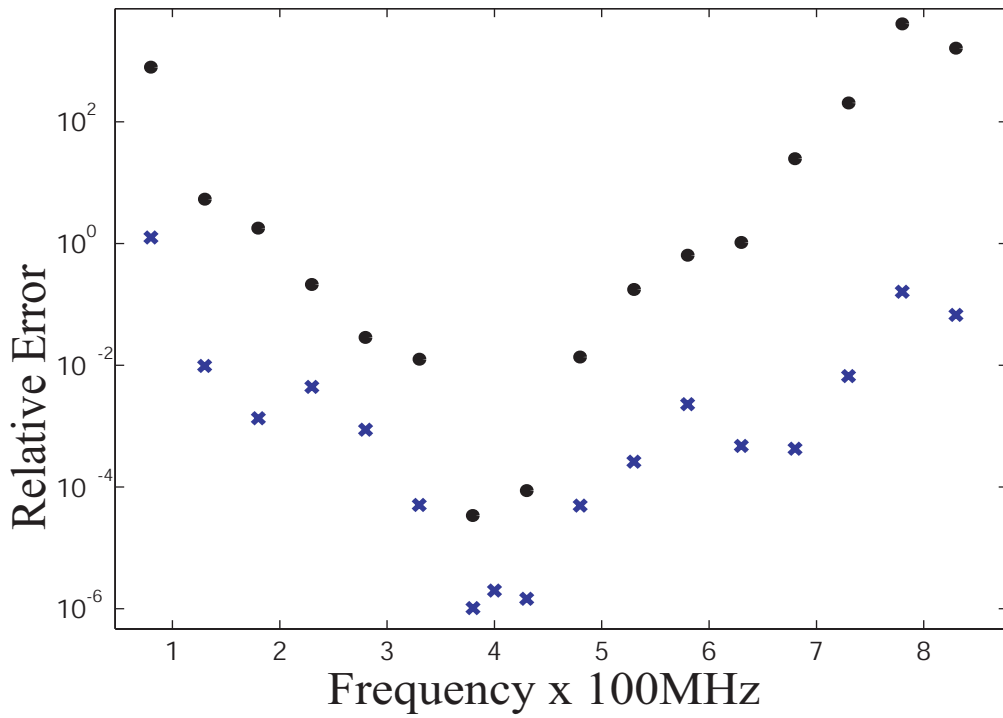(o) Long thin wire. Over the frequency range, the wire has length .5$\lambda$ to 5$\lambda$.



(p) This figure compares the Log scale plot of Relative Error of the X component of scattered electric field at observation point $< 10, 10, 10 >$ computed by the new SPPF-OSV-FMOR (x) algorithm and by the previous ETAS-OSV-FMOR (.) methods plotted versus frequency from 80MHz to 800 MHz for the long thin wire example. The SPPF-OSV-FMOR ROM achieves 1,000 to 100,000 times better accuracy than the ROM produced by ETAS-FMOR over much of the frequency range! This demonstrates a remarkable improvement in the SPPF-ROM's range of accuracy due to the new RHSMP multipoint MOR algorithm.
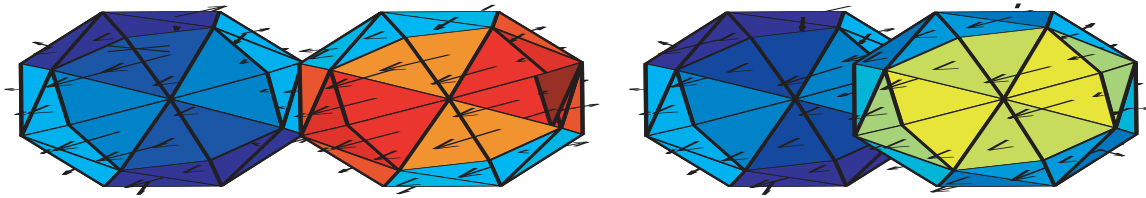
(q) 4 Spheres in a row. Over the frequency range, each sphere has diameter of $.01\lambda$ to $.1\lambda$ and the row has length of $.6\lambda$ to $6\lambda$
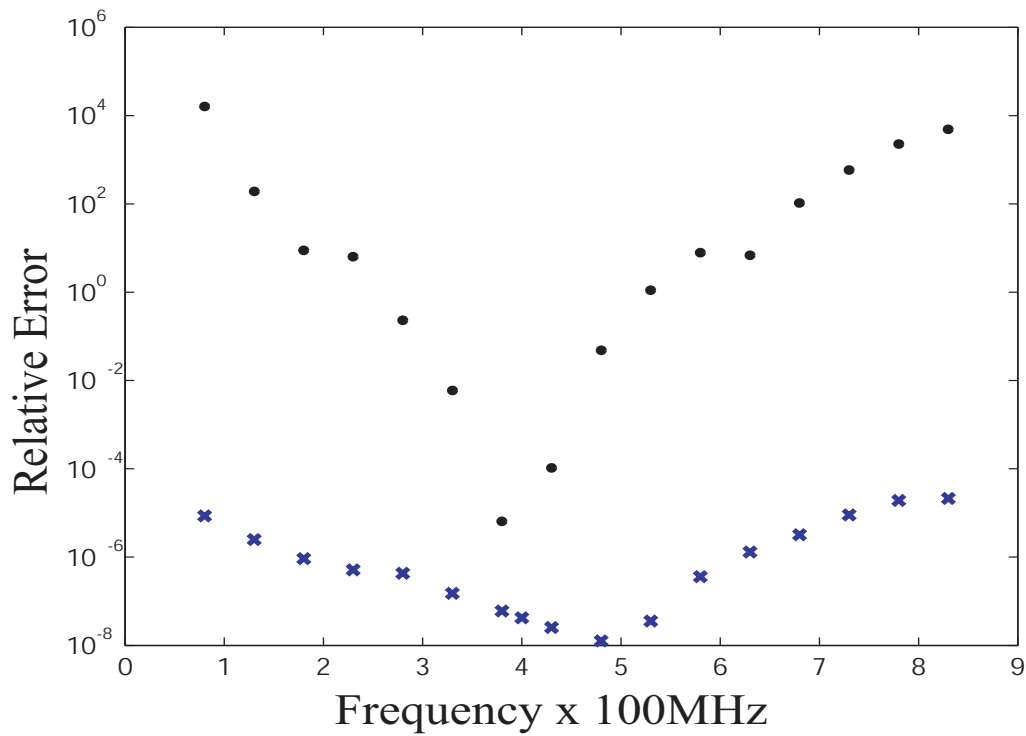


(r) This figure compares the Log scale plot of Relative Error of the X component of scattered electric field at observation point $< 10, 10, 10 >$ computed by the new SPPF-OSV-FMOR (x) algorithm and by the previous ETAS-OSV-FMOR (.) methods plotted versus frequency from 80MHz to 800 MHz for the long thin wire example. The SPPF-OSV-FMOR ROM achieves 100,000,000 times better accuracy than the ROM produced by ETAS-FMOR over most of the frequency range!!! This demonstrates a remarkable improvement in the SPPF-ROM's range of accuracy due to the new RHSMP multipoint MOR algorithm.

141

# Chapter 8

# Extending Segmentation by Primary Phase Factors to incorporate PFFT sparsification algorithm

The SPPF algorithm for model order reduction proposed in sections 4 and 7 did not discuss sparsification techniques, which are often utilized in conjunction with iterative methods for solving large linear systems of equations. The SPPF algorithm depends on access to the dense system matrices in order to separate each frequency dependent exponential into a primary component $e^{-ik\breve{R}i}$ (integer multiple of $\breve{R}$) and a remainder component, $e^{-ikd}$.

The entries of the system matrix can be segregated,

$$\boldsymbol{Z}_{mn} = z_{mn}\frac{e^{-ikr_{mn}}}{r_{mn}} = z_{mn}\frac{e^{-ik(\breve{R}l_{mn}+d_{mn})}}{r_{mn}} = z_{mn}e^{-ik\breve{R}l_{mn}}\frac{e^{-ikd_{mn}}}{r_{mn}}, \qquad (8.1)$$

where $l_{mn} \in 1, \cdots, \breve{n}$. Computing the remainder terms, using equation 8.1, is the first step in segregating the system matrix into multiple matrices, each corresponding to a primary phase factor, as follows:

$$\boldsymbol{Z}(s) = e^{-ik\check{R}0}\boldsymbol{P_0}\check{\boldsymbol{Z}}(s) + e^{-ik\check{R}}\boldsymbol{P_1}\check{\boldsymbol{Z}}(s) + \cdots + e^{-ik\check{R}\check{n}}\boldsymbol{P_{\check{n}}}\check{\boldsymbol{Z}}(s). \qquad (8.2)$$

This first step of the SPPF algorithm may present a problem when sparsification algorithms such as PFFT are considered, because the chief advantage of the PFFT algorithm comes from the fact that the system matrices are never constructed and are not required for iterative solution techniques such as generalized minimum residual (GMRES), since the PFFT algorithm supplies the results of the matrix-vector products without forming the system matrices.

Fortunately, it turns out that SPPF-Dense can be modified to incorporate the PFFT algorithm without too much difficulty. In fact, implementation of the SPPF algorithm for PFFT (SPPF-PFFT) is less complex than SPPF for non-sparsified (SPPF-Dense) systems (described in chapter 4). SPPF-Dense requires access to the factor multiplied with frequency in the exponent of terms in the system with exponential frequency dependency. Thus, the key to extending SPPF to include sparsification techniques is to identify the frequency dependencies in the sparsified (PFFT) representation of the system.

By examining the PFFT algorithm,

$$\begin{aligned} \boldsymbol{Z}(s)\boldsymbol{J} &\approx [\boldsymbol{W}^T\boldsymbol{G_G}\boldsymbol{W} + \boldsymbol{N_{EX}} - \boldsymbol{N_G}]\boldsymbol{J} \\ &= \boldsymbol{W}^T\mathcal{F}^{-1}(diag(\mathcal{F}(\boldsymbol{g_G}))\mathcal{F}(\boldsymbol{J_G})) + (\boldsymbol{N_{EX}} - \boldsymbol{N_G})\boldsymbol{J}, \qquad (8.3) \end{aligned}$$

it is clear that the projection and interpolation matrix, $\boldsymbol{W}$, contains no frequency dependence and that the precorrection matrices $\boldsymbol{N_G}$ and $\boldsymbol{N_{EX}}$ contain separation distance factors of frequency in their exponent which have a maximum possible value equal to the diameter of a 27 cell cube of neighboring grid cells, and thus should be accurately approximated by low order truncated Taylor expansions.

Furthermore, equation 8.3 illustrates that only the convolution matrix $\boldsymbol{G_G}(s)$ has

terms with exponentials that have exponent factors of frequency large enough so that some of its elements cannot be accurately approximated by low order truncated Taylor series. Depending on the ratio of the maximum grid point separation distances present to the minimum wavelengths being examined, it may be necessary that a very large number of terms must be kept from the series, or otherwise the truncated portion of the series will not be negligible. Thus, the convolution matrix $\boldsymbol{G_G}(s)$ is the sole focus of attention for applying SPPF concepts to the PFFT algorithm, but because of the Fourier transform properties that relate convolution in the original domain to multiplication in the transform domain, the vector $\boldsymbol{g_G}$ (much smaller than $\boldsymbol{G_G}(s)$) is segregated into primary phase components to obtain

$$\boldsymbol{ZJ} \approx \sum_{j=0}^{\breve{n}} e^{-ik\breve{R}j} \boldsymbol{W}^T (\boldsymbol{P_j}\breve{\boldsymbol{h}}_{\boldsymbol{G}}) * \boldsymbol{J_G} + (\boldsymbol{N_{EX}} - \boldsymbol{N_G})\boldsymbol{J}. \tag{8.4}$$

The summation with the primary phase factors $e^{-ik\breve{R}l}$ can be pulled out of the convolution because convolution is a linear operation. Notice that the precorrection $\boldsymbol{N_G}$ and $\boldsymbol{N_{EX}}$ terms are unaffected by the SPPF algorithm since none of the separation distances (whether between panel points or grid points) exceed $\breve{R}$. Replacing the convolution operation with FFT and IFFT algorithms yields

$$\boldsymbol{ZJ} \approx \sum_{j=0}^{\breve{n}} e^{-ik\breve{R}j} \boldsymbol{W}^T \mathcal{F}^{-1}(diag(\mathcal{F}(\boldsymbol{P_j}\breve{\boldsymbol{h}}_{\boldsymbol{G}}))\mathcal{F}(\boldsymbol{J_G})) + (\boldsymbol{N_{EX}} - \boldsymbol{N_G})\boldsymbol{J}. \tag{8.5}$$

Summing the various scalar and vector potential contributions and substituting a truncated Taylor approximation for $\boldsymbol{g_G}(kr)$, results in

$$
\begin{aligned}
\boldsymbol{Z_l J_l} &\approx \sum_{j=0}^{\breve{n}} e^{-ik\breve{R}j} \boldsymbol{W}^T \mathcal{F}^{-1}(\sum_{n=0}^{n_G} diag(\boldsymbol{P_j}\frac{(s-s_T)^l}{l!}\tilde{\breve{\boldsymbol{h}}}_{\boldsymbol{Gl}}[n])\tilde{\boldsymbol{J}}_{Gl}[n]e^{\frac{2\pi mn}{n_G}}) \\
&+ (\boldsymbol{N_{EXl}} - \boldsymbol{N_{Gl}})\boldsymbol{J_l}.
\end{aligned}
\tag{8.6}
$$

which corresponds to computing the matrix-vector products with the blocks $\boldsymbol{Z_l}$ in the

145

(s) $\frac{\cos(kr)}{r}$

(t) $\frac{\cos(kr)}{r}, \quad 0 < |r| < \frac{\breve{R}}{2}$

(u) $\frac{\cos(kr)}{r}, \quad \frac{\breve{R}}{2} < |r| < \frac{3\breve{R}}{2}$

(v) $\frac{\cos(kr)}{r}, \quad \frac{3\breve{R}}{2} < |r| < \frac{5\breve{R}}{2}$

(w) $\frac{\cos(kr)}{r}, \quad \frac{5\breve{R}}{2} < |r| < \frac{7\breve{R}}{2}$

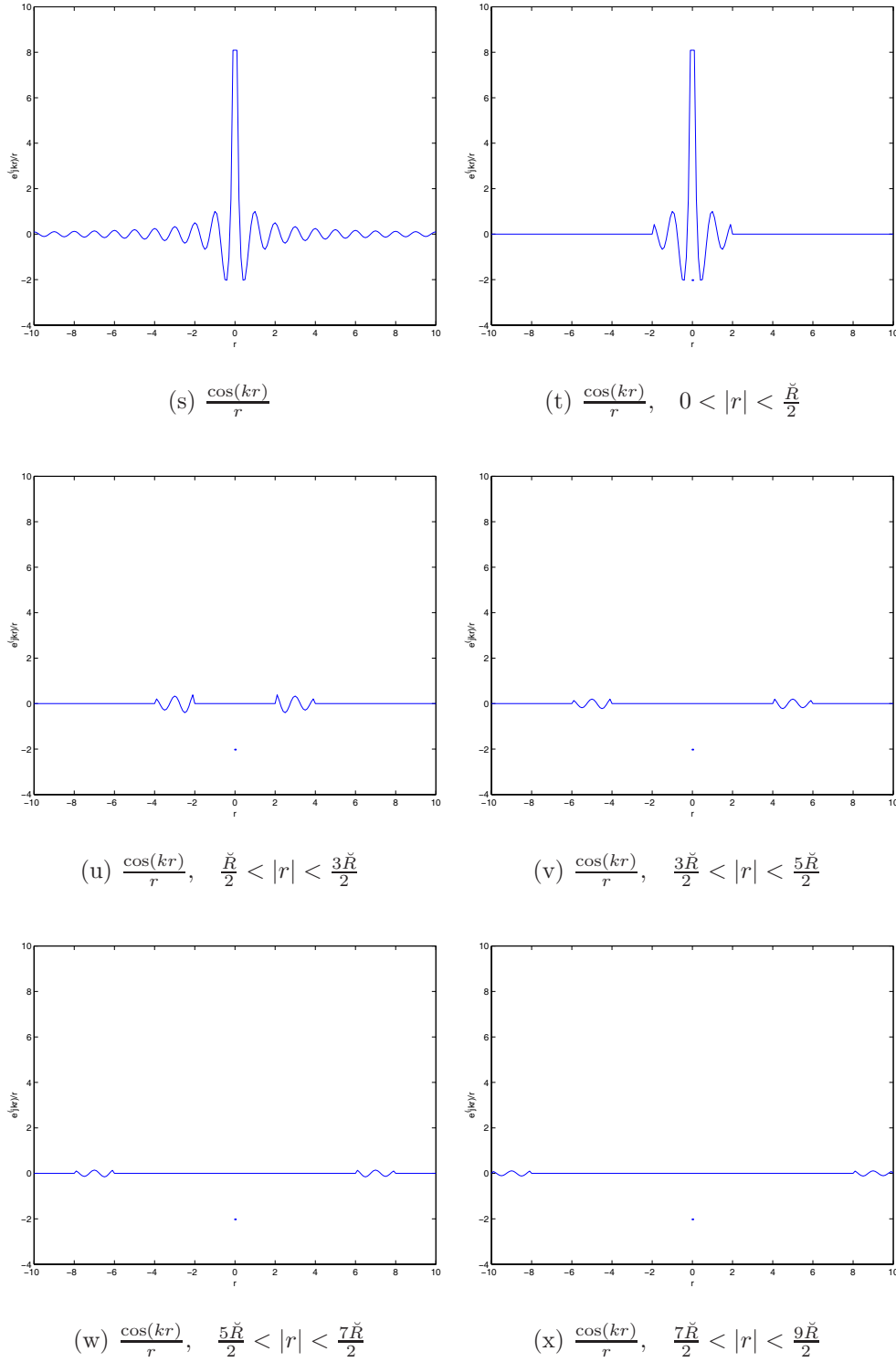(x) $\frac{\cos(kr)}{r}, \quad \frac{7\breve{R}}{2} < |r| < \frac{9\breve{R}}{2}$

Figure 8-1: Full Greens Function and Segregated Green's Function segments

146

top row of the ETAS and summing those terms in the truncated Taylor Expansion[1].
Examining 8.6, we can see that modifying SPPF to incorporate PFFT is actually easier to implement than SPPF for the original unsparsified (dense) system matrices for several reasons: 1) PFFT diagonalizes the matrix corresponding to convolution with the Green's function by projecting edge quantities to grid-point quantities. Thus, in SPPF-MOR-PFFT only $n_G$ quantities in the Green's function vector need to be Segregated by their Primary Phase Factors as opposed to $n_E^2$ for the dense unsparsified system matrices. To apply SPPF-Dense, we have to segregate the entire system matrix by primary phase components, while for SPPF-PFFT we only need to segregate the $g_G$ vector. 2) SPPF-Dense has to handle cases where the four panels associated with a particular edge pair are not all classified into the same bin corresponding to the closest integer multiple of $\breve{R}$, while for SPPF-PFFT, the grid point pair separation distances are unique, and thus every grid point pair has phase contribution from only one primary phase factor. Key steps for Segregation into Primary Phase Factors with the PFFT algorithm are illustrated in figure 8-2, below.

## 8.1 Extending SPPF-PFFT for full-wave Model Order Reduction

Applying MOR to the SPPF-PFFT algorithm is straightforward and the same process as discussed in sections 4.5 and 5.3. We briefly outline the steps involved to apply of MOR to the system in conjunction with SPPF-PFFT, starting by applying SPPF to the expanded state space system matrix from equation 2.28, obtaining

$$
\boldsymbol{Z}(s)\boldsymbol{J} \approx \sum_{j=0}^{\breve{n}} e^{-ik\breve{R}i}\boldsymbol{P_j} \left[\begin{bmatrix} \breve{\boldsymbol{Z}}_{\boldsymbol{0}} & \boldsymbol{0} & \cdots \\ \boldsymbol{0} & \boldsymbol{I} & \ddots \\ \vdots & \ddots & \ddots \end{bmatrix}\right.
$$

---

[1]Note: equation 8.6 incorporates the new state vectors introduced in 2.70
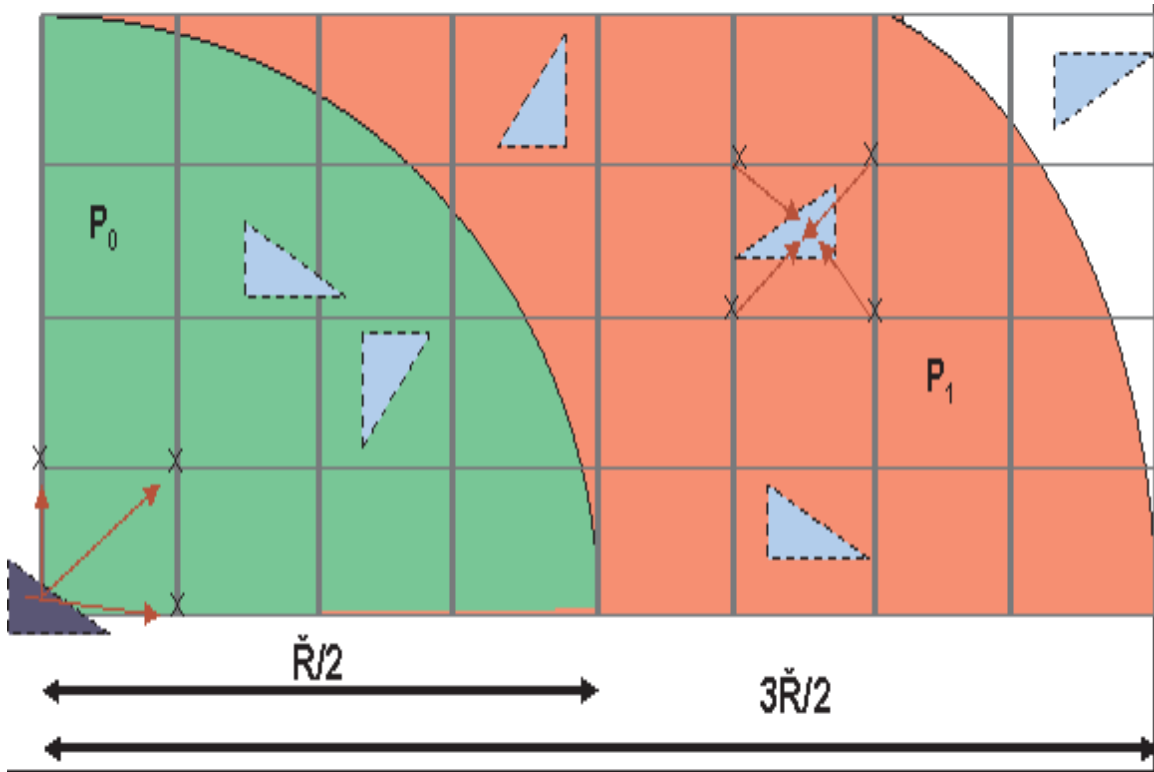
Figure 8-2: Segregation by Primary Phase Factors with PFFT Sparsification: This figure is similar to figure 4-2 except that it shows how PFFT Green's function grid-point to grid-point interactions can be segregated into SPPF bins and the associated primary phase factors. Precorrection all takes place in the $0th$ bin with a primary phase factor of one, such that precorrection routines and quantities are unaffected by the SPFF algorithm.

$$+\Delta(s) \begin{bmatrix} -\breve{Z}_1 & -\breve{Z}_2 & -\breve{Z}_3 & \cdots & -\breve{Z}_{n_T-1} \\ \frac{I}{2} & 0 & 0 & \cdots & 0 \\ 0 & \frac{I}{3} & 0 & \cdots & 0 \\ \vdots & \ddots & \ddots & \ddots & 0 \\ 0 & 0 & 0 & \frac{I}{n_T-1} & 0 \end{bmatrix} \begin{bmatrix} \breve{J}_0 \\ \breve{J}_1 \\ \breve{J}_2 \\ \vdots \\ \breve{J}_{n_T-1} \end{bmatrix} \approx \mathcal{B}. \qquad (8.7)$$

Using sparsification techniques, this system matrix is never actually created. Solving the ETAS with iterative methods such as GMRES requires only matrix-vector products. Generating the projection matrix $V$, which spans the Krylov subspace described in, also only consists of matrix-vector products. Therefore, during a matrix vector product with the SPPF-ETAS, each of the dense blocks in the top row is "realized" by using the PFFT to compute the corresponding contribution of that particular block to the matrix-vector product, as described in previous sections 2.6.4 to 2.6.8.

In a sparsified solver, the ETAS is never constructed explicitly, and equations 8.7 are only realized in terms of matrix-vector multiplications. The entries in the top row correspond to application of the PFFT algorithm to a portion of the extended current density state vector (or vector of same size). Thus, at each grid point, $n_T$ derivatives of the corresponding $g_G$ entry must be stored, with the primary phase factors removed (divided out). The Krylov projection vector, $V$, is generated directly from the system in equation 2.70 (without any application of SPPF).

To reduce equation 8.7 and obtain a reduced order model, premultiply by $V^T$ and postmultiply by $V$ to compute

$$\begin{aligned} \widehat{\breve{\mathcal{Z}}}(s)\widehat{\breve{\mathcal{J}}} &= \sum_{j=0}^{\breve{n}} e^{-ik\breve{R}j} V^T P_j (\breve{Z}_{R1} - (s - s_T)\breve{Z}_{R2}) V \widehat{\breve{\mathcal{J}}} \\ &= \sum_{j=0}^{\breve{n}} e^{-ik\breve{R}j} (\widehat{\breve{\mathcal{Z}}}_{1j} - (s - s_T)\widehat{\breve{\mathcal{Z}}}_{2j}) \widehat{\breve{\mathcal{J}}} \\ &= \sum_{j=0}^{\breve{n}} e^{-ik\breve{R}j} V^T P_j \breve{\mathcal{E}} = \sum_{j=0}^{\breve{n}} e^{-ik\breve{R}j} \widehat{\breve{\mathcal{E}}}_{Rj}, \qquad (8.8) \end{aligned}$$

149

just as before with dense matrices. The ROM is explicitly created and is segregated by primary frequency factors. Above, $\breve{\mathbf{Z}}(s)$ represents the entire system in equation 8.8 and $\widehat{\widetilde{\mathbf{Z}}}(s)$ is the reduced order matrix.

## 8.2 Results for SPPF-PFFT-FMOR applied to EM Scattering analysis

The SPPF-PFFT algorithm has not yet been implemented for the impedance extraction solver, so the results in this section are restricted to EM scattering examples. Two example structures were chosen to demonstrate the utility of the SPPF-PFFT-FMOR algorithms for Electromagnetic Scattering Computations.

- Long thin wire

- 4 spheres in a row

For both example structures, the source is a plane wave traveling along the axis of symmetry, exciting the scattering targets between frequencies of 80 MHz and 800 MHz, and for both example problems, the relative error is compared between SPPF-MOR and the traditional MOR methods for $n_T = 8$. As these results were obtained much earlier that the results in previous chapters, the truncation order used to obtain these results is 2 orders higher and the $\breve{R}$ parameter is much smaller (or $\breve{n}$ parameter is much larger), so the resulting ROMs are correspondingly more accurate.

Figure 8.2 demonstrates 10 to 100-fold improvement for SPPF-FMOR ROM accuracies vs pre-existing FMOR-ETAS methods over the entire frequency range using both the dense-matrix and PFFT-accelerated iterative solvers. For both SPPF-FMOR and FMOR-ETAS, the PFFT and dense solutions are difficult to discern from each other on the graphs because they coincide in most[2] locations.

---

[2]The differences are probably due to the fact that the PFFT implementation is a Galerkin procedure, while the dense implementation uses a RWG basis and centroid delta function testing functions.
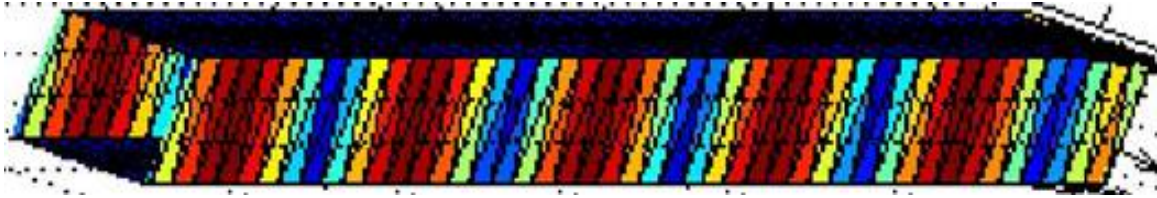
(a) Long, thin wire. For the frequency range of analysis, the wire has length of $.3\lambda$ to $3\lambda$.
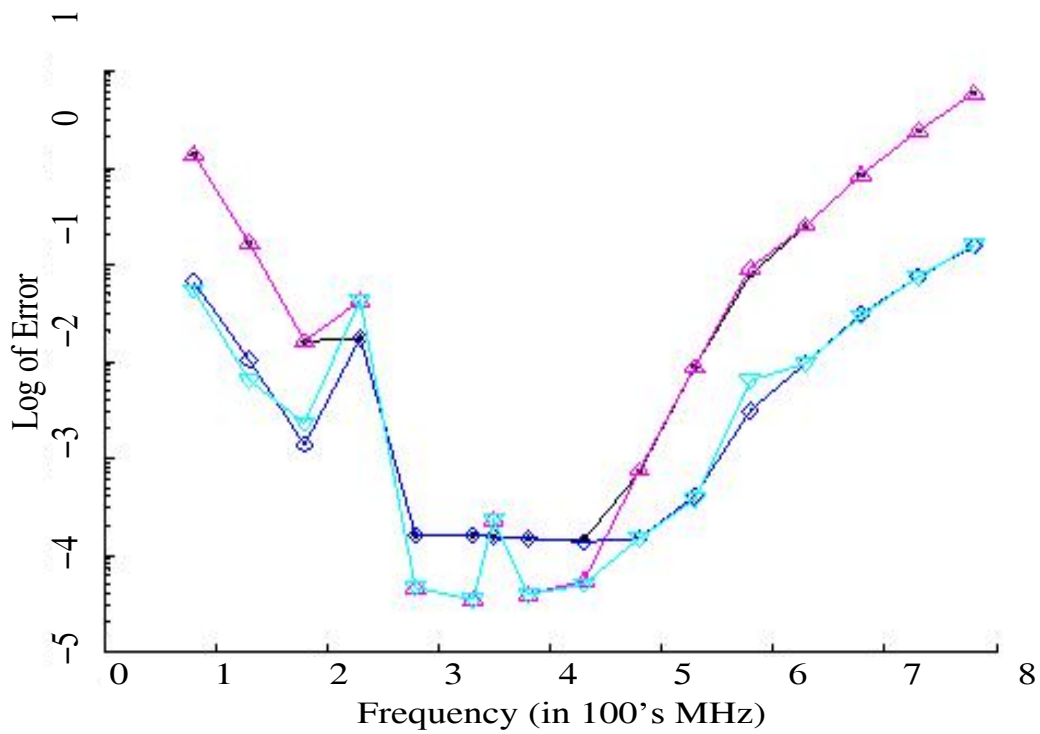


(b) Log of Relative Error vs frequency. This plot compares the new SPPF-FMOR algorithm to the pre-existing FMOR-ETAS methods,. The dense($\diamond$) and PFFT($\bigtriangledown$) SPPF-FMOR ROMs achieves 10 to 100 times better accuracy than the dense($\cdot$) and PFFT($\triangle$) ROMs produced by the FMOR-ETAS method, over the entire frequency range!

Figure 8.2 demonstrates 10,000 to 1,000,000 improvement for the dense and PFFT SPPF-MOR ROM accuracies vs the dense and PFFT ROMs generated by pre-existing ETAS-FMOR method over much of the entire frequency range.

Both sets of results show that the dense and PFFT solutions are practically superimposed on top of each other at many points, and the few differences are probably due to the fact that the choice to use the same PFFT interpolation and projection operators results in a Galerkin discretization for the PFFT solver, as opposed to non-Galerkin discretization, utilizing RWG basis functions and centroid-based delta testing functions, of the dense solver that was described in earlier chapters. Both the PFFT and Dense solver results strongly support the notion that SPPF-FMOR will be of great benefit to EM scattering applications. Furthermore, once the SPPF-based multi-point techniques (SPPF-MRHSP-FMOR) are incorporated into the SPPF-PFFT-FMOR algorithm, the accuracy improvement should be even greater!
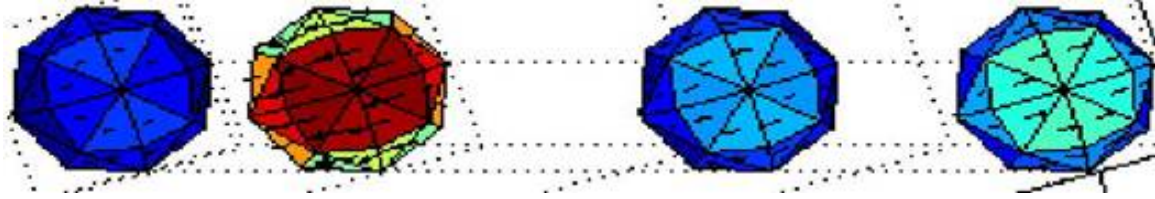
(c) 4 Spheres in a row. For the frequency range of analysis, the spheres each have diameter of .01$\lambda$ to .1$\lambda$ and the row has length of .6$\lambda$ to 6$\lambda$)
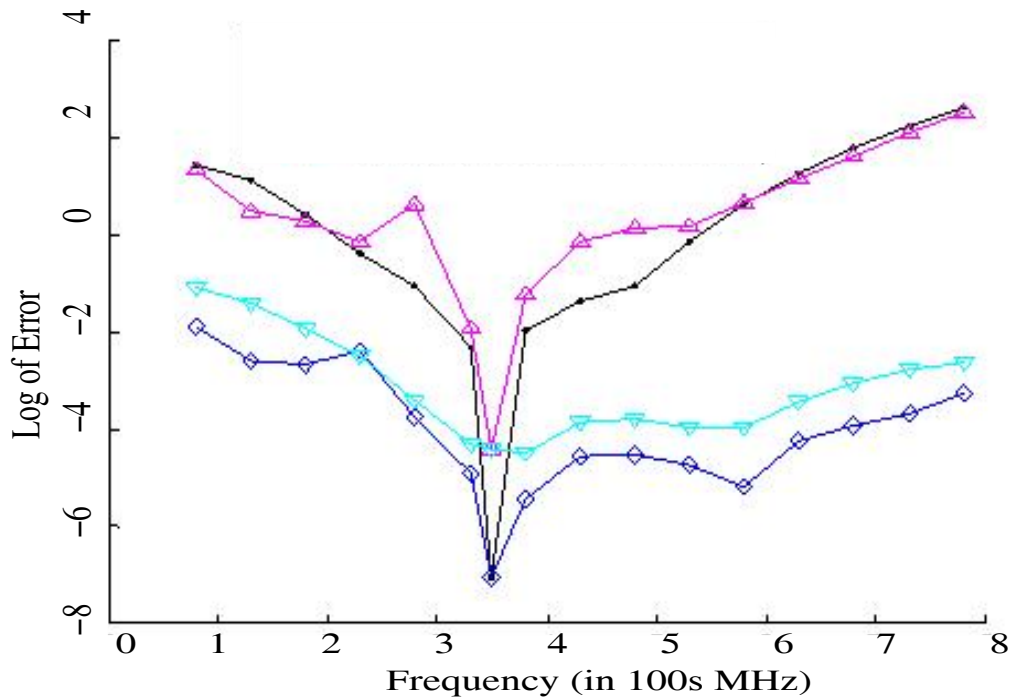


(d) Log of Relative Error vs frequency. This plot compares the new SPPF-FMOR algorithm to the pre-existing FMOR-ETAS methods. The dense($\diamond$) and PFFT($\triangledown$) SPPF-FMOR ROMs achieves 10,000-1,000,000 times better accuracy than the dense($\cdot$) and PFFT($\triangle$) ROMs produced by the FMOR-ETAS method, over the entire frequency range!!!

153

# Chapter 9

# Multi-parameter, full-wave MOR (MPAR-FMOR)

Electromagnetic analysis of impedance extraction and scattering problems frequently involve other parameters in addition to frequency. Sometimes it is desirable to extract impedance models that are function of geometrical parameters of the interconnect line, such as width and length, for interconnect analysis. Techniques to do this have been described in the literature [9]. In EM scattering analysis of airplane radar signals scattering from ground targets, there are also other parameters of interest. Since airplanes fly, angle at which the incident field contacts the scattering object will change as the airplane moves. Thus, for these types of solvers, look angle is a significant parameter in addition to the frequency of the incident signal, and it would be of great value to generate accurate Reduced Order Models (ROMs) which characterize both the frequency and look angle behavior of the original system.

The sections of this chapter address several possible techniques to generate ROM's that are parameters of frequency and additional parameters. Since multi-parameter MOR (MPAR-MOR) algorithms already have been developed and described in [9] for the impedance extraction, this dissertation will not attempt to re-examine them. However, the subsequent sections of this chapter will discuss potential techniques and present new MOR algorithms for generating multi-parameter ROM's for EM scattering analysis in full-wave regimes.

## 9.1 ROMs that include frequency and zenith look angle

To consider how we might generate ROMs which include the zenith look angle as a parameter we first examine how the incident field depends on the zenith look angle. For an incident plane wave approaching along the $z'$ axis, with look angle of 0 radians, each entry has the form $e^{-ikz}$. Basically, as shown in Appendix B, one can think about the look angles as a rotation from the $z$-axis through the zenith look angle, and with that perspective, the *mth* entry would be

$$e^{ikz'_m} = e^{ikz_m \cos(\Delta\phi)} \tag{9.1}$$

Thus, including the zenith look angle parameter, the right hand side would be

$$\sum_{j=0}^{\breve{n}} e^{ik\breve{R}i} \boldsymbol{P_j}\breve{\boldsymbol{\mathcal{E}}} = \sum_{j=0}^{\breve{n}} e^{ik\breve{R}i} \boldsymbol{P_j} \begin{bmatrix} \vdots \\ \breve{\boldsymbol{\mathcal{E}}}_m e^{ikz_m \cos(\Delta\phi)} \\ \vdots \end{bmatrix}, \tag{9.2}$$

and expanding the source vector into a Taylor Series representation would yield an *mth* entry proportional to

$$e^{ikz'_m} = e^{ik_T z_m \cos(\Delta\phi)}\left(1 + [i(k - k_T)z_m \cos(\Delta\phi)] + \cdots + \frac{[i(k - k_T)z_m \cos(\Delta\phi)]^n}{n!} + \cdots\right). \tag{9.3}$$

The key observation, in order to develop a two parameter ROM, is that one can choose the expansion variable to be $j(k - k_T)\cos(\Delta\phi)$ instead of $j(k - k_T)$, and then the ETAS approximation of the system is

$$\breve{\boldsymbol{\mathcal{Z}}}(s)\breve{\boldsymbol{\mathcal{J}}} = \sum_{j=0}^{\breve{n}} e^{-ik\breve{R}i} \boldsymbol{P_j}(\breve{\boldsymbol{\mathcal{Z}}}_1 - (s - s_T)\breve{\boldsymbol{\mathcal{Z}}}_2)\breve{\boldsymbol{\mathcal{J}}}$$

$$= \sum_{j=0}^{\breve{n}} e^{-ik\breve{R}j} \boldsymbol{P_{Ej}}(\breve{\boldsymbol{\mathcal{E}}}_0 + \xi\breve{\boldsymbol{\mathcal{E}}}_1 + \cdots + \frac{\xi^{n_T - 1}}{(n_T - 1)!}\breve{\boldsymbol{\mathcal{E}}}_{n_T - 1}), \tag{9.4}$$

where $\xi = i(k - k_T)\cos\Delta\phi$. Note that we chose ETAS rather than ETASR to approximate the system because the right hand side of equation 8.8 has a different expansion variable than the left hand side. As before, to construct a projection matrix, each of the Taylor terms in the right hand side are added into the Krylov subspace, which results in a larger ROM. Since equation 9.4 preserves the distinct Taylor expansion variables on each side of the equation in the ROM, the approach in 9.4 can be used to include frequency and zenith look angle directly into the ROM without any additional computation cost, as follows:

$$
\begin{aligned}
\widehat{\breve{\mathbf{Z}}}(s)\widehat{\breve{\mathbf{J}}} &= \sum_{j=0}^{\breve{n}} e^{-ik\breve{R}j}\mathbf{P_j}\big(\widehat{\breve{\mathbf{Z}}}_{R1} + j(k - k_T)\widehat{\breve{\mathbf{Z}}}_{R2}\big)\widehat{\breve{\mathbf{J}}} \\
&= \sum_{j=0}^{\breve{n}} e^{-ik\breve{R}j}\mathbf{V}^T\mathbf{P_{Ej}}\big(\breve{\mathbf{\mathcal{E}}}_0 + \xi\breve{\mathbf{\mathcal{E}}}_1 + \cdots + \frac{\xi^{n_T-1}}{(n_T-1)!}\breve{\mathbf{\mathcal{E}}}_{n_T-1}\big)\mathbf{V} \\
&= \sum_{j=0}^{\breve{n}} e^{-ik\breve{R}j}\big(\widehat{\breve{\mathbf{\mathcal{E}}}}_{0j} + \xi\widehat{\breve{\mathbf{\mathcal{E}}}}_{1j} + \cdots + \frac{\xi^{n_T-1}}{(n_T-1)!}\widehat{\breve{\mathbf{\mathcal{E}}}}_{(n_T-1)j}\big) \qquad (9.5)
\end{aligned}
$$

Equation 9.5 is a multi-parameter ROM including both frequency and zenith look angle developed using SPPF-FMOR techniques and which could be generated using the PFFT algorithm to take advantage of sparsification.

While this algorithm for SPPF-based, multi-parameter, with frequency and zenith look angle, and Full-wave Model Order Reduction (SPPF-MPARZLA-FMOR) has been implemented for the EM scattering problem, there has been insufficient time to collect and compare results to include in this dissertation document.

## 9.2 ROMs that include frequency, full look angle parameters, and geometrical parameters

The extensions necessary to develop and implement MOR algorithms that generate ROMs containing frequency and the full set of look angle parameters will likely be quite different that the algorithm developed in the section 9.1 for frequency and

the zenith look angle. The methods in [9] seem to apply straightforwardly, but the complicated implementation details are beyond the scope of the dissertation. In other words, this topic is the subject of ongoing research and hopefully future publications.

# Chapter 10

# Other Contributions

## 10.1 New Formulation for Impedance Extraction

Model Order Reduction with ETAS or SPPF-ETAS to a ROM of size q requires solving a large systems of equations q times. Since the fastest way to accomplish this is usually by iterative techniques [40], it is very important to use formulations that has matrices with low condition numbers.

In order to facilitate model order reduction for Impedance extraction models, one can modify the formulation so that rational functions of the frequency parameter are eliminated in each entry and the entries become polynomials of the frequency parameter $k$. This modification simplifies analytic computation of the derivatives with respect to $k$. Furthermore, rescaling branch and node quantities by the speed of light will improve conditioning of the following system:

$$\boldsymbol{Z}(ik)\boldsymbol{J} = \boldsymbol{M} \begin{bmatrix} ik\boldsymbol{R} + (ik)^2 c_0 \boldsymbol{L}(ik) & \boldsymbol{0} \\ \boldsymbol{0} & \frac{\boldsymbol{P}_{(ik)}}{c0} \end{bmatrix} \boldsymbol{M}^T \boldsymbol{J} = ik\boldsymbol{B} \qquad (10.1)$$
$$y = ik\boldsymbol{B}^T \boldsymbol{Z}(ik)^{-1}\boldsymbol{B}$$

The $ik$ introduced into the right hand side does not complicate MOR because it is only a scalar factor.

## 10.2 Poor Conditioning of the ETAS and SPPF-ETAS required for FMOR

Even with the improved conditioning of the new formulation 10.1, the ETAS required to facilitate MOR, will have very poor conditioning because the $Z_j$ blocks (corresponding to frequency derivates of those blocks of the system matrix) in the top row have very different magnitudes. One can see this by examining the elements of $Z(ik)$ in equation 10.1 which have the form $\frac{p(ik)e^{-ikr}}{r}$, where $k$ is the frequency variable, also known as the wave number, defined by $ik = \frac{s}{c_0}$ , $p(ik)$ is just a polynomial in $ik$, and $r$ represents the interaction distances corresponding to each element. In equation 2.70, the $Z_j$ blocks in the top (block) row represent the successive terms of the Taylor series approximation to equation 10.1, and the elements of the $ith$ matrices will have the form $r^{i-1}e^{-ikr}$. Thus, the blocks $Z_j$ will have very different magnitudes, resulting in poor conditioning for the overall system.

In SPPF algorithms, frequency derivates of the system matrix correspond to frequency derivates of the SPPF remainder matrix which contain remainder phase factors. Since the distances in the remainder phase factors are much smaller, the scaling problem and conditioning will be even worse for the SPPF-ETAS expanded from the SPPF-remainder matrices.

## 10.3 A method to Improve Conditioning for the ETAS and SPPF-ETAS

Letting $\Delta = i(k - k_T)$, the following alterations to the formulation described in equation 2.70 will improve conditioning for both ETAS and SPPF ETAS:

160

$$\left[ \begin{bmatrix} \boldsymbol{Z_0} & \boldsymbol{0} & \cdots & \boldsymbol{0} \\ \boldsymbol{0} & \frac{\boldsymbol{I}}{\beta} & \boldsymbol{0} & \vdots \\ \vdots & \boldsymbol{0} & \ddots & \boldsymbol{0} \\ \boldsymbol{0} & \cdots & \boldsymbol{0} & \frac{\boldsymbol{I}}{\beta} \end{bmatrix} \right.$$

$$\left. +\Delta(ik) \begin{bmatrix} -\boldsymbol{Z_1} & -\frac{\boldsymbol{Z_2}}{\beta} & -\frac{\boldsymbol{Z_3}}{\beta^2} & \cdots & -\frac{\boldsymbol{Z_{n_T-1}}}{\beta^{(n_T-2)}} \\ \frac{\boldsymbol{I}}{2} & \boldsymbol{0} & \boldsymbol{0} & \cdots & \boldsymbol{0} \\ \boldsymbol{0} & \frac{\boldsymbol{I}}{3} & \boldsymbol{0} & \cdots & \boldsymbol{0} \\ \vdots & \ddots & \ddots & \ddots & \boldsymbol{0} \\ \boldsymbol{0} & \boldsymbol{0} & \boldsymbol{0} & \frac{\boldsymbol{I}}{n_T-1} & \boldsymbol{0} \end{bmatrix} \right] \begin{bmatrix} \boldsymbol{J_0} \\ \boldsymbol{J_1} \\ \boldsymbol{J_2} \\ \vdots \\ \boldsymbol{J_{n_T-1}} \end{bmatrix} = \begin{bmatrix} \boldsymbol{B} \\ \boldsymbol{0} \\ \boldsymbol{0} \\ \vdots \\ \boldsymbol{0} \end{bmatrix} , (10.2)$$

In Equation 10.2, the $\beta$ parameter is a representative distance, maybe an average for the entire block. With judicious choice of $\beta$, this modification improved the system conditioning dramatically, by rescaling the blocks $\boldsymbol{Z_j}$. The examples we studied demonstrated an improvement in the condition number of the SPPF-ETAS ranging between 5-10 orders of magnitude.

## 10.4 A method to Improve Conditioning for the SPPF-ETAS

Letting $\Delta = i(k - k_T)$, the following alterations to the SPPF-ETAS formulation of equation 4.6 will improve conditioning:

$$\boldsymbol{\breve{\mathcal{Z}}}(s)\boldsymbol{\breve{\mathcal{J}}} = \sum_{j=0}^{\breve{n}} e^{-ik\breve{R}j} \boldsymbol{\mathcal{P}}_| \left[ \begin{bmatrix} \boldsymbol{\breve{Z}_0} & \boldsymbol{0} & \cdots \\ \boldsymbol{0} & \frac{\boldsymbol{I}}{\beta} & \ddots \\ \vdots & \ddots & \ddots \end{bmatrix} \right.$$

$$+\Delta \begin{bmatrix} -\breve{Z}_1 & -\frac{\breve{Z}_2}{\beta} & -\frac{\breve{Z}_3}{\beta^2} & \cdots & -\frac{\breve{Z}_{n_T-1}}{\beta^{n_T-2}} \\ \frac{I}{2} & 0 & 0 & \cdots & 0 \\ 0 & \frac{I}{3} & 0 & \cdots & 0 \\ \vdots & \ddots & \ddots & \ddots & 0 \\ 0 & 0 & 0 & \frac{I}{n_T-1} & 0 \end{bmatrix} \begin{bmatrix} \breve{J}_0 \\ \breve{J}_1 \\ \breve{J}_2 \\ \vdots \\ \breve{J}_{n_T-1} \end{bmatrix} \approx \mathcal{B}. \qquad (10.3)$$

As before, the value of the $\beta$ parameter in Equation 10.3 is selected to be a representative distance, maybe an average for the entire block. With judicious choice of $\beta$, this modification improved the system conditioning dramatically, by rescaling the blocks $\boldsymbol{Z_j}$. As for the ETAS, the examples we studied demonstrated an improvement in the condition number of the SPPF-ETAS ranging between 5-10 orders of magnitude.

# Chapter 11

# Conclusion

Computational electromagnetic analysis is used to extract impedance models for the interconnect that connects the components on SoB's and SoP's which operate over a wide frequency bandwidth. While these parameter-dependent models accurately characterize the parameter-dependent behavior of the original interconnect system, the models correspond to extremely large parameter-dependent linear systems of equations that require enormous computational resources to solve. As a result of the model complexity, simulating the interconnect and the components is infeasible using the solver-generated impedance models.

Computational electromagnetic analysis is also used to compute models that accurately characterize the parameter dependent scattering behavior when electromagnetic waves scatter from a targets of interest. The parameter dependent models can be solved to compute induced current densities at individual parameter points, and, once the induced current densities are known, other quantities of interest are easily computed, such as scattered fields at observation points and radar cross sections, at those parameter points. However, as in the case of the impedance models, these extremely large parameter-dependent linear systems of equations require enormous computational resources to solve. The size of these models often precludes use in inverse scattering applications and for large parameter sweeps solves of the system.

Model Order Reduction (MOR) algorithms generate reduced order models (ROMs) that approximate the parameter-dependent behavior of the original system over a

limited frequency range. This frequency range can be extended by techniques known as multi-point MOR. Since, the resulting reduced order models can be solved very rapidly, MOR can enable a simulation, rapid parameter sweeps, and a variety of inverse scattering applications. The computational cost to construct the ROM is usually equivalent to a few solves of the system. However, the pre-existing MOR methods are unable to efficiently and accurately characterize frequency behavior of systems over a large enough parameter range when source wavelengths of interest are comparable or smaller than the diameter of the geometry, otherwise known as a full-wave regime.

Segregation by Primary Phase Factors (SPPF) is a new algorithm that enables use of tradition MOR techniques to efficiently generate accurate reduced order models that characterize the parameter-dependent behavior of "Electromagnetically-Large" geometries for full-wave analysis in a desired frequency range. This dissertation presented techniques to enable SPPF-based multi-point MOR (SPPF-MRHSP-FMOR), to incorporate SPPF concepts into the Precorrected Fast Fourier Transform algorithm (SPPF-PFFT) in order to compute rapid matrix vector products during MOR, and to extend SPPF for approximation of systems with source vectors (SPPF-RHS) and output selection vectors (SPPF-OSV) with complicated frequency dependencies. For certain example problems, the SPPF-FMOR based techniques produced ROMs that were 100,000,000 times more accurate than ROMs generated by the pre-existing MOR technique with an equal order of computational cost. The results presented in this dissertation convincingly demonstrate that SPPF has great potential to efficiently generate accurate reduced order models for two challenging full-wave computational electromagnetic modeling applications, interconnect impedance extraction and scattering analysis.

Topics for future research will include: exploring specific application problems in order to transition the SPPF algorithms into existing technologies, exploring if the SPPF algorithms will extend to other sparsification methods, conducting an in-depth analysis of the computational complexity of tools incorporating these techniques to better understand how the various parameters are inter-related, and exploring possible

164

approaches to apply integral equation based methods to frequency ranges in which these techniques were not considered feasible (due to high panel counts) in the past.

# Appendix A

# Survey of Military Ground Vehicles

1 The USA High Mobility Multipurpose Wheeled Vehicles (HMMWV) have approximate length of 4.57 meters, width of 2.16 meters, and height of 1.83 meters.

2 The USA Shadow Reconnaissance Surveillance Targeting Vehicle (RST-V) has approximate length of 5.45 meters, width of 2.057 meters, and height of 1.397-1.674 meters

3 The USA Paladin 155MM self-propelled Howitzer has approximate length of 9.75 meters, width of 3.15 meters, and height of 3.24 meters.

4 The USA M60A3 main battle tank has approximate length with gun forward of 9.44 meters, width of 3.63 meters, and height of 3.28 meters.

5 The US Army M1 Abrams Main Battle Tank has approximate length of hull of 7.47 meters and height of 2.65 meters.

6 The USA M1A1 / M1A2 Abrams main battle tanks have approximate length with gun forward of 9.83 meters, width of 3.66 meters, turret height of 2.37 meters.

7 The Russian T-72 main battle tank has approximate length with gun forward of 9.53 meters, length of hull of 6.86 meters, width of 3.37 meters, and height of 2.26 meters.

8  The Russian T-80 main battle tank has approximate length with gun forward of 9.66 meters, length of hull of 7 meters, width of 3.4-3.6 meters, and height of 2.2 meters.

# Appendix B

# Rotation of Axes

If there is a coordinate system with $x$, $y$, and $z$ axes, the cartesian variables can be represented in terms of spherical coordinates as follows:

$$
\begin{aligned}
x &= r \sin(\phi) \cos(\theta) \\
y &= r \sin(\phi) \sin(\theta) \\
z &= r \cos(\phi),
\end{aligned}
\tag{B.1}
$$

Similarly, a second coordinate system with $x'$, $y'$, and $z'$ axes, the cartesian variables can be represented in terms of spherical coordinates as follows:

$$
\begin{aligned}
x' &= r' \sin(\phi') \cos(\theta') \\
x' &= r' \sin(\phi') \sin(\theta') \\
z' &= r' \cos(\phi').
\end{aligned}
\tag{B.2}
$$

If the second coordinate axes are merely rotated around the original origin point and not translated, then the rotation of $\Delta\phi$ and $\Delta\theta$ radians could be represented in spherical coordinates, as follows:

$$r' = r$$
$$\phi' = \phi + \Delta\phi$$
$$\theta' = \theta + \Delta\theta, \tag{B.3}$$

In this case of rotation without translation, the variables $x'$, $y'$, and $z'$ will have the values

$$x' = r\sin(\phi + \Delta\phi)\cos(\theta + \Delta\theta)$$
$$y' = r\sin(\phi + \Delta\phi)\sin(\theta + \Delta\theta)$$
$$z' = r\cos(\phi + \Delta\phi). \tag{B.4}$$

If the only rotation is restricted to the zenith angle,

$$r' = r$$
$$\phi' = \phi + \Delta\phi$$
$$\theta' = \theta, \tag{B.5}$$

then new coordinates $x'$, $y'$, and $z'$ will have the values:

$$x' = r\sin(\phi + \Delta\phi)\cos(\theta)$$
$$= r\cos(\phi)\sin(\Delta\phi)\cos(\theta) + r\sin(\phi)\cos(\Delta\phi)\cos(\theta)$$
$$= \frac{zx}{\rho}\sin(\Delta\phi) + x\cos(\Delta\phi)$$
$$y' = r\sin(\phi + \Delta\phi)\sin(\theta)$$
$$= r\cos(\phi)\sin(\Delta\phi)\sin(\theta) + r\sin(\phi)\cos(\Delta\phi)\sin(\theta)$$

$$\begin{aligned}
&= \frac{zy}{\rho}\sin(\Delta\phi) + y\cos(\Delta\phi)\\
z' &= r\cos(\phi + \Delta\phi)\\
&= r\cos(\phi)\cos(\Delta\phi) + r\sin(\phi)\sin(\Delta\phi)\\
&= z\cos(\Delta\phi) + \rho\sin(\Delta\phi),
\end{aligned}\tag{B.6}$$

where $\rho = \sqrt{x^2 + y^2}$. Therefore a rotation of axes for only zenith angle would merely scale the exponent of the source terms by the cosine of the zenith angle shift $\Delta\phi$:

$$\Rightarrow e^{jkz_l'} \rightarrow e^{jkz_l\cos(\Delta\phi)}\tag{B.7}$$

# Bibliography

[1] D.A. Anderson, J.C. Tannehill, and R.H. Pletcher. *Computational Fluid Mechanics and Heat Transfer*. Taylor and Francis, Bristol, PA, 1984.

[2] R. Beatson and L. Greengard. A short course on fast multipole methods.

[3] G. Chen and J. Zhou. *Boundary Element Methods*. Academic Press, San Diego, CA, 1992.

[4] Chew, Jin, Michielssen, and Song. *Fast and Efficient Algorithms in Computational Electromagnetics*. Artech House Publishers, Boston, MA, 2001.

[5] E. Chiprout and M.S. Nakhla. *Asymptotic Waveform Evaluation and Moment Matching for Interconnect Analysis*. Kluwer Academic Publishers, Norwell, MA, 1946.

[6] Eli Chiprout, Hansruedi Heeb, Michael S. Nakhla, and Albert E. Ruehli. Simulating 3-D retarded interconnect models using complex frequency hopping (CFH). In *Proc. of IEEE/ACM International Conference on Computer Aided-Design*, pages 66–72, Santa Clara, California, November 1993.

[7] Eli Chiprout and Michael Nakhla. Generalized Moment-Matching Methods for Transient Analysis of Interconnect Networks. In $29^{th}$ *ACM/IEEE Design Automation Conference*, pages 201–206, Anaheim, California, June 1992.

[8] R. Coifman, V. Rokhlin, and S. Wandzura. The fast multipole method for the wave equation: A pedestrian prescription. *IEEE Antennas and Propagation Mag.*, 35(3), June 1993.

[9] L. Daniel, C. S. Ong, S. C. Low, K. H. Lee, and J. K. White. Geometrically parameterized interconnect performance models for interconnect synthesis. In *International Symposium in Physical Design*, pages 202–207, San Diego, CA, USA, April 2002.

[10] Luca Daniel. *Simulation and Modeling Techniques for Signal Integrity and Electromagnetic Interference on High Frequency Electronic Systems*. PhD thesis, University of California at Berkeley, 2003.

[11] Y.E. Erdemli, J. Gong, C.J. Reddy, and J.L. Volakis. Fast rcs pattern fill using awe technique. *IEEE Transactions on Antennas and Propagation*, 46(11):1752–1753, Nov 1998.

[12] P. Feldman and R.W. Freund. Efficient linear circuit analysis by pade approximation via the lanczos process. *IEEE Transactions CAD*, 14:639–649, May 1995.

[13] Peter Feldmann and Roland W. Freund. Efficient linear circuit analysis by Padé approximations via the Lanczos process. In *EURO-DAC'94 with EURO-VHDL'94*, September 1994.

[14] Peter Feldmann and Roland W. Freund. Reduced-order modeling of large linear subcircuits via a block Lanczos algorithm. In $32^{nd}$ *ACM/IEEE Design Automation Conference*, pages 474–479, San Francisco, CA, June 1995.

[15] K. Gallivan, E. Grimme, and P.V. Dooren. A rational lanczos algorithm for model reduction. *Numerical Algorithms*, 12:33–63, 1996.

[16] L. Greengard, J. Huang, V. Rokhlin, and S. Wandzura. Accelerating fast multipole methods for the Helmholtz equation. *Computational science and engineering*, 5:32–37, July 1998.

[17] L. Greengard and V. Rokhlin. A new version of the fast multipole method for the Laplace equation in three dimensions. *Acta Numerica*, pages 229–269, 1997.

[18] Eric Grimme. *Krylov Projection Methods for Model Reduction.* PhD thesis, Coordinated-Science Laboratory, University of Illinois at Urbana-Champaign, Urbana-Champaign, IL, 1997.

[19] R. F. Harrington. *Field Computation by Moment Methods.* MacMillan, New York, 1968.

[20] H. Heeb and A. E. Ruehli. Three-dimensional interconnect analysis using partial element equivalent circuits. *IEEE Trans. On Circuits and Systems I: Fundamental Theory and Applications*, 39(11):974–982, November 1992.

[21] F. B. Hildebrand. *Advanced Calculus for Applications.* Prentice Hall Inc, New Jersey, 1976.

[22] J.D. Jackson. *Classical Electrodynamics.* John Wiley and Sons, Inc., New York, NY, 1975.

[23] M. Kamon, N. Marques, and J. K. White. FastPep: a fast parasitic extraction program for complex three-dimensional geometries. In *Proc. of the IEEE/ACM International Conference on Computer-Aided Design*, pages 456–460, San Jose, CA, November 1997.

[24] M. Kamon, N. Marques, and Jacob White. Fastpep: a fast parasitic extraction program for complex three-dimensional geometries. In *Proc. of the IEEE/ACM International Conf. on CAD*, pages 456–460. IEEE/ACM, November 1997.

[25] M. Kamon, M. J. Tsuk, and J. K. White. FASTHENRY: A multipole-accelerated 3-D inductance extraction program. *IEEE Trans. on Microwave Theory and Techniques*, 42(9):1750–8, September 1994.

[26] S. Kapur and D. E. Long. Ies3: efficient electrostatic and electromagnetic simulation. *Computational Science and Engineering, IEEE*, 5(4):60–67, Oct-Dec 1998.

[27] E. Michielssen. *Method of Moments: Fundamentals, Electromagnetic Computation on Parallel and Distributed Architectures Part 3.* Electromagnetic Communication Lab, University of Illinois, Urbana, IL.

[28] R. Mittra, S.L. Ray, and A.F. Peterson. *Computational Methods for Electromagnetics.* IEEE Press, Oxford, 1960.

[29] Kenneth Nabors and Jacob White. Fast capacitance extraction of general three-dimensional structures. *IEEE Trans. On Microwave Theory and Techniques,* June 1992.

[30] A. Odabasioglu, M. Celik, and L.T. Pileggi. Prima: Passive reduced-order interconnect macromodelling algorithm. *IEEE Trans. on Computer-Aided Design of Integrated Circuits and Systems,* 17(8):645–654, August 1998.

[31] Altan Odabasioglu, Mustafa Celik, and Lawrence Pileggi. Prima: Passive reduced-order interconnect macromodeling algorithm. Technical report, Carnegie-Mellon University, Pittsburgh, PA, 1997.

[32] A. T. Patera and E. M. Ronquist. *Introduction to Finite Element Methods.* Massachusetts Institute of Technology, Cambridge, MA, 1998.

[33] A.F. Peterson. The interior resonance problem associated with surface integral equations of electromagnetics: Numerical consequences and a survey of remedies.

[34] J. Phillips, E. Chiprout, and D.D. Ling. Efficient full-wave electromagnetic analysis via model-order reduction of fast integral transforms. In *DAC Proceedings.* Design Automation Conference, June 1996.

[35] J. R. Phillips, E. Chiprout, and D. D. Ling. Efficient full-wave electromagnetic analysis via model-order reduction of fast integral transforms. In $33^{rd}$ *ACM/IEEE Design Automation Conference,* pages 377–382, Las Vegas, Nevada, June 1996.

[36] J. R. Phillips and J. K. White. A Precorrected-FFT method for electrostatic analysis of complicated 3-D structures. *IEEE Trans. on Computer-Aided Design of Integrated Circuits and Systems*, 16(10):1059–1072, October 1997.

[37] Joel Phillips. *Solution of potential integral equations in complicated 3-dimensional geometries.* PhD Thesis, Massachusetts Institute of Technology, Cambridge, MA, 1998.

[38] S. Rao, D. Wilton, and A. Glisson. Electromagnetic scattering by surfaces of arbitrary shape. *IEEE Transactions on Antennas and Propagation*, 30(3):409–418, May 1982.

[39] S. Rao, D. Wilton, A. Glisson, D.H. Schaubert, O.M. Al-Bundak, and C.M. Butler. Potential integrals for uniform and linear source distributions on polygonal and polyhedral domains. *IEEE Transactions on Antennas and Propagation*, 32(3):276–281, March 1984.

[40] Y. Saad. *Iterative Methods for Sparse Linear Systems.* PWS Publishing Company, Boston, MA, 1996.

[41] L. M. Silveira, M. Kamon, I. Elfadel, and J. K. White. Coordinate-transformed arnoldi algorithm for generating guarantee stable reduced-order models of RLC. *Computer Methods in Applied Mechanics and Engineering*, 169(3-4):377–89, February 1999.

[42] L. M Silveira, M. Kamon, and J. K. White. Direct computation of reduced-order models for circuit simulation of 3-d interconnect structures. In *Proceedings of the 3$^{rd}$ Topical Meeting on Electrical Performance of Electronic Packaging*, pages 254–248, Monterey, California, November 1994.

[43] J.M. Song and W.C. Chew. Multilevel fast multipole algorithm for solving combined field integral equation of electromagnetic scattering.

[44] L. Zhao and A. C. Cangellaris. Reduced-order modeling of electromagnetic field interactions in unbounded domains truncated by perfectly matched layers. *Microwave and Op. Tech. Lett.*, 17(1):62–66, Jan 1998.

[45] T. Zhou, S.L. Dvorak, and J.L. Prince. Application of subspace projection approaches for reduced-order modeling of electromagnetic systems. *IEEE Transactions on Advanced Packaging*, 26(4):353–360, Nov 2003.

[46] Zhenhai Zhu, Ben Song, and Jacob White. Algorithms in fastimp: a fast and wideband impedance extraction program for complicated 3-d geometries. In *DAC Proceedings*, pages 712–717. Design Automation Conference, June 2003.